UNIVERSITY OF COPENHAGEN
FACULTY OF SCIENCE

This thesis has been submitted to the PhD School of The Faculty of Science, University of Copenhagen

On the nature of dark matter structures, and the growth of charged atmospheric aerosols

Jacob Svensmark

Supervised by Steen H. Hansen

September 2019

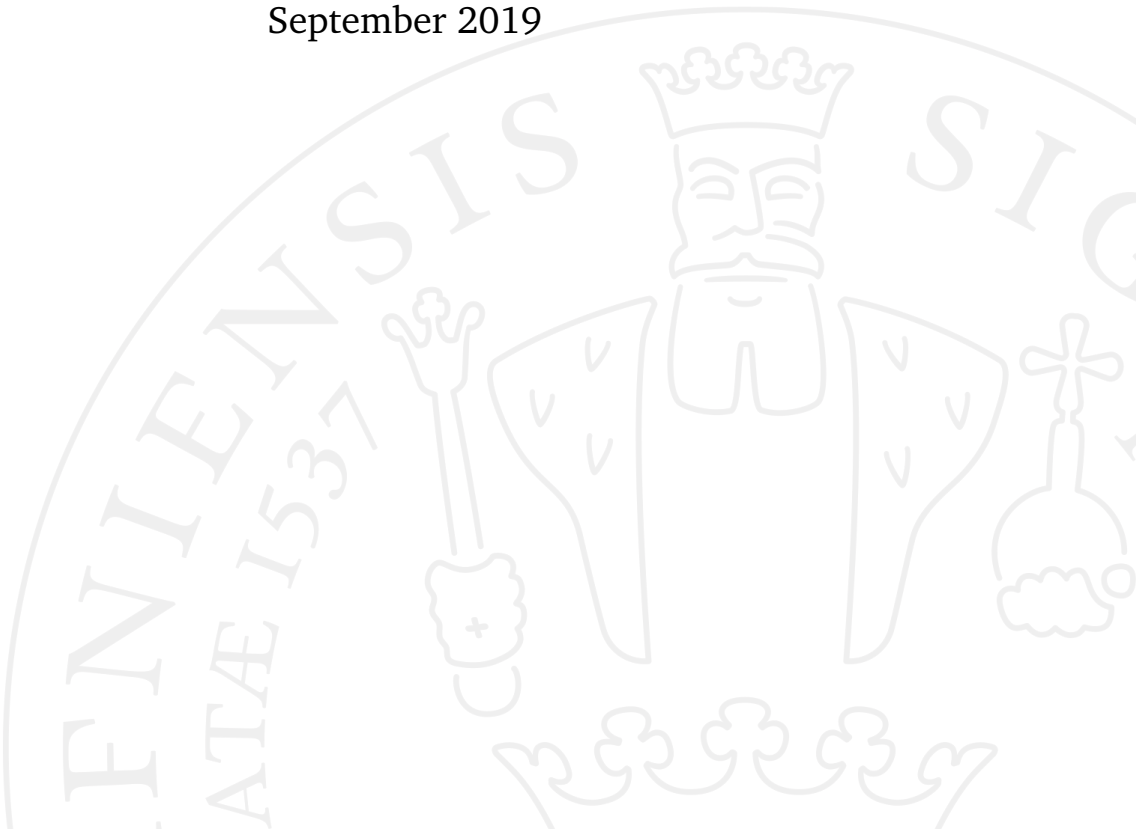

Jacob Svensmark

On the nature of dark matter structures, and the growth of charged atmospheric aerosols

This thesis has been submitted to the PhD School of The Faculty of Science, University of Copenhagen,
September 2019
Supervisor: Steen H. Hansen

University of Copenhagen
Faculty of Science
DARK, Niels Bohr Institute
Jagtvej 128
DK-2100 Copenhagen

Acknowledgements

First of all I would like to thank my supervisor Steen for his strong support and encouragement in pursuing the science that intrigues me, and for making sure I drink enough coffee. I would also like to thank my father for years of scientific exploration as both father and colleague. I thank my colleagues Nir at the Hebrew university of Jerusalem and Martin at DTU for helping me produce better science. I would like to thank the people at DARK for always making it a pleasure to go to work. Finally I would like to thank my family: Partner, son, mother, brothers, grandmother, in-laws and friends for their strong support. Without them none of this would have been possible.

Abstract

This thesis comprises a series of articles written during my time as PhD student, which have either been published, or are currently under review for publication.
In the first paper, the so-called velocity anisotropy of the dark matter is inferred in the Perseus galaxy cluster to nearly 5 times the radius of previous estimates. Based on X-ray observations from the Suzaku telescope, the velocity anisotropy is found to be non-zero at 1.7σ. This agrees with expectations from the standard ΛCDM model of our Universe, in which the dark matter is collisionless.
The second paper, addresses some recent findings on shear measurements from a galaxy - galaxy weak gravitational lensing survey, which seemingly do not agree with predictions from the standard cosmological model of our Universe. Using the suite of N-body simulations from the ΛCDM based Illustris-TNG project, we calculate the predicted galaxy - galaxy lensing signal and find that it is strongly dependent on numerical resolution of the simulation. Furthermore, the signal is also sensitive to the criteria used for excluding non-isolated galaxies from the catalogue. This questions the strength of the weak galaxy - galaxy signal for cosmological inference at present, when state-of-the-art simulations, and thus predictions, have not reached full convergence.
In the third paper, an ion-dependent aerosol growth mechanism is presented and detected in the laboratory. Aerosols in the terrestrial atmosphere above a certain diameter of 30-50 nm act as precursors for cloud droplets, which impact the albedo of Earth and thus climate. In an 8 m^3 atmospheric reaction chamber, clean atmospheric air was introduced to ionizing radiation from two CS-137 gamma sources, attenuated by varying amounts of led. It is shown, that the growth rate of small $\sim 1-20$ nm sulfuric aerosols is proportional to the ion concentration, consistent with a theoretical description of ions as a condensing species.
In the fourth paper, an aerosol growth model is developed which solves the general dynamic equation for a neutral and charged size distribution of aerosols. Specifically, the ion induced condensation term presented in *the third paper* is included as part of the model. The ion-condensation mechanism is shown to be numerically consistent with analytical expectations. Furthermore, the effect of electric charge on aerosol-aerosol coagulation, which is another growth term of the general dynamic equation, is confirmed to be independent of ion concentration under certain assumptions. This points to the ion-induced condensation as responsible for the experimental result of *the third paper*, where aerosol growth rate is affected by the ambient ion concentration.

Abstract

Denne afhandling indeholder en række af artikler som er skrevet i min tid som PhD studerende. Disse er enten publiceret, eller i færd med at blive bedømt af fagfæller på vej til udgivelse.
I den første artikel estimerer vi hastighedsanisotropien af det mørke stof i galaksehoben Perseus ud til næsten 5 gange længere fra hobens centrum end tidligere målinger. Baseret på målinger af røntgenstråling fra Suzaku teleskopet estimerer vi hastihedsanisotropien til at være forskellig fra 0 med en sikkerhed på 1.7σ. Dette er i overensstemmelse med forventninger fra ΛCDM standardmodellen for vores Univers, i hvilken mørkt stof er kollisionsløst.
I den anden artikel adresserer vi nylige resultater fra "shear" målinger af galakse - galakse signalet fra svag gravitationel lensing. Disse målinger ikke er forenelige med kosmologiske forudsigelser fra ΛCDM modellen. Ved at analysere paletten af simuleringer udbudt under "Illustris-TNG" projektet udregner vi nye forudsigelser af dette signal, og finder at forudsigelserne er stærkt afhængige af den numeriske opløsning af simuleringerne. Derudover er signalet sensitivt overfor de kriterier der benyttes for at ekskludere ikke-isolerede galakser fra kataloget. Dette stiller for nuværende spørgsmålstegn ved styrken af det svage gravitationelle lensing galakse - galakse signal som kosmologisk probe, idet de nyeste simuleringer ikke har konvergeret tilstrækkeligt.
I den tredje artikel, bliver en ion-afhængig vækstmekanisme for aerosoler presenteret og målt i laboratoriet. Atmosfæriske aerosoler større end en vis diameter på 30-50 nm fungerer som kim til skydråber, hvilket påvirker jordens albedo og derved klima. I et $8\,\mathrm{m}^3$ atmosfærisk reaktionskammer blev ren atmosfærisk luft udsat for ioniserende stråling fra 2 CS-137 gamma kilder, reguleret vha. variendende mængder bly. I artiklen vises det, at vækstraten for hyperfine $\sim 1-20\,\mathrm{nm}$ svovlsyreholdige aerosoler er proportional med ionkoncentrationen, hvilket er konsistent med en teoretiske beskrivelse af ioner som en kondenserende gas.
I den fjerde artikel bliver en aerosolmodel, som løser "the general dynamic equation" for en neutral og ladet størrelsesfordeling af aerosoler, introduceret. Navnligt er ledet for ion-induceret kondensation, som præsenteres i den tredje artikel, inkluderet i modellen. Ion kondensationsmekanismen vises at være numerisk konsistent med forventingerne fra analytiske beregninger. Derudover bliver effekten af ladning på aerosol-aerosol koagulation, endnu et led i 'the general dynamic equation", bekræftet i at være uafhængigt af ionkoncentrationen. Dette indikerer at ion-induceret kondensation er årsag til det eksperimentelle resultat i *den tredje artikel, hvor vækstraten af aerosoler påvirkes af iontætheden*.

Contents

1 Introduction

This thesis is the result of my diverging research interest, which originated from my pre-thesis interest in interactions between our terrestrial climate, and the local astrophysical environment of the solar system. This interest in both atmospheric physics and astrophysics has taken me in two very different directions: On the one hand, the astrophysical work contained in this thesis focuses on dark matter structures, how they can be measured and what they can teach us about the nature of the Universe that we live in. On the other hand, the atmospheric work of this thesis is focused on aerosol physics, which is the result of trying to explain correlations between cosmic rays and Earths cloud cover. This has led to considerations on aerosol and ion interactions at the microphysical scale.

The thesis is organized as follows: Each of the following chapters represent a paper that I have worked on in my time as PhD student. Every chapter contains a summary section, which outlines the scientific context of the paper, the objectives of the research in the paper and an outlook for future research. This is then followed by the paper itself.

In Chapter 2 I summarize the main arguments for believing in the existence of dark matter, and point to why the velocity anisotropy of dark matter is the first logical dynamical dark matter quantity to focus on in terms of measurement. I then present the paper, in which my co-authors and I infer dark matter velocity anisotropy towards the virial radius of the Perseus cluster, and find that it agrees with the standard model of our Universe: We find that the dark matter moves in a manner consistent with being cold and collisionless. The paper is currently resubmitted for review at Monthly Notices of the Royal Astronomical Society (`arXiv:1904.04260`).

In Chapter 3 I introduce the concept of weak galaxy-galaxy gravitational lensing, and how this quantity has been used to produce measurements in tension with our standard cosmological model. I then present a paper in which my co-authors and I try to reproduce this tension by using state-of-the-art numerical N-body simulations for model predictions. We find that the tension may be resolved by the fact that numerical simulations have not reached a high enough degree of convergence to robustly predict the weak galaxy-galaxy lensing signal. The paper is currently under review at Astronomy & Astrophysics (`arXiv:1906.00975`).

In Chapter 3 I discuss the motivation for studying whether ions can affect aerosol growth rates, through correlations between solar activity or ionizing cosmic rays on the one side, and clouds or climate on the other. I then present a paper in which my co-authors and I detect an ion dependent growth mechanism in the laboratory for the first time. Here, we describe

it as an ion condensation effect. The paper was published in Nature Communications (DOI: 10.1038/s41467-017-02082-2)

In chapter 4, a paper on a numerical aerosol model is presented, in which my co-authors and I include the ion-condensation mechanism measured in chapter 4. The model was developed in parallel with the design of the experiment, and we use this model to show how it reproduces the results of the experimental and theoretical study in chapter 4. The model is released as open source code (https://github.com/jacobsvensmark/ioncage) and the paper was published in Space and Earth Science (DOI: 10.1029/2020EA001142).

On the dynamics of dark matter

2

Inferring the dark matter velocity anisotropy to the cluster edge

MNRAS, (under review)

Jacob Svensmark[1], **Steen H. Hansen**[1], **Davide Martizzi**[1], **Ben Moore**[2], **Romain Teyssier**[2]

[1] Dark Cosmology Centre, Niels Bohr Institute, University of Copenhagen, Jagtvej 128, 2200 Copenhagen.

[2] Institute for Computational Science, University of Zurich, CH-8057 Zurich, Switzerland.

Abstract

Dark matter dominates the properties of large cosmological structures such as galaxy clusters, and the mass profiles of the dark matter have been measured for these equilibrated structures for years using X-rays, lensing or galaxy velocities. A new method has been proposed, which should allow us to estimate a dynamical property of the dark matter, namely the velocity anisotropy. For the gas a similar velocity anisotropy is zero due to frequent collisions, however, the collisionless nature of dark matter allows it to be non-trivial. Numerical simulations have for years found non-zero and radially varying dark matter velocity anisotropies. Here we employ the method proposed by Hansen & Pifaretti (2007), and developed by Høst et al. (2009) to estimate the dark matter velocity anisotropy in the bright galaxy cluster Perseus, to near 5 times the radii previously obtained. We find the dark matter velocity anisotropy to be consistent with the results of numerical simulations, however, still with large error-bars. At half the virial radius we find the velocity anisotropy to be non-zero at $1.7\,\sigma$, lending support to the collisionless nature of dark matter.

2.1 Summary

In the very early universe, a brief period of inflation had caused the universe to be highly, but not perfectly smooth [Kolb and Turner, 1990]. Very slight variations between over and under dense regions in the quark-gluonic plasma were being distributed over an exceedingly large volume as the universe expanded. As the temperature of the plasma dropped below $\sim 10^{12}$K, due to an imbalance in the amount of available matter and antimatter, the quarks combined to form the first stable baryonic elements in protons, electron and neutrons. Still hot and full of energetic photons, the universe was completely ionized from an atomic perspective - protons and electrons were combined and re-ionized through emission and absorption of photons. This changed abruptly as the universe cooled to a point in which the mean photon carried less energy than the ionization energy of the hydrogen atom. Protons and electrons recombined to form atomic hydrogen atoms, drastically reducing the number of free electrons for the photons to scatter on. In essence the photons that make up this cosmic afterglow have been travelling unscattered ever since. Due to the expansion, the photons have at present been redshifted into the microwave regime, providing its name as the cosmic microwave background (CMB). Observations of the CMB offer an insight into the properties of the universe when it was very young - long before non-linear structure development complicated the picture. The statistical properties of the CMB, that is, the power of ripples on different spatial scales, is enormously sensitive to the contents of the universe. The best fit model of the CMB favours a universe in which most of the gravitating matter is not baryonic, but a form of non (or very weakly) interacting non luminous “dark” matter.

The first signs of dark matter and its large abundance began to emerge almost 90 years ago. Originally coined by astronomer Fritz Zwicky in 1933, the notion of *dunkle* referred to a non light emitting yet apparently large gravitating mass component of the Coma galaxy cluster [Zwicky, 1933]. If he assumed the galaxy cluster to be a spherical and self gravitating steady state structure, the virial theorem stated that its potential energy should be equal to twice its kinetic energy. By measuring the velocity dispersion of galaxies in the cluster, he arrived at a kinetic energy estimate far to great to be explained by their gravitational potential, hinting at a missing factor of 400 in mass. Similarly, through observation of the rotating motion of our galaxy early pioneers were able to infer that mass was missing by at least a factor of 3 [Lundmark, 1930, Oort, 1932]. In the 1970s the stellar rotation curves of galaxies was systematically studied galaxies to reveal a much faster rotation that explainable from just their stellar visible component (see eg. Rubin and Ford [1970], or other references in Bertone and Hooper [2018]).

More modern indications of dark matter is seen in the fluctuations of the baryonic density field as measured in for instance the Sloan Digital Sky Survay, mapping out the distribution of the large structure by observing galaxies between redshift of $\sim 0.1 - 0.3$. The power spectrum of angular distances between pairs of galaxies is related to the propagation of density perturbations in the early universe throgh the sound speed of the medium. Finally the highly related powerspectrum of scale and amplitude of the temperature fluctuations in the the cosmic microwave background constrains the total amount of gravitating mass. This again

is much larger than the visible mass, and shows that around 85% of the gravitating mass must be non baryonic.

In trying to uncover a particle nature of the dark matter, it is no overstatement to say that a very wide range of particle types have been considered. A particle is in part defined by its mass and scattering cross sections with itself or other particles. Suggested scattering cross sections with standard model particles span over 60 orders of magnitude, and similarly, proposed masses span over 45 [Conrad and Reimer, 2017]. It is naturally difficult to constrain such a large parameter space within a single direct detection experiment, and even with the large experimental effort that has taken place since the 90s, only a fraction of this parameter space has been ruled out.

This motivates approaching the dark matter problem from other angles than direct detection. On scales larger than 300 Mpc the universe appears homogeneous and isotropic, and is simply driven by an accelerating expansion dominated by the dark energy. On smaller scales, the initial overdensities of the expanding density field has undergone gravitational collapse, and condensed to what in named the large scale structure. The large scale structure is largely made up of dark matter, conceptually described as having collapsed in 0, 1, 2 or 3 dimensions in what is named cosmic voids, sheets, filaments or clusters respectively [Bond et al., 1996].

The largest concentrations of dark matter is found in galaxy clusters, and they remain a natural astronomical laboratory available to study dark matter properties. The stellar mass contained in galaxy clusters is far smaller than the hot gas mass of the intracluster medium. This gas exhibits a temperature in the range of 10^7 K - 10^8 K, emitting strongly in the X-ray regime through bremsstrahlung interactions [Sarazin, 1986]. If the thermal pressure of the gas is assumed to be in hydrostatic equilibrium with the gravitational pull, its temperature and density is a reflection of the total mass of the galaxy cluster. Here, the baryonic mass is typically found to make up 10%-20% of the total gravitational mass, which points to a dominating dark component. If dark matter were to interact with itself even weakly, galaxy clusters would be a natural place to observe.

Dark matter drives structure formation in its nonlinear phase, and since baryonic content mainly follows the potential well of the dark matter, the distribution of ordinary matter depends on it too. A natural question to ask is what universality one can extract from dark matter structures, and in turn if this can help us answer questions about the particle nature of dark matter itself.

As mentioned above dark matter mass and density profile can be obtained through a range of observational methods for spherical systems. In addition to X-ray observations as mentioned above, methods like gravitational lensing and Sunyaev-Zeldovic effect provides dark matter density profiles. It has been pointed out that the shape of the density profile in dark matter structures like galaxy clusters follows a power law that declines with a negative slope of $\gamma = d\ln\rho/d\ln r \sim -1$ in the inner regions, and $\gamma \sim -3$ in the outer regions. Numerical N-body dark matter simulations arrived at this overall shape of equilibrated structures based on its collisionless property [Navarro et al., 1996]. This is overall supported by observations

[Pointecouteau, E. et al., 2005]. There has however been a large attention directed towards the inner parts of smaller dark matter structures at the galaxy or dwarf galaxy scale, where a flatter central density distribution has been observed compared numerical predictions, but some modern simulations are able to resolve this through baryonic feedback.

While much attention has been devoted to the whereabouts of dark matter, focus is emerging on its dynamics. To this end, the collisionless Boltzmann equation can be employed. A collisionless fluid is completely described by its phase-space distribution function which describes the probability $P = f(\mathbf{x}, \mathbf{v}, t)d\mathbf{x}d\mathbf{v}$ of finding a collisionless particle within phase-space volume $d\mathbf{x}d\mathbf{v}$ at position $\mathbf{x}$ and velocity $\mathbf{v}$. By requiring that the distribution function obeys the continuity equation, and imposing Newtons 2nd law, the collisionless Boltzmann equation reads:

$$\frac{\partial f}{\partial t} + \mathbf{v} \cdot \frac{\partial f}{\partial \mathbf{x}} - \nabla\Phi \cdot \frac{\partial f}{\partial \mathbf{v}} = 0.$$

Here, the potential $-\nabla\Phi = \partial\mathbf{v}/\partial t$. It serves as a basis for kinematic analysis of collisionless systems, including stars in galaxies, galaxies in clusters and dark matter structures. Often it is not applied directly, but rather in *moments* of the equation, through multiplying by a velocity component and integrating over parts of phase-space. With galaxies and galaxy clusters in mind, the polar-coordinate representation of the collisionless Boltzmann equation can be multiplied by v_r, and integrated over all velocities. By assuming *spherical symmetry*, *time independence* and *no rotation*, the spherical Jeans equation emerges:

$$\frac{GM(r)}{r} = -\sigma_r^2 \left(\frac{\partial \ln\rho}{\partial \ln r} + \frac{\partial \ln\sigma_r^2}{\partial \ln r} + 2\beta \right) .$$

Here, ρ is the mass density, and $M(r)$ is the mass within radius r. σ_r^2 is the radial velocity dispersion, that is, the mean of the squared radial velocity when there is no rotation. Finally

$$\beta = 1 - (\sigma_\theta^2 + \sigma_\phi^2)/2\sigma_r^2.$$

The spherical Jeans equation is powerful, because it relates the collisionless dynamics of one species on the right hand side to the full gravitating mass profile on the left hand side. The dark matter density can be measured through a number of techniques, so the spherical Jeans equation related these to the dark matter dynamics in equilibrated structures. Certainly, this is not the only interesting dynamical aspect to consider for dark matter throughout the cosmic web. One might wish to measure for instance bulk motion or rotation in certain regions. However, equilibration allows us to input the mass distribution into the Boltzmann equation, and thus the spherical Jeans equation is probably the first logical place to look at dark matter dynamics through the velocity anisotropy of the dark matter β. For collisionless particles in mainly radial orbits, β tends towards 1. Similarly for mainly tangential orbits, β can take arbitrarily large negative values. A similar term for say a collisional gas of baryons is trivially 0, but precisely because of the collisionless nature of dark matter, that does not have to be the case. If β, much like $\rho(r)$ can be said display some universality in clusters, then its behaviour serves as a prediction from numerical simulations. β has indeed been studied in simulations. The far majority of those are based on standard ΛCDM cosmology, and find in average a radial dependency of β with a value of around 0 in the inner regions of dark matter structures, increasing towards around 0.5 in the outer regions. One study found that by introducing

a self-interacting property to the dark matter in 28 simulated galaxy clusters, the β profile decreased significantly. Since β couples to the self-scattering cross section of dark matter (if it has one), measuring it is desirable. As with any prediction of a theory, it is only a good one if it is available for testing.

The first study to present a measurement of β relied on X-ray observations of two low redshift relaxed galaxy clusters. By employing assumptions of 1) hydrostatic equilibrium of the gas and 2) equality between the gas temperature and dark matter total velocity dispersions (also referred to as "dark matter temperature" even though it cannot formally be said to have one), the velocity anisotropy was found to be non-zero at the 3σ confidence level [Hansen, S. H. and Piffaretti, R., 2007]. This approach was later expanded to 16 galaxy clusters in another study, which confirmed β as an increasing function of radius towards $0.85\,r_{2500}$ [Host et al., 2009].

Since 2009, significant improvements have been made in numerical cosmological simulations, and in observational X-ray astrophysics. In the study presented below, the main objective was to use the increased quality to probe the velocity anisotropy of dark matter in parts of the Universe where it has never been measured before: The outskirts of a galaxy cluster. To this end, three novel approaches were taken. First, the available X-ray data for the Perseus galaxy cluster as observed by the Suzaku telescope extends out to almost 5 times the radius available for previous velocity anisotropy measurements, allowing us to probe this dark matter velocity component towards the virial radius. Secondly, we calibrate the previous assumption of gas and dark matter temperature equality to an advanced hydrodynamical N-body simulation to increase the precision of the measurement. Finally, the X-ray data is available along 8 equiangular arms of the galaxy cluster, which allows us to consider the validity of hydrostatic equilibrium assumptions of each arm individually. We confirm at just under 2σ the non-zero property of β towards the virial radius of the cluster.

Future studies of velocity anisotropy will benefit from the statistics of including multiple clusters for measurements to high cluster radii. At present, the X-COP sample of X-ray galaxy cluster observations could be used [Ettori et al., 2019]. Further advances on the numerical end will also help. For instance, the relation between gas and dark matter temperature might depend on infalling structure, cluster alignment, presence of a cluster cool-core etc. The Hydrostatic equilibrium assumption is not always valid for a given galaxy cluster, and the X-ray derived mass is known to be biased low. Future studies might complement the analysis by including better mass estimates from methods such as lensing or Suyaev-Zeldovic techniques.

2.2 Introduction

The global dynamics of the expanding universe is dominated by two invisible components, namely dark matter (DM) and dark energy [Planck Collaboration et al., 2018]. In addition there exist independent gravitational observations of dark matter on smaller scales [Clowe et al., 2006]. Despite the importance of dark matter in structure formation, we still have only limited knowledge about its fundamental properties.

From a basic point of view, DM is constituted of fundamental particles, characterized by their mass and interactions with other particles. These parameters can be tested through astronomical observations as well as in terrestrial experiments. Typically, cosmological observations measure a combination of these. For instance, if DM particles interact with photons, structure formation will be affected through the ratio of the interaction cross section and the DM particle mass, $\sigma_{\gamma-\mathrm{DM}}/M_{\mathrm{DM}}$ [Bœhm et al., 2002, Hinshaw et al., 2013]. Similar constraints can be obtained for DM self-scattering or for various annihilation channels (for a list of references, see e.g. Zavala et al. [2013], Liu et al. [2016]). A range of accelerator and underground detector "null" observations have provided limits on the DM mass and interaction rates, e.g., from CMS, ATLAS, DarkSide-50, LUX [Lowette and for the CMS Collaboration, 2014, ATLAS Collaboration et al., 2015, Agnes et al., 2015, Faham, 2014]. Basically these constraints indicate that the DM has only very limited interactions besides gravity.

Structure formation has been thoroughly investigated for many years using numerical simulations in a cosmological setting. The resulting structures include galaxies and clusters at various stages of equilibration. These simulations have revealed that the DM density profile, $\rho(r)$, of individual cosmological structures changes from having a fairly shallow profile in the central regions, $\gamma_\rho = d\log\rho/d\log r \approx -1$, to a much steeper fall off in the outer regions, $\gamma_\rho \approx -3$ [Navarro et al., 2010].

For the largest equilibrated structures like galaxy clusters there is fair agreement between the numerical predictions and observations concerning the central steepness [Pointecouteau, E. et al., 2005, Vikhlinin et al., 2006]. However, for smaller structures like galaxies or dwarf galaxies, the observations have indicated that the central region has a shallower density profile than seen in numerical simulations [Salucci et al., 2007, Gilmore et al., 2007], and it is not entirely resolved whether this difference is because of significant self-interaction of the DM, or because of stellar, black hole, or supernova effects. The majority of recent state of the art simulations employing cold dark matter models with baryonic effects and stellar feedback tend to agree with observations [Amorisco et al., 2014, Santos-Santos et al., 2017, Dutton et al., 2018, Wheeler et al., 2018, Benitez-Llambay et al., 2018, Wetzel et al., 2016, Bullock et al., 2015, Teyssier et al., 2013], however some still do not find cores using this approach [Bose et al., 2018]. Some efforts have been made with alternative dark matter models, but the results are thus far not fully conclusive [Di Cintio et al., 2017, Fitts et al., 2018, González-Samaniego et al., 2017].

Observationally it is very difficult to determine other properties of the DM structures besides the density profile. The density profile is a static quantity (not involving velocity), which arises from the zeroth moment of the Boltzmann equation (i.e. mass conservation). The first moment of the Boltzmann equation instead relates to momentum conservation, and here appears the first dynamical properties in the shape of the so-called dark matter velocity anisotropy.

The principal purpose of measuring the dark matter velocity anisotropy is to improve our knowledge of dark matter. The value of the velocity anisotropy depends on the magnitude of the dark matter self-interactions [Brinckmann et al., 2018], and hence a precise measurement of the velocity anisotropy in the inner halo region should allow us to constrain the dark matter collisionality. Furthermore, it has been suggested from theoretical considerations that there should be a correlation between the dark matter velocity anisotropy and the total mass profile [Hansen, 2009], and a future accurate measurement of both would allow testing this prediction. Finally, it is possible that the velocity anisotropy in the outer cluster regions could depend on cosmological parameters, even though, to our knowledge, this has not yet been thoroughly investigated. Hopefully an investigation like the one we are presenting here, will inspire simulators to make such an investigation.

We will in this paper attempt to infer the dark matter velocity anisotropy of the Perseus galaxy cluster. The technique we use is based only on the observation of hot X-ray emitting gas, and it uses the combined analysis of both the gas equation (hydrostatic equilibrium) and the Jeans equation with the dark matter as the dynamical tracer. Measurements and analyses of the X-ray emitting hot gas have improved significantly over the last decades, and we will use the recent observation of Perseus, which extends up to the virial radius [Simionescu et al., 2011, Urban et al., 2014]. Here we define the virial radius as the radius where the enclosed density is 200 times the critical density of the universe, $r_{\rm vir} = r_{200}$. This approach of inferring velocity anisotropy contains the radial velocity dispersion of the DM as a degeneracy, and thus the resulting velocity anisotropy should be viewed as a check of the consistency of data with the DM model of the simulation that it inherently relies on.

Probing this dynamical dark matter property was originally suggested in Hansen, S. H. and Piffaretti, R. [2007], however, the first reliable estimate was made by stacking 16 galaxy clusters [Host et al., 2009]. This stacked cluster inference extended to approximately 0.85 times r_{2500}. Thus, in this paper we will extend this inference by approximately a factor 5 in radius. The following sections outline how this is done through our implementation of this method in the context of the Perseus observations.

2.3 Hydrostatic gas and equilibrated DM

The conservation of momentum for a fluid leads to the Euler equations, which for spherical and equilibrated systems reduce to the equation of hydrostatic equilibrium

$$\frac{GM(r)}{r} = -\frac{k_b T_{\rm gas}}{m_p \mu_{\rm gas}} \left(\frac{\partial \ln \rho_{\rm gas}}{\partial \ln r} + \frac{\partial \ln T_{\rm gas}}{\partial \ln r} \right) . \tag{2.1}$$

This equation simply states that when we can measure the gas temperature and gas density (all quantities on the r.h.s. of this equation) then we can derive the total mass profile. From the total mass profile one can then derive the dark matter density profile. The gas properties are typically observed through the X-ray emission from bremsstrahlung, and this X-ray determination of the dark matter density profile is very well established [Sarazin, 1986]. Alternatively, both density and temperature profiles can in principle be measured separately through the Sunyaev-Zeldovich effect.

Let us now consider the dynamical equation for the dark matter. The dark matter is normally assumed to be collisionless, and hence the fluid equations do not apply. Instead one starts from the collisionless Boltzmann equation. The first moment of the collisionless Boltzmann equation leads to the first Jeans equation, which for spherical and fully equilibrated systems reads [Binney and Tremaine, 2008]

$$\frac{GM(r)}{r} = -\sigma_r^2 \left(\frac{\partial \ln \rho}{\partial \ln r} + \frac{\partial \ln \sigma_r^2}{\partial \ln r} + 2\beta \right) . \tag{2.2}$$

If we look at the r.h.s. of the Jeans equation, we see that there are 3 quantities: the dark matter density, $\rho(r)$, the radial velocity dispersion, and the velocity anisotropy

$$\beta \equiv 1 - \frac{{\sigma_\theta}^2 + {\sigma_\phi}^2}{2{\sigma_r}^2} , \tag{2.3}$$

where σ_r^2, σ_θ^2, and σ_ϕ^2 are the velocity dispersions of dark matter along the radial, polar, and azimuthal directions respectively.

We can infer the total mass and the DM density from the equation of hydrostatic equilibrium. That means that if we wish to determine the velocity anisotropy, then we must find a way to obtain the radial velocity dispersion of the dark matter, σ_r^2. To that end we will need assistance from numerical simulation, which we will explain in detail below. The conclusion will be that we can map the gas temperature to the DM velocity dispersion. Thus the inference of the dark matter velocity anisotropy depends on the ability of numerical simulations to reliably map between gas temperature and DM dispersion.

The dark matter particles are normally assumed to be collisionless, and hence the halos of dark matter will never achieve a thermal equilibrium with Maxwellian velocity distributions [Hansen et al., 2006, Binney and Tremaine, 2008, Chapter 4]. Therefore the DM cannot formally be claimed to have a “temperature”. However, for normal collisional particles there is a simple connection between the thermal energy of the gas and the temperature, and we use a similar terminology for dark matter, and hence discuss its “temperature” as a representation of its local kinetic energy:

$$T_{\rm DM} \equiv \frac{m_p \mu_{\rm DM}}{3k_b} \sigma_{\rm DM}^2 , \tag{2.4}$$

where the total dispersion is the sum of the three one-dimensional dispersions

$$\sigma_{\rm DM}^2 \equiv \sigma_r^2 + \sigma_\theta^2 + \sigma_\phi^2 . \tag{2.5}$$

Since the dark matter and gas particles inside an equilibrated cosmological structure experience the same gravitational potential, then we should expect the gas and DM temperatures to be approximately equal [Hansen, S. H. and Piffaretti, R., 2007]. Later analyses have shown [Host et al., 2009, Hansen et al., 2011] that the ratio of DM to gas temperatures

$$\kappa \equiv \frac{T_{\rm DM}/\mu_{\rm DM}}{T_{\rm gas}/\mu_{\rm gas}}\,, \tag{2.6}$$

is a slowly varying function of radius, always of the order unity.

2.4 DM velocity anisotropy from observables

The Jeans equation can be rewritten as

$$\beta = -\frac{1}{2}\left(\frac{\partial {\rm ln}\rho}{\partial {\rm ln}r} + \frac{\partial {\rm ln}\sigma_r^2}{\partial {\rm ln}r} + \frac{GM(r)}{r\sigma_r^2}\right). \tag{2.7}$$

We will now clarify how the 3 terms on the r.h.s. can be expressed as functions only of the measured gas temperature and density, and also the calibration of κ from numerical simulations. As discussed above, by measuring the gas temperature and density, the equation of hydrostatic equilibrium, Eq. (2.1), gives us the total mass profile. In addition this allows us to derive the DM density profile, $\rho = \rho_{\rm tot} - \rho_{\rm gas}$. Thus we only need an expression for the radial velocity dispersion of the dark matter, σ_r^2. Combining the definitions in Eqs. (2.3, 2.4, 2.5, 2.6) gives

$$2\sigma_r^2\beta = 3\sigma_r^2 - 3\frac{k_b T_{\rm gas}}{m_p \mu_{\rm gas}}\kappa\,. \tag{2.8}$$

This allows us to rewrite the Jeans equation as

$$\sigma_r^2\left(\frac{d\,\ln\rho_{\rm DM}}{d\,\ln r} + \frac{d\,\ln\sigma_r^2}{d\,\ln r} + 3\right) = \psi(r). \tag{2.9}$$

where the quantity

$$\psi(r) = \left(\frac{3k_b}{m_p}\frac{T_{gas}}{\mu_{gas}}\kappa - \frac{GM(r)}{r}\right) \tag{2.10}$$

contains quantities from the X-ray observables, as well as κ. Equation 2.9 can be solved as

$$\sigma_r^2(r) = \frac{1}{\rho_{\rm DM} r^3}\int_0^r dr'\,\psi(r')\,\rho_{\rm DM}(r')\,r'^2, \tag{2.11}$$

through numerical integration. The solution to the integral depends on the boundary condition on σ_r. Here we assume that $\sigma_r^2(0) = 0$. In this way we have all the quantities on the r.h.s. of Equation (2.7), and β can directly be calculated.

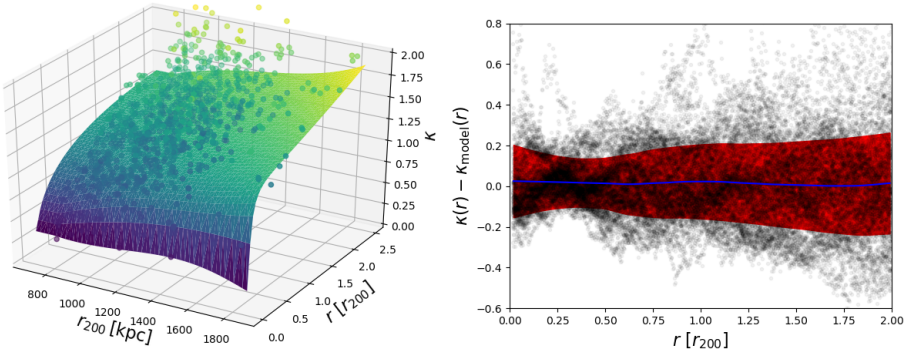

Figure 2.1: κ-profiles for the 51 clusters of the RAMSES simulation, as function of radius and r_{200}. Left panel shows a 2D smoothing spline to the profiles, and right panel shows the 1σ scatter contours of the residuals collapsed along the r_{200} direction. The smoothed surface, and scatter profile serves as parametrization for $\kappa(r, r_{200})$ profiles for observations.

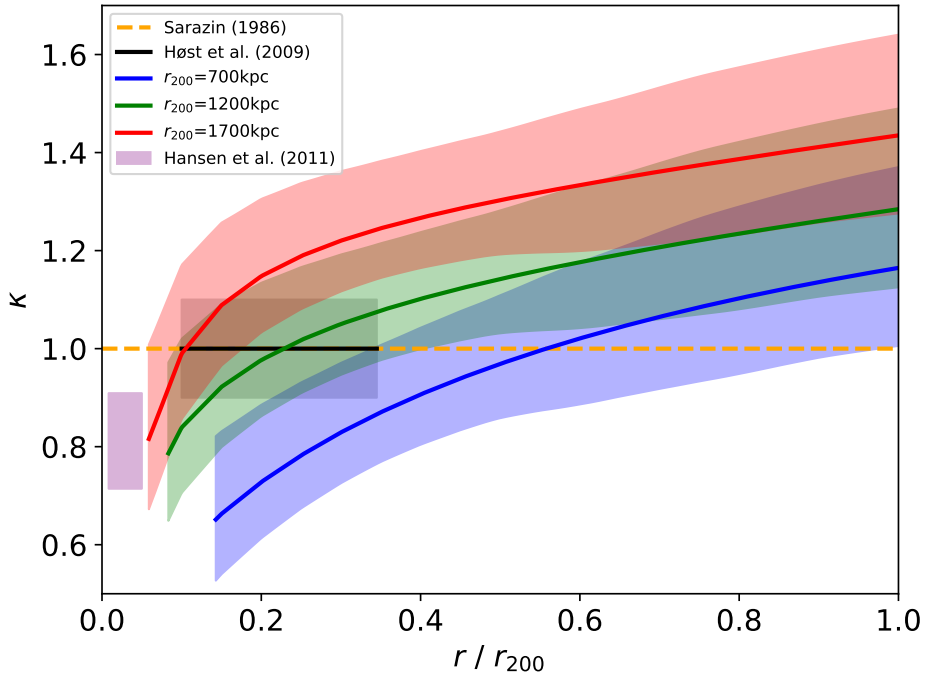

Figure 2.2: Comparison of κ-profiles used here and in previous works [Sarazin, 1986, Host et al., 2009]. Bands on the curves display 1σ spread of the κ-profiles. Note that in [Sarazin, 1986], κ=1 by assumption, so no error bands are shown here. The purple band of [Hansen et al., 2011] shows the approximate area in which their curve varies.

2.5 Numerical simulation and parametrizing κ

The energy-argument that the DM dispersion should be approximately equal to the gas temperature ($\kappa \approx 1$) in relaxed gravitating structures has a long history [Sarazin, 1986]. The anticipation that κ may change significantly when gas is cooling was investigated by Hansen et al. [2011], where κ was extracted for Milky Way like galaxies as a function of redshift (where cooling is extremely much more significant than in cluster outskirts). There it was found that as long as the high-density/low-temperature component of the gas is removed, then κ remains close to unity around $z = 0$.

Here we take possibly the most modern approach to gas cooling and other radiative processes in simulation to extract κ. We chose to use a simulation with the AMR code RAMSES [Teyssier, R., 2002], which uses flat ΛCDM cosmology with cosmological constant density parameter $\Omega_\Lambda = 0.728$, matter density parameter $\Omega_m = 0.272$ of which the baryonic density parameter is $\Omega_b = 0.045$, power spectrum normalization $\sigma_8 = 0.809$, primordial power spectrum index $n_s = 0.963$, and current epoch Hubble parameter $H_0 = 70.4\,\mathrm{km/s/Mpc}$. To identify large galaxy clusters, the simulation was initially run as a dark-matter-only simulation with comoving box size $144\,\mathrm{Mpc}/h$ and particle mass $m_{\mathrm{DM}} = 1.55 \cdot 10^9\, M_\odot/h$. Here h is the dimensionless Hubble parameter, defined as $h = \frac{H_0}{100\,\mathrm{km/s/Mpc}}$. After running the dark matter only simulation, 51 cluster sized haloes with total masses above $10^{14}\, M_\odot/h$ were identified and resimulated including the baryonic component, with dark matter particle mass $m_{\mathrm{DM}} = 1.62 \cdot 10^8\, M_\odot/h$ and baryonic component mass resolution of $3.22 \cdot 10^7\, M_\odot$. The 51 resimulation runs implemented models of radiation, gas cooling, star formation, metal enrichment, supernova and AGN feedback, and were evolved to $z = 0$. A detailed description of the simulation can be found in Martizzi et al. [2014].

For the 51 clusters, the κ profile can be calculated in spherical bins according to equation 2.6. Since all quantities contained in κ depend on the cluster size, we calculate a 2D smoothing spline surface for the 51 $\kappa(r, r_{200})$ profiles, such that given r_{200} for a cluster, $\kappa(r)$ can be retrieved (left panel of figure 2.1). The error associated with using this κ function is approximated from the residual after collapsing it in the r_{200} direction (figure 2.1 right panel), and we find no strong correlation or systematics within these residuals. The resulting $1\,\sigma$ standard deviation profile can then be taken into account when inferring $\beta(r)$.

In Figure 2.2 we show how previous κ-estimates compare to the one(s) we use here. Profiles from the fitted smoothing spline surface are shown for three cluster sizes: 700 kpc, 1200 kpc and 1700 kpc. We find κ to increase with cluster size on the displayed radial range. Sarazin [1986] assumed $\kappa = 1$, which is obviously a first approximation, but depending on the cluster size, reasonable within $0.3 r_{200}$. Later numerical approaches, such as the use of `GADGET-2` [Kay et al., 2007] (previously used to extract κ [Host et al., 2009]), yields a similar κ. Host et al. [2009] include radial constraints and an error band around $\kappa = 1 \pm 0.1$, shown as the black shaded area on Figure 2.2. The size range of the clusters considered in Host et al. [2009] is comparable to the green curve in Figure 2.2, and they are found to be consistent within error bars. In Figure 2.2 the lower κ limit of Host et al. [2009] is truncated at $0.1 r_{200}$. At lower radii,

the effects from AGN feedback become relevant, which was not included in the GADGET-2 simulations. A first step towards including AGN feedback was done in Figure 7 of Hansen et al. [2011]. Here a clear AGN effect is seen in the inner parts of the cluster in their conservative AGN feedback model estimate. Note, that for this figure we have taken into account that they use a different definition of the calibration between gas and DM temperatures. As gas temperature increases towards the cluster center, κ (in our definition) decreases, which results in a sharp decrease. This decrease, shown as an approximate purple square in Figure 2.2 is consistent with the decrease we observe in our κ profiles, which are based on simulations that take a more advanced approach to implementing AGN feedback. One could imagine further explorations of κ. We have performed some preliminary investigation on κ parametrization based on relaxedness, and found that while it adds to κ scatter, the effect was subdominant to the cluster size effect. Relaxedness, presence of a cool core, triaxiality and other effects could however be subjects for future study.

Herein lies the core of the method, but notably also the reason why resulting β profiles cannot be called de facto measurements. Rather they are consistency checks with the DM model employed in the simulation that produces the κ relation. The Jeans equation assumes DM to be collisionless, as (in this case) does the simulation that produces κ, however should this assumption not be valid, a measured β profile might not be consistent with those of simulations. From an observational point of view, the κ-parametrisation makes good sense, as measurements of the mass profile and thus r_{200} of galaxy clusters are independent of κ. Thus by observing the properties of the hot X-ray emitting gas we can obtain $\kappa(r)$ using our parametrization, and from this calculate $\sigma_r^2(r)$ from eq. 2.9 and finally $\beta(r)$ from eq. 2.8 and 2.6, assuming that the gas is fully equilibrated. The next section is dedicated to reinforcing the soundness of this assumption in the observations that we choose to analyze.

2.6 Excluding infeasible sectors from analysis

One of the core assumptions in deriving massprofiles from the X-ray signal in galaxy clusters is that of hydrostatically equilibrated gas. This excludes a large block of potential cluster targets for study, as merging and other irregularities causes a failure to meet this demand. Previous studies show how cluster merging can cause cold front and sloshing in the hot baryonic gas, and phenomena that show up in derived X-ray profiles as unequilibrated features [Markevitch and Vikhlinin, 2007]. Data quality has however heightened through the last decades, and so has the frequency of attempts at solving this issue through data selection - considering only sections of the observational plane which best meets the assumptions of equilibrium. This makes sense if material falling onto an equilibrated structure is small enough to only disturb equilibrium locally, or that the in-falling material has not yet had time to perturb the larger equilibrated cluster in its entirety.

In order to develop and test a method of inferring β to high radii through data selection in the observational plane of galaxy clusters, we construct a mock observational catalogue from the RAMSES re-simulated clusters. Radial profiles of all quantities relevant for the present work has been extracted. We select a sub-sample of 10 randomly selected clusters in range

$14 < \log m_{200} < 15$ where half of the clusters in the sample have been classified as globally relaxed, following the criterion of Martizzi and Agrusa 2016 [Martizzi and Agrusa, 2016]. We choose a line of sight through them at random and divided each observational plane of the 10 clusters into 8 equiangular sectors. The motivation for this division originates in the Perseus X-ray observations analyzed in the next sections. Perseus is precisely observed along 8 arms at evenly spaced angles, yielding 8 gas density and temperature profiles in total for the cluster. Previous analysis of the 8 arms of Perseus has shown signatures of cold-fronts and sloshing of the gas in 5 of the 8 arms suggesting that they are suboptimal for calculations assuming hydrostatic equilibrium. The remaining 3 are shown to be more relaxed. In the following we take a similar approach selecting just the sectors that are equilibrated. We conclude that by deselecting the most deviant sectors we can reduce the scatter in our final inference of β within the RAMSES clusters.

For each of the sectors in the observational plane, 3D radial profiles from spherical shells were extracted for the gas and dark matter component, using only the particles that in projection are contained inside of that sector. Each sector can then be analyzed separately, and thus parts of the observed cluster that displays unequilibrated features may be excluded from our calculation of $\beta(r)$. With this in hand, we estimate the statistical reward in removing sectors from analysis, and use this in an attempt to reduce the errorbars of $\beta(r)$ for actual X-ray data.

Figure 2.3 displays gas temperature and density profiles for 6 of the 10 resimulated galaxy clusters for which we have 3D data. The remaining 4 clusters displayed enough unequilibrated features in the gas component that they were unfit to consider for further analysis, due to strongly inconsistent profiles across the 8 sectors of a cluster, or a steep incline in the central temperature profiles. It should be noted, that only three of the six clusters remaining were categorized as virialized using the criteria of Martizzi and Agrusa [2016]. Each column of figure 2.3 represent one of the six clusters, and the colored profiles represent individual sectors. Top panels show the gas temperature scaled by a constant, and the central panels show the gas density also scaled. From these two quantities alone it is clear that sectors within a single cluster displays some variance, which is natural to expect from a 3D numerical simulation, but also a reflection of the hydrostatic equilibrium assumption not being perfectly true. For the remainder of this section we will discuss which directions appear less equilibrated than others, considering purely the observational gas profiles.

For some of the clusters, looking only at the top two rows of figure 2.3 it is not always easy to tell whether parts of the cluster are effected by some disturbing element. The 5th column has a pretty clear signature in the temperature profiles that something is disturbing its equilibrium in the dark blue, purple and pink sectors. For the cluster in the 6th column, deviations from hydrostatic equilibrium are more subtle. Herein lies an observational challenge, and in an attempt to enhance the visibility of such subtle differences between sectors within a single galaxy cluster, we combine the two measurable quantities $\rho_{\rm gas}$ and $T_{\rm gas}$ into a single quantity.

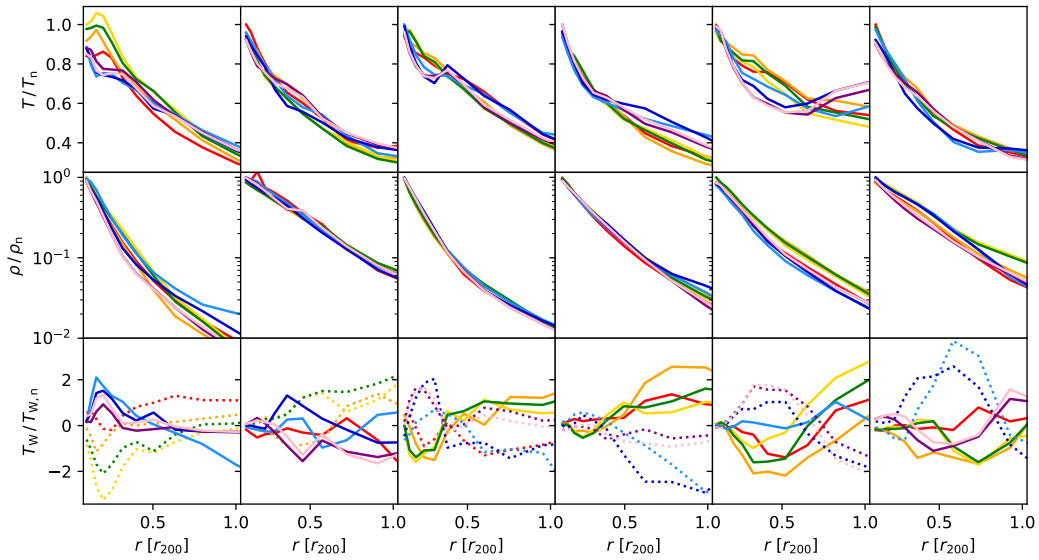

Figure 2.3: Temperature profiles (top row), gas density profiles (middle row) and weighted temperature variation profiles (bottom row) for the six resimulated RAMSES clusters considered for analysis. Each color represents one of the 8 sectors within the cluster. Neighbouring sectors are colored in the following order: Red, orange, yellow, green, light blue, dark blue, purple, pink. The dotted profiles in the bottom row indicates the sectors that were excluded from analysis due to their profile as discussed in the main text. Note that T, ρ and T_W profiles are scaled by a constant T_n, ρ_n and $T_{\mathrm{W,n}}$, which differs within each cluster, in order to compare profile shapes between clusters in this figure.

The bottom panels of figure 2.3 show this combination in the form of a weighted temperature variation profile,

$$T_\mathrm{W} = \rho_\mathrm{gas} r^2 \left(1 - \frac{T_\mathrm{gas}}{\overline{T_\mathrm{gas}}}\right), \tag{2.12}$$

where $\overline{T_\mathrm{gas}}$ is the mean temperature profile of the entire cluster. This observationally available construct emphasizes in some cases distinct groups of sectors, and by comparing these to the gas and temperature profiles of the same cluster, we try to deselect those that are least consistent with the overall trend of the cluster. Here bumps i.e. cold fronts in the temperature and density profile are features we look for [Markevitch and Vikhlinin, 2007]. In the case of well behaved clusters, this of course is less obvious, and arguably data selection may also have less of an effect. In column 3 of figure 2.3 the density is smooth, but the dark blue, light blue, pink, purple and red directions have a bump in the temperature profile. The T_W profiles show two groups that clearly differ from each other. Based on the irregular bump in the T_gas profile and the separation in the T_W figure we include only the green, orange and yellow directions, and indicate the deselected sectors with the grey color in the bottom panel. In column 6 the two blue sectors stand out slightly in the T_gas-profile, but more profoundly in the T_W profile, and are thus removed from analysis. Column 2 displays a very smooth cluster, and it is less clear which (if any) directions should be removed. We deselect the green, yellow and orange directions as they tend to lie slightly high for the high radii of primary interest for this paper. The cluster in the first column shows a kink towards its inner parts. Here, the red, orange, green and yellow profiles deviate largely within $0.7r_{200}$ from the remaining four sectors, and are thus removed from analysis. The T_W profiles of column 4 shows three main

groups, substantiating what is otherwise hard to see in the $T_{\rm gas}$ profiles alone. We remove from analysis the dark blue, light blue, purple and pink and keep the most coherent 4 sectors as indicated in the figure.

In some clusters, such as the one in column 5 of figure 2.3, signatures of a "cold-front" is visible in the sectors represented by the dark-blue, pink and purple profiles, which are consequently removed from analysis. These may be caught by performing an analysis of the X-ray data analogous with the one in Urban et al. [2014], and in this case both approaches would possibly single out the same sectors. The present exclusion process however singles out some features that are not predominantly cold-front related, and as such provides a different approach to determining which parts of a galaxy cluster that are not in equilibrium.

From the weighted temperature variation profiles in combination with the raw density and temperature profile, we have identified up to five sectors within each cluster that deviate substantially from the more relaxed conditions, and are now ready to calculate the velocity anisotropy parameter β.

2.7 Non-parametric fitting and MC resampling to data

In order to arrive at an inference of β, local fluctuations and measurement uncertainties are necessary to take into account. We employ non-parametric locally estimated scatter plot smoothing (LOESS) fitting to the gas density and temperature measurements in order to smooth out local variations [Scrucca, 2011]. In this way we manage to avoid imposing an analytical profile to our data. This yields a fitted curve and a 1σ standard deviation profile in addition. Any fit, including this one, is of course subject to a level of arbitrarity in the choice of function, and for non-parametric fits some choice of smoothing parameter and algorithm. In this case, we let the LOESS smoothing parameter be determined by a generalized cross-validation technique [Wang, 2010], which adapts to the data in question. Doing this, we obtain a smooth profile, that neglects local bumps and wiggles, however allows for larger scale variation, rather than forcing it to follow a strict parametric form. An example of a cross-validated LOESS fit to the gas temperature profile is seen is seen in figure 2.4 for a single sector in one of the galaxy clusters within the RAMSES simulation. In this example the temperature profile from the simulated data is without uncertainty and smooth in comparison with realistic measurements of the 3D temperature profiles of galaxy clusters. Therefore Gaussian errors of 3×10^6 K and error bars of the same magnitude are added. The red band of figure 2.4 represents the 68% percentile of 100 LOESS fit to the noisy data using a resampling technique assuming a Gaussian distribution, and recreates the original temperature profile in black reasonably well. The same goes for the $\rho_{\rm gas}$ in the bottom panel, though this is to be expected as uncertainties in typical gas density profiles are small compared to the temperature measurements. As explained in section 2.8 we employ a Monte Carlo resampling approach to obtain error estimates on the inferred galaxy cluster β. For an input smoothed $T_{\rm gas}$ and $\rho_{\rm gas}$ we proceed to calculate $M(r)$, $\sigma_r^2(r)$ and $\beta(r)$ through hydrostatic equilibrium assumptions,

as shown in section 2.3. In this process, we fit yet another LOESS curve to both the $M(r)$, ρ and $\sigma_r^2(r)$ profiles, to neglect the smaller bumps and ripples. This comprises the drawback of not assuming and fitting e.g. well behaved power law functions to the raw hydrostatic data. However, the multiple non-parametric fits do allow a degree (as controlled by the cross-validation mentioned above) of ripple that would otherwise not be seen in the parametric form, and in this respect the approach is arguably preferable. In the next section we can begin the process of Monte Carlo resampling $\rho_{\rm gas}$, $T_{\rm gas}$ and κ to arrive at a final inference of β and its uncertainty from a number of sectors within a single galaxy cluster.

2.8 Errors in estimating β

Each sector of each cluster is handled individually in our analysis. The final β of a given sector is obtained using a Monte Carlo resampling approach, which allows us to propagate measurement errors from the input X-ray profiles. For a single sector we produce a number $N_{\rm MC}$ of resamples of $T_{\rm gas}(r)$ using its measurement uncertainties. We resample complementary $\kappa(r)$ profiles and proceed to calculate $M(r)$, $\sigma_r^2(r)$ and $\beta(r)$ through hydrostatic equilibrium assumptions, as shown in section 2.3 and 2.7. The final β profile for a given sector is then the median profile of all β from the resamples of that sector.

Our intent is to use the procedure on multiple sectors of a single cluster (or potentially even multiple clusters, though this is left for future work), and end up with a final inference of the universal velocity anisotropy profile. We must therefore understand to what degree the procedure is biased, and how much scatter it introduces in addition to the natural scatter within cluster β profiles. To do this, we infer the β profile of two groups of sectors from the 6 RAMSES clusters selected in section 2.6: One group consisting of all 48 sectors in the 6 RAMSES clusters, and another group using only the 27 equilibrated sectors. Starting with the full set, as an intermediary step the hydrostatic massprofiles of each sector is calculated. These can be seen in figure 2.5, relative to the true mass profiles. The hydrostatic masses are just within the 1σ standard deviation profile at the radii of interest, however the mean value under-performs between between 0 and 10% low for growing radii similar to previous findings using other mass reconstruction techniques [Gifford and Miller, 2013, Armitage et al., 2018]. One could imagine correcting inferred masses accordingly, however it is non-trivial how that translates into a β correction given the simulated data we have available. For this reason we allow the hydrostatic mass measurements to under perform at these radii.

Proceeding towards β, figure 2.6 on the left shows in the red curve and red band a LOESS fit and σ scatter of the true β profiles for the full set of sectors. The black curve and grey band shows the same, but for the β profiles as inferred from only the gas observables of each sector. The mock inference of β in a sector is seen to be unbiased, with a scatter determined largely by the true scatter in β until around $0.5\,r_{200}$, at which point the scatter is dominated by assumptions of equilibrium breaking down. In order to lessen the scatter, only the sectors selected in section 2.6 i.e. the second set of sectors was used, and their true and inferred β summarized in the right hand side of figure 2.6. Notably, the scatter is lower in this case because assumptions of equilibrium are better met in these selected simulated sectors.

The grey patches in the right panel of figure 2.6 comprises scatter in the true β profiles of the simulated clusters, as well as additional scatter introduced by our analysis. As we proceed to calculate β for X-ray observations of the sectors in a single real galaxy cluster, we must incorporate this scatter in the uncertainty of our inference. How this is done depends on the amount of correlation between sectors of a single galaxy cluster. If all sectors within a single cluster are completely independent inferences of β, then the uncertainty of the joint β profile decreases by a factor $1/\sqrt{N}$ where N is the number of sectors under analysis. If on the other hand sectors within a single cluster are completely correlated, the part of the scatter that originates from natural variation in β (red patch of figure 2.6) is constant with number of sectors, whereas the residual scatter (difference between grey and red scatter) in figure 2.6, i.e. the additional scatter introduced by the analysis framework is reduced by $1/\sqrt{N}$, assuming that the two sources of scatter are directly separable. As one extreme, we could assume that all of the sectors of a single galaxy were uncorrelated in their inference of β, and as another we could assume complete correlation.

Now we have an estimate of the uncertainties involved in inferring $\beta(r)$ through X-ray data and assumptions of hydrostatic equilibrium, and a method for eliminating parts of this uncertainty by data selection. In the next section we move to apply the technique and infer $\beta(r)$ to the virial radius for the Perseus galaxy cluster.

2.9 Perseus cluster observations in X-ray

The Perseus cluster is the brightest cluster in the X-ray sky, and was observed in 85 pointings as a Suzaku Key Project, with a total exposure time of 1.1 Ms. The low particle background makes Suzaku ideal for analysing cluster outskirts. These pointings were arranged in eight arms along different azimuthal directions. For each direction the data had point sources removed and was cleaned, 21 pointings were used for a careful background modelling, and XSPEC was used to extract the deprojected temperature and density profiles [Simionescu et al., 2011, Urban et al., 2014]. Such careful treatment of the deprojection is necessary, as the calculation of β requires 3D profiles of $T_{\rm gas}$ and $\rho_{\rm gas}$ to function. For each of the eight arms, the $T_{\rm gas}$ and $\rho_{\rm gas}$ profiles can be seen with uncertainties in the top and middle panel of the LHS column in figure 2.7.

Previous careful analyses allowed a categorization of the eight arms into three “relaxed” arms showing no particular irregular behaviour, where in particular the temperature profiles are generally decreasing functions of radius. The other arms either show signs of large cold fronts between 20 and 50 arcminutes form the center, or showed signs of large scale sloshing motion of the gas [Simionescu et al., 2011, 2012, Urban et al., 2014].

In this work, we consider temperature variations relative to the mean profile, and weigh them by ρr^2 as described in equation 2.12. The $T_{\rm W}$ profiles are seen in the bottom panel of the first column in figure 2.7. Since Perseus is already a comparatively virialised cluster, there are not a couple of sectors that show extremely obvious deviant features from the mean temperature profile. The western arm (magenta) shares more or less no features with the rest, and is

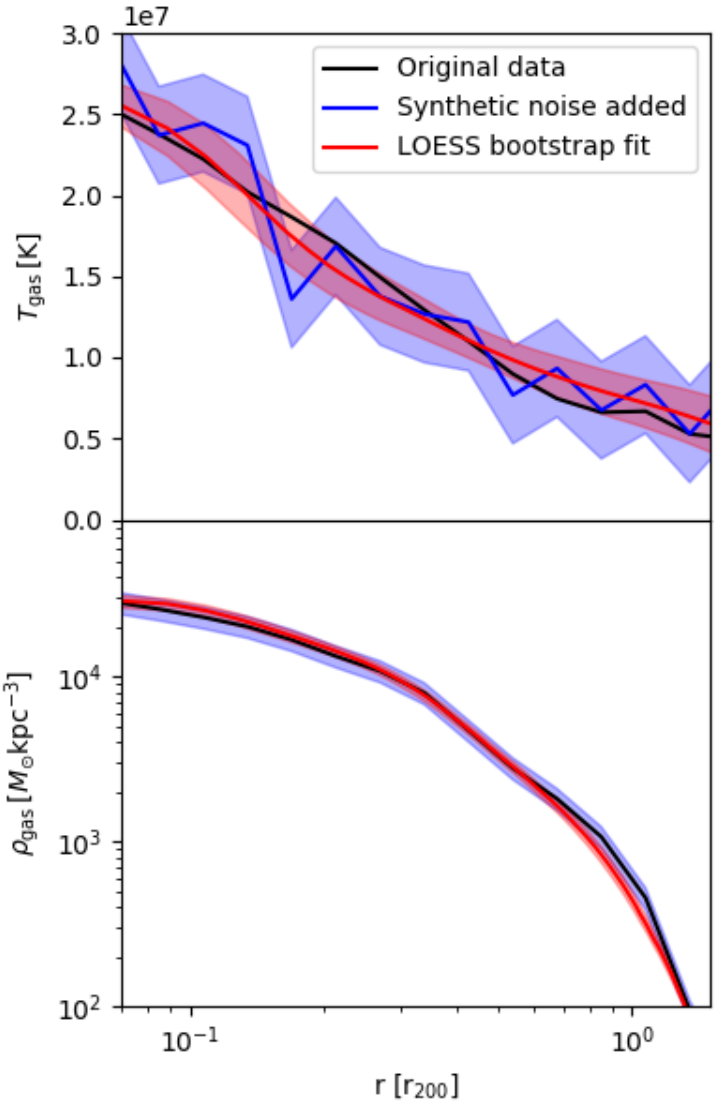

Figure 2.4: Example of the temperature (upper panel) and density (lower panel) LOESS fits employed in the hydrostatic equilibrium calculation for the gas component, as applied to a single clean sector from one of the RAMSES simulated clusters. Top panel shows $T_{\rm gas}$ and bottom panel $\rho_{\rm gas}$. Black lines show the original profiles. The blue curves and patches shows the profile with synthetic noise and errorbars added, and the red curves shows the median and 68% percentile of 100 bootstrap resampled Monte Carlo LOESS fits to the noisy profiles.

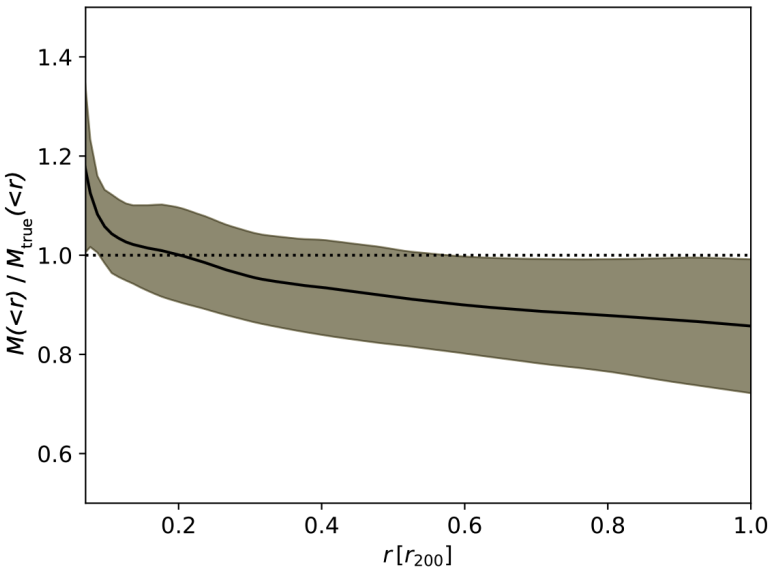

Figure 2.5: The mass profiles from hydrostatic equilibrium for all sectors of the 6 RAMSES clusters relative to the true mass profile of the cluster they belong to. The black curve represents a LOESS fit to the individual profiles, and the grey band represents the $1\,\sigma$ standard deviation of the profiles, as obtained from the generalized cross-validation technique of the LOESS fit outlined in the main text.

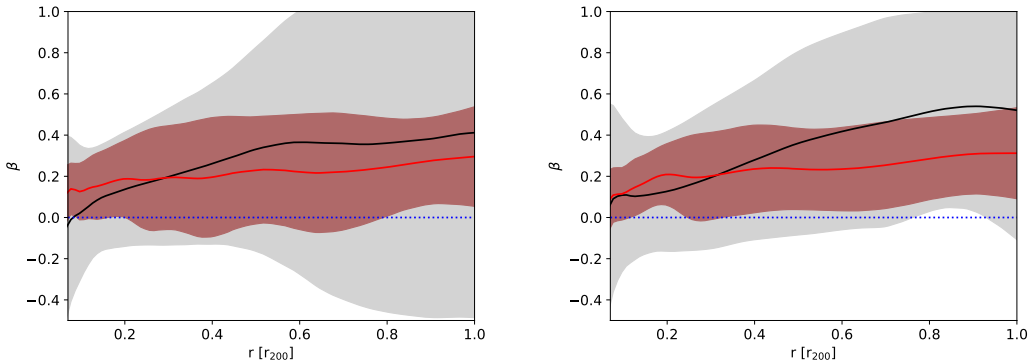

Figure 2.6: β profile for all sectors (left) and selected sectors (right) for the six relaxed RAMSES clusters using interpolated 2D smoothing spline κ-profiles for each cluster. Red curve shows a LOESS fit to the true β-profiles, and black curves to inferred ones. The red narrow patches indicate the 1σ standard deviation of the true β-profiles, and the light grey wider patches indicated the same but for the inferred β-profiles, as obtained through the generalized cross validation technique of the LOESS fit outlined in the main text. Thus the standard deviations shown here is for a single sector of a single cluster.

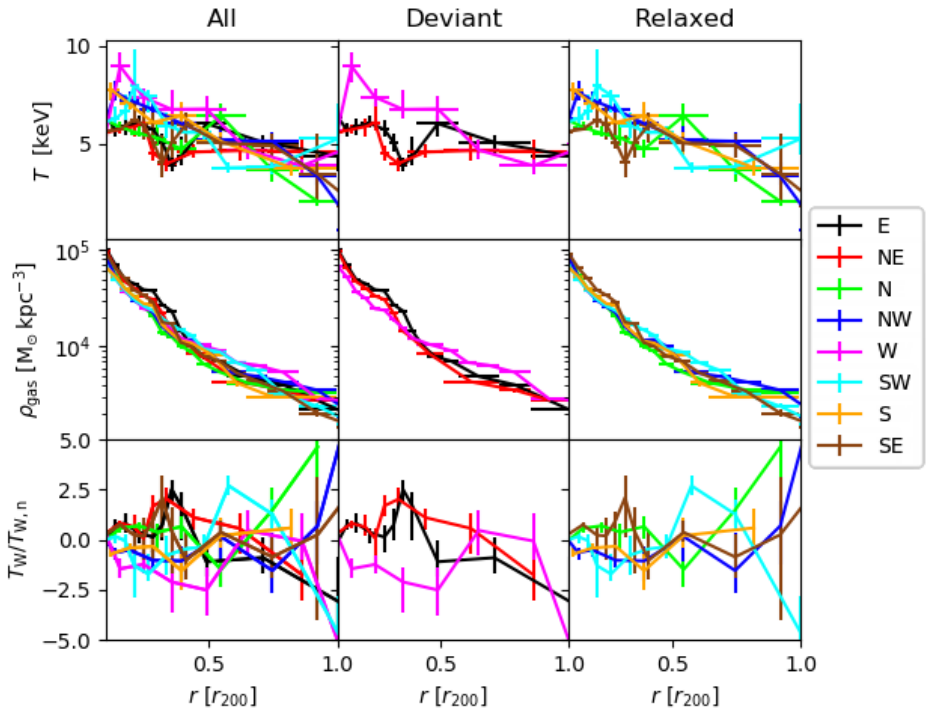

Figure 2.7: Deprojected profiles for the 8 sectors of the Perseus cluster, grouped in categories through columns "All", "Deviant" and "Relaxed". Top row shows the gas temperature $T_{\rm gas}$, center row the gas density $\rho_{\rm gas}$ and bottom row the weighted temperature variation $T_{\rm W}$.

arguably not in equilibrium with the remaining parts of the cluster. Beyond $0.7\,r_{200}$ the spread of the profiles becomes very large and the profiles deviate significantly from each other. Within $0.7\,r_{200}$ the Eastern (black), North Eastern (red) and to a lesser extent the South Eastern (brown) arms display an irregularity that Urban et. al conclude to be a cold front. Here we shall remove Eastern and North Eastern arms, the ones furthest from the mean temperature profile below $0.5r_{200}$ and with a general downwards tendency beyond r_{200} in the $T_{\rm W}$ profiles (figure 2.7 bottom row central column). Instead we focus on the remaining 5 profiles closer to the mean below r_{200} and with the upwards tendency in the $T_{\rm W}$ profiles beyond r_{200} (figure 2.7 bottom row 3rd column). Then we are consistent with the methodology of the previous sections, where the numerical clusters were considered, and arrive at the selections in the 3rd column of figure 2.7. The middle column shows the profiles that are not included in the analysis.

This leaves us with three sets of data within Perseus: The full set, the sectors selected here and the ones found to be relaxed by previous analysis [Urban et al., 2014]. In the following section we examine all three sets. Each arm is fed through our analysis separately, and in the end we stack the β of each set to obtain an overall inference of β from Perseus.

We do not consider radii outside the virial radius, where the infall motion leads to departure from hydrostatic equilibrium [Falco et al., 2013, Albæk et al., 2017].

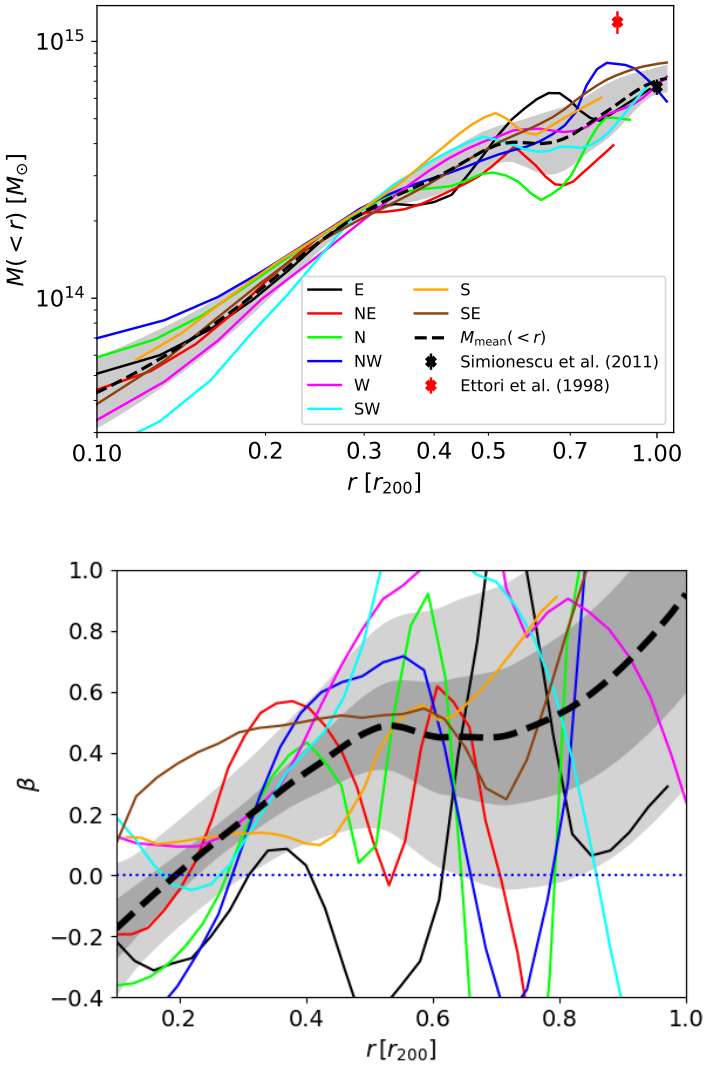

Figure 2.8: Top: Mass profiles for the 8 sectors of Perseus as obtained from hydrostatic equilibrium. Gray band shows the 1σ spread of the individual profiles. Note the logarithmic r-axis. The red point at 0.85 r_{200} shows the Perseus mass estimate from Ettori, with errorbars showing the 10% and 90% from an MC fitting of a β profile to ROSAT data. The blue point at 1.0 r_{200} shows the mass estimate and 1σ errorbars of Simionescu et al. [2011], which is based on NFW-profile fits of the Suzaku data of the North-Western and Eastern arms only. We note that while our findings do not agree with those of Ettori, they are in agreement with the Simionescu et al. [2011] result. Bottom: Calculated $\beta(r)$ profiles for the same directions arms. Dark grey band represents the uncertainty of the mean β profile based on the spread of the Perseus sample ($\frac{\sigma}{\sqrt{N}}$ where N is number of sectors), and and light grey is the added uncertainty of the mean based on the standard deviation of the RAMSES full set i.e. the grey area of the LHS panel of figure 2.6.

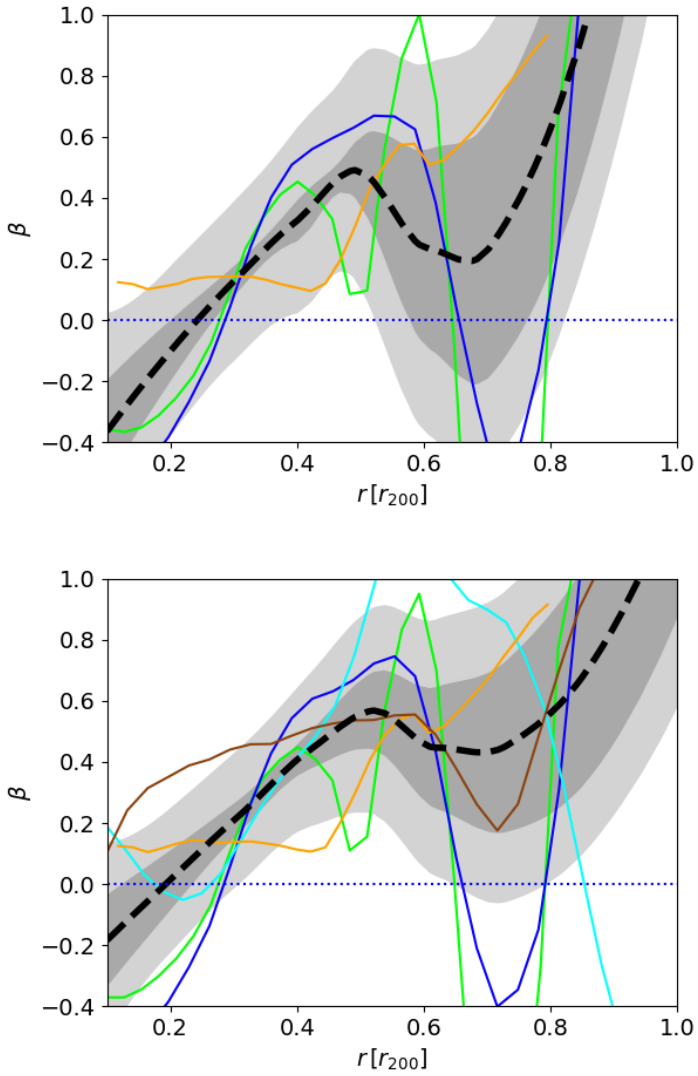

Figure 2.9: Top: $\beta(r)$ using only the selected 3 sectors which are classified as "Relaxed" in [Urban et al., 2014]. Bottom: $\beta(r)$ using the 5 equilibrated sectors according to section 2.9 above. In both figures, the black dashed curve shows LOESS fit to the profiles. The dark grey inner band shows the uncertainty of the mean $\frac{\sigma}{\sqrt{N}}$, where σ is the spread as obtained through LOESS generalized cross validation, and N is the number of sectors included. The light grey outer band shows the added uncertainty from spread of the RHS of figure 2.6, i.e. the uncertainty from the inference technique itself. For each sector, multiple β profiles are calculated via the analytical framework and MC bootstrap procedure described in the paper. Slight variations upon each MC realisation occurs, and so the profiles may be slightly different between realisations.

2.10 Extracting the DM velocity anisotropy in Perseus

Having prepared a method for data selection in the previous sections, and determined 3 sets of sectors for the Perseus cluster to investigate, we are now ready to extract β from it. We use the deprojected observations of $T_{\rm gas}$ and $\rho_{\rm gas}$ profiles and their corresponding error-bars to perform a Monte Carlo sampling as input for the analysis for each sector i.e. each arm. First $\frac{\partial \ln \rho_{\rm gas}}{\partial \ln r}$ and $\frac{\partial \ln T_{\rm gas}}{\partial \ln r}$ are found at each radial point by computing central differences in the interior and first differences at the boundaries. These are then used in the hydrostatic equilibrium equation to calculate the mass profile. This mass profile is again subjected to a non-parametric LOESS fit in order to smooth out bumps and wiggles. After subtracting the gas mass, we can directly generate the DM density profile. The resulting mass profile of Perseus can be seen in figure 2.8 using the data from all 8 arms. For each Monte Carlo sampling a DM temperature profile is also resampled based on the smoothing spline κ surface and errors of figure 2.1, and the resampled gas temperature profile. The $\sigma_r^2(r)$ profiles can now be calculated for each sample, and hence the $\beta(r)$ profiles.

The results are shown in the bottom panel of figure 2.8 for all 8 arms of Perseus i.e. the full set. The coloured curves represents the $\beta(r)$ median Monte Carlo profiles obtained from the individual sectors of the Perseus data, and the black dashed curve shows another LOESS smoothing to these curves to infer an overall β for the data included. The inner dark grey band shows the 1σ standard error of the mean as obtained via the standard deviation of the LOESS fit, and the light grey outer bands the additional 1σ standard error of the mean from of the standard deviation of the β obtained from the RAMSES mock data as seen in the left side of figure 2.6. We see that the the β profile ranges from 0 in the inner parts towards 1 at r_{200} where uncertainty grows large on the data and the validity of our assumptions, and thus on β.

For the partial sets, we perform the same analysis but include only the 3 sectors of the Urban et. al. set, and the 5 sectors selected through $T_{\rm W}$ profiles. The β can be seen in the left and right panel of figure 2.9 respectively. Here, the grey inner bands represent the same as for the full set, but the outer light grey bands are instead taken from the standard deviation of the right hand side panel of figure 2.6. We see especially for the set chosen here that β is different from 0 between $0.3r_{200}$ and $0.6r_{200}$ beyond its standard error. Including all the error-bars, we have here found indications that the velocity anisotropy in Perseus is of the order

$$\beta_{r=0.5r_{200}} = 0.5 \pm 0.1 \pm 0.2\,, \tag{2.13}$$

where the error-bars are from: variations within the Perseus cluster sectors, and the added scatter from the hydrostatic equilibrium technique itself as applied on each individual arm. This takes the optimistic stand that sectors within a galaxy cluster are completely uncorrelated inferences of β. Taking the more pessimistic viewpoint that sectors within a single cluster are completely correlated yields $\beta_{r=0.5r_{200}} = 0.5 \pm 0.1 \pm 0.3$. This includes uncertainty from temperature measurements and uncertainty in κ. From around $0.6\,r_{200}$ and up to $0.8r_{200}$ the

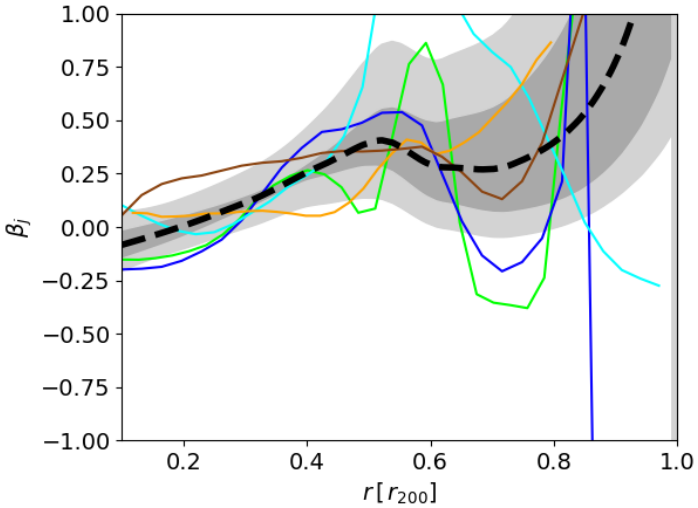

Figure 2.10: The non-standard and symmetrized β_j, which can only assume values between -1 and $+1$, plotted for the 5 sectors of Perseus selected in the present work through $T_{\rm W}$. The black dashed line shows the LOESS fit to the five profiles. The inner and outer grey bands are the standard errors of the mean similarly to the ones of figure 2.8.

inference of β is consistent with 0, and beyond that the error grows as the assumptions of hydrostatic equilibrium breaks down even for the selected clusters and sectors within them. This in fact is already seen in the massprofiles of the RAMSES clusters, where the hydrostatic method has large errorbars at these large radii. Generally β tends to increase with increasing radius. At $r < 0.2r_{200}$ the results are statistically consistent with $\beta = 0$, but if the decrease extends to lower radii, it could be interpreted as an effect of the brightest central galaxy making orbits more tangentially biased. However, this effect should not be visible at the scales examined in this work [Host and Hansen, 2011]. Figure 2.11 compares the Perseus inference to the β profile of the chosen sectors of the RAMSES clusters, and again we see, for this single Perseus inference, that observation and simulation agrees within r_{200}.

It is worth keeping in mind that β in principle could take on any value between $+1$ and $-\infty$. The simulated values of β from these 51 RAMSES clusters are about 0.25 at $r = 0.5r_{200}$ (with a 1σ spread about 0.2 among the 51 clusters), and at $r \sim r_{200}$ it is about 0.35 (with a dispersion about $^{+0.2}_{-0.4}$). Upon comparing the inferred β with the β of the simulated clusters in figure 2.6 and figure 2.9 respectively we see that they are in reasonable agreement at least until $0.7r_{200}$. Another way to visualize the velocity anisotropy parameter is through joining σ_r^2 and σ_t^2 in the construct

$$\beta_j = \frac{\sigma_r^2 - \sigma_t^2}{\sigma_r^2 + \sigma_t^2} = \frac{\beta}{2 - \beta}, \tag{2.14}$$

which ranges from -1 to 1. Figure 2.10 shows precisely this quantity for the 5 sectors of the Perseus cluster selected here, where the β_j profile with its standard error of the mean is seen to be non-trivial below $0.6r_{200}$.

It should be noted, that in spite of removing data from the analysis, the Perseus resulting β is comparable to that of the one with the full data both in terms of the mean curve and

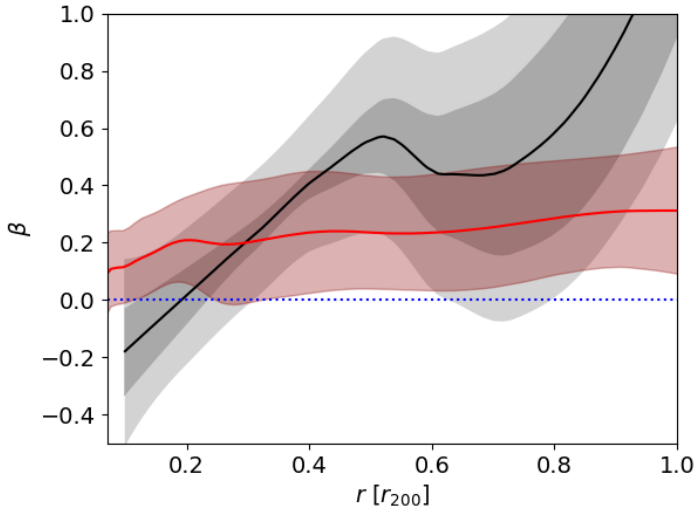

Figure 2.11: Comparison of the true β profile from RAMSES (red curve) and the inferred β profile for Perseus (black curve). The RAMSES profile is comprised of the β profiles of the relaxed sectors of the relaxed clusters as also shown in the RHS panel of figure 2.6. The Perseus profile is the same as shown in the bottom panel of figure 2.9 for the 5 arms selected through our analysis. Again the dark grey inner band shows the uncertainty of the mean $\frac{\sigma}{\sqrt{N}}$, where σ is the standard deviation as obtained through LOESS generalized cross validation, and N is the number of sectors included. The light grey outer band shows the added uncertainty from spread of the RHS of figure 2.6, i.e. the uncertainty from the inference technique itself.

the error. Perseus is itself a virialized cluster, and thus expectations of bettering the beta inference remarkably with this data selection technique are low. However, as multiple clusters are discovered and analyzed through the same technique, our results from the RAMSES simulation show that it is possible to better the uncertainty in β inferences by conducting data selection of the type outlined here. Høst et al. obtained inferences of β within r_{2500} for a stack of 16 clusters observed in X-ray [Host et al., 2009], whereas here we analyze just one single cluster. In the future we hope to include future cluster X-ray observations to high radii to further bring uncertainties down.

2.11 Conclusion

The dark matter velocity anisotropy contains information on the dynamics of dark matter in equilibrated structures. By combining the gas equation from hydrostatic equilibrium and the DM equation i.e. the Jeans equation with input from a numerical cosmological simulation that includes the baryonic component, we are able to test the consistency of the velocity anisotropy inference for Perseus with the dark matter model employed in this simulation. We find that the velocity anisotropy of Perseus is consistent with that of the cosmological model employing a ΛCDM cosmology, lending support to the cold and collisionless nature of DM in galaxy clusters. Our analysis of the Perseus data agrees with previous inferences on the velocity anisotropy. Previous studies employ the strength of a catalogue of 16 galaxy clusters. However, since deprojected gas profiles are requirement of the analysis the results were within 0.85 r_{2500}.

The quality and radial extent of the Perseus data allows us to probe the consistency of the DM model towards the virial radius. By analyzing and including only sectors of the cluster that displays a well behaved radial X-ray signal, we show that we in simulation are able to put better constraints on the velocity anisotropy inferences, however for Perseus we are only able to get meaningful constraints towards $0.6r_{200}$, which is still a large improvement of about a factor of 3 compared to previous work.

The method comes with some caveats: A relation κ from numerical simulations between the gas temperature and the dark matter total velocity dispersion i.e. the "DM temperature" is used to calibrate the inference of the dark matter velocity anisotropy. The inferred velocity anisotropy of a galaxy cluster in observation is only ever as good as the κ that it is calibrated against. Since we assume a DM model in all cosmological simulations we at best are able to infer velocity anisotropy as relying on the assumptions of the simulation. Therefore, our velocity anisotropy inference should be viewed as a check of consistency with the model employed in the estimation of the total DM velocity dispersion. Furthermore, the Perseus data comprises just a single galaxy cluster. To obtain better constraints on the dark matter velocity anisotropy is a statistical challenge, and even a couple of galaxy cluster data sets of the same quality would strengthen the analysis greatly.

Our final remarks concern future analyses. Above we have made the assumption of hydrostatic equilibrium. It is well known that departure from hydrostatic equilibrium impacts the mass determinations, see e.g. Nelson et al. [2014] for a list of references, and also that the velocity anisotropy directly or through mass profiles may depend on orientation [Sparre and Hansen, 2012, Wojtak et al., 2013, Svensmark et al., 2015]. We also assume sphericity of the cluster which have previously been found to impact mass estimates of clusters. Perseus was chosen because it does have a relaxed appearance, and we have chosen only the 5 most relaxed arms. Furthermore, at the moment the large scatter in κ leads to large error-bars of β. By analysing cones in numerical simulated clusters, for instance separating according to differences in temperature profiles such as cool-core (CC) and non-CC cones, one might be able to reduce scatter in κ, and hence obtain smaller error-bars of the DM β.

Few alternative methods to estimate the DM velocity anisotropy exits [Lemze et al., 2012, Mamon et al., 2013]. Future analyses which would improve on the method discussed here, could be forced to attempt to improve on the mass determination by including complementary observation e.g. from lensing or the SZ effect [Kneib and Natarajan, 1996, Stark et al., 2017]. Here one will, however, have to deal with the difficult systematic effects when combining such different observational techniques.

Acknowledgements

It is a pleasure thanking Ondrej Urban for providing the data from Perseus. We thank Adam Mantz, Aurora Simionescu and Ondrej Urban for constructive suggestions. SHH wishes to thank Christoffer Bruun-Schmidt, Beatriz Soret and Lasse Albæk for discussions. This

project is partially funded by the Danish council for independent research under the project “Fundamentals of Dark Matter Structures”, DFF - 6108-00470.

Bibliography

P. Agnes, T. Alexander, A. Alton, K. Arisaka, H.O. Back, B. Baldin, K. Biery, G. Bonfini, M. Bossa, A. Brigatti, J. Brodsky, F. Budano, L. Cadonati, F. Calaprice, N. Canci, A. Candela, H. Cao, M. Cariello, P. Cavalcante, A. Chavarria, A. Chepurnov, A.G. Cocco, L. Crippa, D. D'Angelo, M. D'Incecco, S. Davini, M. De Deo, A. Derbin, A. Devoto, F. Di Eusanio, G. Di Pietro, E. Edkins, A. Empl, A. Fan, G. Fiorillo, K. Fomenko, G. Forster, D. Franco, F. Gabriele, C. Galbiati, A. Goretti, L. Grandi, M. Gromov, M.Y. Guan, Y. Guardincerri, B. Hackett, K. Herner, E.V. Hungerford, Al. Ianni, An. Ianni, C. Jollet, K. Keeter, C. Kendziora, S. Kidner, V. Kobychev, G. Koh, D. Korablev, G. Korga, A. Kurlej, P.X. Li, B. Loer, P. Lombardi, C. Love, L. Ludhova, S. Luitz, Y.Q. Ma, I. Machulin, A. Mandarano, S. Mari, J. Maricic, L. Marini, C.J. Martoff, A. Meregaglia, E. Meroni, P.D. Meyers, R. Milincic, D. Montanari, A. Monte, M. Montuschi, M.E. Monzani, P. Mosteiro, B. Mount, V. Muratova, P. Musico, A. Nelson, S. Odrowski, M. Okounkova, M. Orsini, F. Ortica, L. Pagani, M. Pallavicini, E. Pantic, L. Papp, S. Parmeggiano, R. Parsells, K. Pelczar, N. Pelliccia, S. Perasso, A. Pocar, S. Pordes, D. Pugachev, H. Qian, K. Randle, G. Ranucci, A. Razeto, B. Reinhold, A. Renshaw, A. Romani, B. Rossi, N. Rossi, S.D. Rountree, D. Sablone, P. Saggese, R. Saldanha, W. Sands, S. Sangiorgio, E. Segreto, D. Semenov, E. Shields, M. Skorokhvatov, O. Smirnov, A. Sotnikov, C. Stanford, Y. Suvorov, R. Tartaglia, J. Tatarowicz, G. Testera, A. Tonazzo, E. Unzhakov, R.B. Vogelaar, M. Wada, S. Walker, H. Wang, Y. Wang, A. Watson, S. Westerdale, M. Wojcik, A. Wright, X. Xiang, J. Xu, C.G. Yang, J. Yoo, S. Zavatarelli, A. Zec, C. Zhu, and G. Zuzel. First results from the darkside-50 dark matter experiment at laboratori nazionali del gran sasso. *Physics Letters B*, 743:456 – 466, 2015. ISSN 0370-2693. doi: https://doi.org/10.1016/j.physletb.2015.03.012. URL `http://www.sciencedirect.com/science/article/pii/S0370269315001756`.

L. Albæk, S. H. Hansen, D. Martizzi, B. Moore, and R. Teyssier. Infall near clusters of galaxies: comparing gas and dark matter velocity profiles. *Monthly Notices of the Royal Astronomical Society*, 472(3):3486–3491, 2017. doi: 10.1093/mnras/stx2139. URL `http://dx.doi.org/10.1093/mnras/stx2139`.

N. C. Amorisco, J. Zavala, and T. J. L. de Boer. Dark matter cores in the fornax and sculptor dwarf galaxies: Joining halo assembly and detailed star formation histories. *The Astrophysical Journal Letters*, 782(2):L39, 2014. URL `http://stacks.iop.org/2041-8205/782/i=2/a=L39`.

Thomas J Armitage, Scott T Kay, David J Barnes, Yannick M Bahé, and Claudio Dalla Vecchia. The Cluster-EAGLE project: a comparison of dynamical mass estimators using simulated

clusters. *Monthly Notices of the Royal Astronomical Society*, 482(3):3308–3325, 10 2018. ISSN 0035-8711. doi: 10.1093/mnras/sty2921. URL https://dx.doi.org/10.1093/mnras/sty2921.

ATLAS Collaboration, G. Aad, B. Abbott, J. Abdallah, and S. Abdel Khalek. Search for dark matter in events with heavy quarks and missing transverse momentum in $$pp$$ppcollisions with the atlas detector. *The European Physical Journal C*, 75(2):92, 02 2015. ISSN 1434-6052. doi: 10.1140/epjc/s10052-015-3306-z. URL https://doi.org/10.1140/epjc/s10052-015-3306-z.

Alejandro Benitez-Llambay, Carlos S. Frenk, Aaron D. Ludlow, and Julio F. Navarro. Baryon-induced dark matter cores in the EAGLE simulations. *arXiv e-prints*, art. arXiv:1810.04186, 10 2018.

Gianfranco Bertone and Dan Hooper. History of dark matter. *Reviews of Modern Physics*, 90 (4):045002, October 2018. doi: 10.1103/RevModPhys.90.045002.

J. Binney and S. Tremaine. *Galactic Dynamics: Second Edition*. Princeton University Press, 2008.

Céline Bœhm, Alain Riazuelo, Steen H. Hansen, and Richard Schaeffer. Interacting dark matter disguised as warm dark matter. *Phys. Rev. D*, 66:083505, 10 2002. doi: 10.1103/PhysRevD.66.083505. URL https://link.aps.org/doi/10.1103/PhysRevD.66.083505.

J. Richard Bond, Lev Kofman, and Dmitry Pogosyan. How filaments of galaxies are woven into the cosmic web. *Nature*, 380(6575):603–606, April 1996. doi: 10.1038/380603a0.

Sownak Bose, Carlos S. Frenk, Adrian Jenkins, Azadeh Fattahi, Facundo A. Gomez, Robert J. J. Grand, Federico Marinacci, Julio F. Navarro, Kyle A. Oman, Ruediger Pakmor, Joop Schaye, Christine M. Simpson, and Volker Springel. No cores in dark matter-dominated dwarf galaxies with bursty star formation histories. *arXiv e-prints*, art. arXiv:1810.03635, 10 2018.

Thejs Brinckmann, Jesús Zavala, David Rapetti, Steen H. Hansen, and Mark Vogelsberger. The structure and assembly history of cluster-sized haloes in self-interacting dark matter. *Monthly Notices of the Royal Astronomical Society*, 474(1):746–759, 2018. doi: 10.1093/mnras/stx2782. URL http://dx.doi.org/10.1093/mnras/stx2782.

James S. Bullock, Jose Oñorbe, Michael Boylan-Kolchin, Philip F. Hopkins, Dušan Kereš, Claude-André Faucher-Giguère, Eliot Quataert, and Norman Murray. Forged in fire: cusps, cores and baryons in low-mass dwarf galaxies. *Monthly Notices of the Royal Astronomical Society*, 454(2):2092–2106, 10 2015. ISSN 0035-8711. doi: 10.1093/mnras/stv2072. URL https://dx.doi.org/10.1093/mnras/stv2072.

Douglas Clowe, Maruša Bradač, Anthony H. Gonzalez, Maxim Markevitch, Scott W. Randall, Christine Jones, and Dennis Zaritsky. A direct empirical proof of the existence of dark matter. *The Astrophysical Journal Letters*, 648(2):L109, 2006. URL http://stacks.iop.org/1538-4357/648/i=2/a=L109.

Jan Conrad and Olaf Reimer. Indirect dark matter searches in gamma and cosmic rays. *Nature Physics*, 13(3):224–231, March 2017. doi: 10.1038/nphys4049.

Arianna Di Cintio, Michael Tremmel, Fabio Governato, Andrew Pontzen, Jesús Zavala, Alexander Bastidas Fry, Alyson Brooks, and Mark Vogelsberger. A rumble in the dark: signatures of self-interacting dark matter in supermassive black hole dynamics and galaxy density profiles. *Monthly Notices of the Royal Astronomical Society*, 469(3):2845–2854, 2017. doi: 10.1093/mnras/stx1043. URL http://dx.doi.org/10.1093/mnras/stx1043.

Aaron A. Dutton, Andrea V. Macciò, Tobias Buck, Keri L. Dixon, Marvin Blank, and Aura Obreja. NIHAO XX: The impact of the star formation threshold on the cusp-core transformation of cold dark matter haloes. *arXiv e-prints*, art. arXiv:1811.10625, 11 2018.

Ettori.

S. Ettori, V. Ghirardini, D. Eckert, E. Pointecouteau, F. Gastaldello, M. Sereno, M. Gaspari, S. Ghizzardi, M. Roncarelli, and M. Rossetti. Hydrostatic mass profiles in X-COP galaxy clusters. *Astronomy and Astrophysics*, 621:A39, January 2019. doi: 10.1051/0004-6361/201833323.

C. Faham. First Dark Matter Search Results from the Large Underground Xenon (LUX) Experiment. *ArXiv e-prints*, May 2014.

Martina Falco, Gary A. Mamon, Radoslaw Wojtak, Steen H. Hansen, and Stefan Gottlöber. Dynamical signatures of infall around galaxy clusters: a generalized jeans equation. *Monthly Notices of the Royal Astronomical Society*, 436(3):2639–2649, 2013. doi: 10.1093/mnras/stt1768. URL http://dx.doi.org/10.1093/mnras/stt1768.

Alex Fitts, Michael Boylan-Kolchin, Brandon Bozek, James S. Bullock, Andrew Graus, Victor Robles, Philip F. Hopkins, Kareem El-Badry, Shea Garrison-Kimmel, Claude-André Faucher-Giguère, Andrew Wetzel, and Dušan Kereš. Dwarf Galaxies in CDM, WDM, and SIDM: Disentangling Baryons and Dark Matter Physics. *arXiv e-prints*, art. arXiv:1811.11791, 11 2018.

Daniel Gifford and Christopher J. Miller. VELOCITY ANISOTROPY AND SHAPE BIAS IN THE CAUSTIC TECHNIQUE. *The Astrophysical Journal*, 768(2):L32, 04 2013. doi: 10.1088/2041-8205/768/2/l32.

Gerard Gilmore, Mark I. Wilkinson, Rosemary F. G. Wyse, Jan T. Kleyna, Andreas Koch, N. Wyn Evans, and Eva K. Grebel. The observed properties of dark matter on small spatial scales. *The Astrophysical Journal*, 663(2):948, 2007. URL http://stacks.iop.org/0004-637X/663/i=2/a=948.

Alejandro González-Samaniego, Oliver D. Elbert, James S. Bullock, Victor H. Robles, Alex Fitts, Michael Boylan-Kolchin, Philip F. Hopkins, Christopher C. Hayward, Claude-André Faucher-Giguère, and Dušan Kereš. SIDM on fire: hydrodynamical self-interacting dark matter simulations of low-mass dwarf galaxies. *Monthly Notices of the Royal Astronomical Society*, 472(3):2945–2954, 09 2017. ISSN 0035-8711. doi: 10.1093/mnras/stx2253. URL https://dx.doi.org/10.1093/mnras/stx2253.

Steen H. Hansen. Might we eventually understand the origin of the dark matter velocity anisotropy? *The Astrophysical Journal*, 694(2):1250, 2009. URL http://stacks.iop.org/0004-637X/694/i=2/a=1250.

Steen H. Hansen, Ben Moore, Marcel Zemp, and Joachim Stadel. A universal velocity distribution of relaxed collisionless structures. *J. Cosmology Astropart. Phys.*, 2006(1):014, January 2006. doi: 10.1088/1475-7516/2006/01/014.

Steen H. Hansen, Andrea V. Macció, Emilio Romano-Diaz, Yehuda Hoffman, Marcus Brüggen, Evan Scannapieco, and Greg S. Stinson. The temperature of hot gas in galaxies and clusters: Baryons dancing to the tune of dark matter. *The Astrophysical Journal*, 734(1):62, 2011. URL http://stacks.iop.org/0004-637X/734/i=1/a=62.

Hansen, S. H. and Piffaretti, R. Measuring the dark matter velocity anisotropy in galaxy clusters. *A&A*, 476(3):L37–L40, 2007. doi: 10.1051/0004-6361:20078656. URL https://doi.org/10.1051/0004-6361:20078656.

G. Hinshaw, D. Larson, E. Komatsu, D. N. Spergel, C. L. Bennett, J. Dunkley, M. R. Nolta, M. Halpern, R. S. Hill, N. Odegard, L. Page, K. M. Smith, J. L. Weiland, B. Gold, N. Jarosik, A. Kogut, M. Limon, S. S. Meyer, G. S. Tucker, E. Wollack, and E. L. Wright. Nine-year wilkinson microwave anisotropy probe (wmap) observations: Cosmological parameter results. *The Astrophysical Journal Supplement Series*, 208(2):19, 2013. URL http://stacks.iop.org/0067-0049/208/i=2/a=19.

Ole Host and Steen H. Hansen. A DETAILED STATISTICAL ANALYSIS OF THE MASS PROFILES OF GALAXY CLUSTERS. *The Astrophysical Journal*, 736(1):52, 07 2011. doi: 10.1088/0004-637x/736/1/52. URL https://doi.org/10.1088%2F0004-637x%2F736%2F1%2F52.

Ole Host, Steen H. Hansen, Rocco Piffaretti, Andrea Morandi, Stefano Ettori, Scott T. Kay, and Riccardo Valdarnini. Measurement of the dark matter velocity anisotropy in galaxy clusters. *The Astrophysical Journal*, 690(1):358, 2009. URL http://stacks.iop.org/0004-637X/690/i=1/a=358.

Scott T. Kay, Antonio C. Da Silva, Nabila Aghanim, Alain Blanchard, Andrew R. Liddle, Jean-Loup Puget, Rachida Sadat, and Peter A. Thomas. The evolution of clusters in the CLEF cosmological simulation: X-ray structural and scaling properties. *Monthly Notices of the Royal Astronomical Society*, 377(1):317–334, 04 2007. ISSN 0035-8711. doi: 10.1111/j.1365-2966.2007.11605.x. URL https://doi.org/10.1111/j.1365-2966.2007.11605.x.

Jean-Paul Kneib and Priyamvada Natarajan. Probing the dynamics of cluster-lenses. *Monthly Notices of the Royal Astronomical Society*, 283(3):1031–1046, 12 1996. ISSN 0035-8711. doi: 10.1093/mnras/283.3.1031. URL https://dx.doi.org/10.1093/mnras/283.3.1031.

Edward W. Kolb and Michael S. Turner. *The early universe*, volume 69. 1990.

Doron Lemze, Rick Wagner, Yoel Rephaeli, Sharon Sadeh, Michael L. Norman, Rennan Barkana, Tom Broadhurst, Holland Ford, and Marc Postman. PROFILES OF DARK MATTER VELOCITY ANISOTROPY IN SIMULATED CLUSTERS. *The Astrophysical Journal*, 752(2):141, 06 2012. doi: 10.1088/0004-637x/752/2/141. URL https://doi.org/10.1088%2F0004-637x%2F752%2F2%2F141.

Hongwan Liu, Tracy R. Slatyer, and Jesús Zavala. Contributions to cosmic reionization from dark matter annihilation and decay. *Phys. Rev. D*, 94:063507, 09 2016. doi: 10.1103/PhysRevD.94.063507. URL https://link.aps.org/doi/10.1103/PhysRevD.94.063507.

S. Lowette and for the CMS Collaboration. Search for Dark Matter at CMS. *ArXiv e-prints*, 10 2014.

K. Lundmark. Über die Bestimmung der Entfernungen, Dimensionen, Massen und Dichtigkeit fur die nächstgelegenen anagalacktischen Sternsysteme. *Meddelanden fran Lunds Astronomiska Observatorium Serie I*, 125:1–13, January 1930.

Gary A. Mamon, Gwenaël Boué, and Andrea Biviano. MAMPOSSt: Modelling Anisotropy and Mass Profiles of Observed Spherical Systems – I. Gaussian 3D velocities. *Monthly Notices of the Royal Astronomical Society*, 429(4):3079–3098, 01 2013. ISSN 0035-8711. doi: 10.1093/mnras/sts565. URL https://dx.doi.org/10.1093/mnras/sts565.

Maxim Markevitch and Alexey Vikhlinin. Shocks and cold fronts in galaxy clusters. *Physics Reports*, 443(1):1 – 53, 2007. ISSN 0370-1573. doi: https://doi.org/10.1016/j.physrep.2007.01.001. URL http://www.sciencedirect.com/science/article/pii/S0370157307000695.

Davide Martizzi and Harrison Agrusa. Mass modeling of galaxy clusters: quantifying hydrostatic bias and contribution from non-thermal pressure. *arXiv e-prints*, art. arXiv:1608.04388, 08 2016.

Davide Martizzi, Irshad Mohammed, Romain Teyssier, and Ben Moore. The biasing of baryons on the cluster mass function and cosmological parameter estimation. *Monthly Notices of the Royal Astronomical Society*, 440(3):2290–2299, 2014. doi: 10.1093/mnras/stu440. URL http://dx.doi.org/10.1093/mnras/stu440.

Julio F. Navarro, Carlos S. Frenk, and Simon D. M. White. The Structure of Cold Dark Matter Halos. *The Astrophysical Journal*, 462:563, May 1996. doi: 10.1086/177173.

Julio F. Navarro, Aaron Ludlow, Volker Springel, Jie Wang, Mark Vogelsberger, Simon D. M. White, Adrian Jenkins, Carlos S. Frenk, and Amina Helmi. The diversity and similarity of simulated cold dark matter haloes. *Monthly Notices of the Royal Astronomical Society*, 402 (1):21–34, 2010. doi: 10.1111/j.1365-2966.2009.15878.x. URL http://dx.doi.org/10.1111/j.1365-2966.2009.15878.x.

Kaylea Nelson, Erwin T. Lau, and Daisuke Nagai. HYDRODYNAMIC SIMULATION OF NON-THERMAL PRESSURE PROFILES OF GALAXY CLUSTERS. *The Astrophysical Journal*, 792 (1):25, 08 2014. doi: 10.1088/0004-637x/792/1/25. URL https://doi.org/10.1088%2F0004-637x%2F792%2F1%2F25.

J. H. Oort. The force exerted by the stellar system in the direction perpendicular to the galactic plane and some related problems. *Bulletin Astronomical Institute of the Netherlands*, 6:249, August 1932.

Planck Collaboration, N. Aghanim, Y. Akrami, M. Ashdown, J. Aumont, C. Baccigalupi, M. Ballardini, A. J. Banday, R. B. Barreiro, N. Bartolo, S. Basak, R. Battye, K. Benabed, J. P. Bernard, M. Bersanelli, P. Bielewicz, J. J. Bock, J. R. Bond, J. Borrill, F. R. Bouchet, F. Boulanger, M. Bucher, C. Burigana, R. C. Butler, E. Calabrese, J. F. Cardoso, J. Carron, A. Challinor, H. C. Chiang, J. Chluba, L. P. L. Colombo, C. Combet, D. Contreras, B. P. Crill, F. Cuttaia, P. de Bernardis, G. de Zotti, J. Delabrouille, J. M. Delouis, E. Di Valentino,

J. M. Diego, O. Dore, M. Douspis, A. Ducout, X. Dupac, S. Dusini, G. Efstathiou, F. Elsner, T. A. Ensslin, H. K. Eriksen, Y. Fantaye, M. Farhang, J. Fergusson, R. Fernandez-Cobos, F. Finelli, F. Forastieri, M. Frailis, E. Franceschi, A. Frolov, S. Galeotta, S. Galli, K. Ganga, R. T. Genova-Santos, M. Gerbino, T. Ghosh, J. Gonzalez-Nuevo, K. M. Gorski, S. Gratton, A. Gruppuso, J. E. Gudmundsson, J. Hamann, W. Handley, D. Herranz, E. Hivon, Z. Huang, A. H. Jaffe, W. C. Jones, A. Karakci, E. Keihanen, R. Keskitalo, K. Kiiveri, J. Kim, T. S. Kisner, L. Knox, N. Krachmalnicoff, M. Kunz, H. Kurki-Suonio, G. Lagache, J. M. Lamarre, A. Lasenby, M. Lattanzi, C. R. Lawrence, M. Le Jeune, P. Lemos, J. Lesgourgues, F. Levrier, A. Lewis, M. Liguori, P. B. Lilje, M. Lilley, V. Lindholm, M. Lopez-Caniego, P. M. Lubin, Y. Z. Ma, J. F. Macias-Perez, G. Maggio, D. Maino, N. Mandolesi, A. Mangilli, A. Marcos-Caballero, M. Maris, P. G. Martin, M. Martinelli, E. Martinez-González, S. Matarrese, N. Mauri, J. D. McEwen, P. R. Meinhold, A. Melchiorri, A. Mennella, M. Migliaccio, M. Millea, S. Mitra, M. A. Miville-Deschênes, D. Molinari, L. Montier, G. Morgante, A. Moss, P. Natoli, H. U. Norgaard-Nielsen, L. Pagano, D. Paoletti, B. Partridge, G. Patanchon, H. V. Peiris, F. Perrotta, V. Pettorino, F. Piacentini, L. Polastri, G. Polenta, J. L. Puget, J. P. Rachen, M. Reinecke, M. Remazeilles, A. Renzi, G. Rocha, C. Rosset, G. Roudier, J. A. Rubino-Martin, B. Ruiz-Granados, L. Salvati, M. Sandri, M. Savelainen, D. Scott, E. P. S. Shellard, C. Sirignano, G. Sirri, L. D. Spencer, R. Sunyaev, A. S. Suur-Uski, J. A. Tauber, D. Tavagnacco, M. Tenti, L. Toffolatti, M. Tomasi, T. Trombetti, L. Valenziano, J. Valiviita, B. Van Tent, L. Vibert, P. Vielva, F. Villa, N. Vittorio, B. D. Wandelt, I. K. Wehus, M. White, S. D. M. White, A. Zacchei, and A. Zonca. Planck 2018 results. VI. Cosmological parameters. *arXiv e-prints*, art. arXiv:1807.06209, 06 2018.

Pointecouteau, E., Arnaud, M., and Pratt, G. W. The structural and scaling properties of nearby galaxy clusters - i. the universal mass profile. *A&A*, 435(1):1–7, 2005. doi: 10.1051/0004-6361:20042569. URL `https://doi.org/10.1051/0004-6361:20042569`.

Vera C. Rubin and Jr. Ford, W. Kent. Rotation of the Andromeda Nebula from a Spectroscopic Survey of Emission Regions. *The Astrophysical Journal*, 159:379, February 1970. doi: 10.1086/150317.

P. Salucci, A. Lapi, C. Tonini, G. Gentile, I. Yegorova, and U. Klein. The universal rotation curve of spiral galaxies – ii. the dark matter distribution out to the virial radius. *Monthly Notices of the Royal Astronomical Society*, 378(1):41–47, 2007. doi: 10.1111/j.1365-2966.2007.11696.x. URL `http://dx.doi.org/10.1111/j.1365-2966.2007.11696.x`.

Isabel M. Santos-Santos, Arianna Di Cintio, Chris B. Brook, Andrea Macciò, Aaron Dutton, and Rosa Domínguez-Tenreiro. NIHAO – XIV. Reproducing the observed diversity of dwarf galaxy rotation curve shapes in ΛCDM. *Monthly Notices of the Royal Astronomical Society*, 473(4):4392–4403, 10 2017. ISSN 0035-8711. doi: 10.1093/mnras/stx2660. URL `https://dx.doi.org/10.1093/mnras/stx2660`.

Craig L. Sarazin. X-ray emission from clusters of galaxies. *Rev. Mod. Phys.*, 58:1–115, 01 1986. doi: 10.1103/RevModPhys.58.1. URL `https://link.aps.org/doi/10.1103/RevModPhys.58.1`.

Luca Scrucca. Model-based sir for dimension reduction. *Computational Statistics & Data Analysis*, 5(11):3010–3026, 2011.

A. Simionescu, N. Werner, O. Urban, S. W. Allen, A. C. Fabian, J. S. Sanders, A. Mantz, P. E. J. Nulsen, and Y. Takei. LARGE-SCALE MOTIONS IN THE PERSEUS GALAXY CLUSTER. *The Astrophysical Journal*, 757(2):182, 09 2012. doi: 10.1088/0004-637x/757/2/182. URL https://doi.org/10.1088%2F0004-637x%2F757%2F2%2F182.

Aurora Simionescu, Steven W. Allen, Adam Mantz, Norbert Werner, Yoh Takei, R. Glenn Morris, Andrew C. Fabian, Jeremy S. Sanders, Paul E. J. Nulsen, Matthew R. George, and Gregory B. Taylor. Baryons at the edge of the x-ray–brightest galaxy cluster. *Science*, 331(6024):1576–1579, 2011. ISSN 0036-8075. doi: 10.1126/science.1200331. URL http://science.sciencemag.org/content/331/6024/1576.

Martin Sparre and Steen H. Hansen. Asymmetric velocity anisotropies in remnants of collisionless mergers. *Journal of Cosmology and Astroparticle Physics*, 2012(07):042, 2012. URL http://stacks.iop.org/1475-7516/2012/i=07/a=042.

Alejo Stark, Christopher J. Miller, and Vitali Halenka. Deriving galaxy cluster velocity anisotropy profiles from a joint analysis of dynamical and weak lensing data. *arXiv e-prints*, art. arXiv:1711.10018, 11 2017.

Jacob Svensmark, Steen H. Hansen, and Radoslaw Wojtak. Effect of asphericity in caustic mass estimates of galaxy clusters. *Monthly Notices of the Royal Astronomical Society*, 448 (2):1644–1659, 02 2015. ISSN 0035-8711. doi: 10.1093/mnras/stu2686. URL https://dx.doi.org/10.1093/mnras/stu2686.

Romain Teyssier, Andrew Pontzen, Yohan Dubois, and Justin I. Read. Cusp-core transformations in dwarf galaxies: observational predictions. *Monthly Notices of the Royal Astronomical Society*, 429(4):3068–3078, 01 2013. ISSN 0035-8711. doi: 10.1093/mnras/sts563. URL https://dx.doi.org/10.1093/mnras/sts563.

Teyssier, R. Cosmological hydrodynamics with adaptive mesh refinement - a new high resolution code called ramses. *A&A*, 385(1):337–364, 2002. doi: 10.1051/0004-6361:20011817. URL https://doi.org/10.1051/0004-6361:20011817.

O. Urban, A. Simionescu, N. Werner, S. W. Allen, S. Ehlert, I. Zhuravleva, R. G. Morris, A. C. Fabian, A. Mantz, P. E. J. Nulsen, J. S. Sanders, and Y. Takei. Azimuthally resolved x-ray spectroscopy to the edge of the perseus cluster. *Monthly Notices of the Royal Astronomical Society*, 437(4):3939–3961, 2014. doi: 10.1093/mnras/stt2209. URL http://dx.doi.org/10.1093/mnras/stt2209.

A. Vikhlinin, A. Kravtsov, W. Forman, C. Jones, M. Markevitch, S. S. Murray, and L. Van Speybroeck. Chandra sample of nearby relaxed galaxy clusters: Mass, gas fraction, and mass-temperature relation. *The Astrophysical Journal*, 640(2):691, 2006. URL http://stacks.iop.org/0004-637X/640/i=2/a=691.

Xiao-Feng Wang. *fANCOVA: Nonparametric Analysis of Covariance*, 2010. URL https://CRAN.R-project.org/package=fANCOVA. R package version 0.5-1.

Andrew R. Wetzel, Philip F. Hopkins, Ji hoon Kim, Claude-André Faucher-Giguère, Dušan Kereš, and Eliot Quataert. Reconciling dwarf galaxies with Λcdm cosmology: Simulating a realistic population of satellites around a milky way-mass galaxy. *The Astrophysical Journal*,

827(2):L23, 08 2016. doi: 10.3847/2041-8205/827/2/l23. URL https://doi.org/10.3847%2F2041-8205%2F827%2F2%2Fl23.

Coral Wheeler, Philip F. Hopkins, Andrew B. Pace, Shea Garrison-Kimmel, Michael Boylan-Kolchin, Andrew Wetzel, James S. Bullock, Dusan Keres, Claude-Andre Faucher-Giguere, and Eliot Quataert. Be it therefore resolved: Cosmological Simulations of Dwarf Galaxies with Extreme Resolution. *arXiv e-prints*, art. arXiv:1812.02749, 12 2018.

Radosław Wojtak, Stefan Gottlöber, and Anatoly Klypin. Orbital anisotropy in cosmological haloes revisited. *Monthly Notices of the Royal Astronomical Society*, 434(2):1576–1585, 2013. doi: 10.1093/mnras/stt1113. URL http://dx.doi.org/10.1093/mnras/stt1113.

Jesús Zavala, Mark Vogelsberger, and Matthew G. Walker. Constraining self-interacting dark matter with the milky way's dwarf spheroidals. *Monthly Notices of the Royal Astronomical Society: Letters*, 431(1):L20–L24, 2013. doi: 10.1093/mnrasl/sls053. URL http://dx.doi.org/10.1093/mnrasl/sls053.

F. Zwicky. Die Rotverschiebung von extragalaktischen Nebeln. *Helvetica Physica Acta*, 6: 110–127, January 1933.

3 Cosmological tension from weak-lensing measurements

On the mass mismatch between simulations and weak-lensing measurements

Astronomy & Astrophysics, (under review)

Jacob Svensmark[1], **Davide Martizzi**[1,2], **Adriano Agnello**[1]

[1] Dark Cosmology Centre, Niels Bohr Institute, University of Copenhagen, Jagtvej 128, 2200 Copenhagen.

[2] Department of Astronomy and Astrophysics, University of California, Santa Cruz, CA 95064, USA

Abstract

Context. The recently discovered discrepancy between galaxy mass measurements from weak lensing and predictions from abundance matching questions our understanding of cosmology, or of the galaxy-halo connection, or of both.

Aims. We re-examine this tension by considering, as models, different cosmological simulations in the Illustris suite.

Methods. We produced *excess profiles* $R\Delta\Sigma$ from subhalo snapshots at different redshifts in Illustris-1 and IllustrisTNG (TNG100, TNG300) simulations, enabling a direct comparison with weak-lensing measurements. We separate the individual contributions of stars, dark matter and gas within ≈ 1 Mpc (comoving length), beyond which correlated two-halo terms dominate.

Results. The mismatch between measurements and predictions depends strongly on how massive and isolated galaxies are selected, and with the simulation resolution, up to factors of two. In contrast to abundance matching results, the $R\Delta\Sigma$ profile may either increase, decrease or stay constant with redshift. This depends on how the mock sample are corrected to match observational incompleteness, which in turn depends on simulation resolution. The contribution of gas to $R\Delta\Sigma$ is $5-10\%$ over the scales dominated by one-halo terms.

Conclusions. Different procedures to link stellar and halo masses (abundance matching, cosmological simulations) are still significantly discrepant with one another. Therefore, the change in cosmological parameters advocated through abundance-matching arguments may not resolve this tension. Also, current criteria to select isolated massive galaxies in simulations are susceptible to resolution issues and may not correspond to observational criteria. The (currently subdominant) contribution of gas is non-negligible, and even if the major discrepancy within stellar and halo masses is resolved, it will be an appreciable source of systematics in the LSST era, when uncertainties on the $R\Delta\Sigma$ profiles are expected to be ≈ 10 times smaller.

3.1 Summary

The following summary sets the frame for a recent claim, that deviations from ΛCDM predictions in weak gravitational lensing measurements may be reconciled by introducing "new physics" i.e. new values for cosmological parameters. We calculate similar predictions from the state of the art series of "Illustris-TNG" cosmological simulations. Illustris-TNG are cosmological high-resolution simulations that include comprehensive baryonic physics. We show, that our predicted lensing signal suffers from lack of simulation convergence. If this is true for the Illustris TNG simulation suite, then it is likely also true for the simulations used in the recent study suggesting "new physics". We therefore state, that stronger simulation convergence needs to be achieved before cosmological inference can be made from the weak lensing measurements.

The notion that gravity affects light in the same way that it affects matter can be traced as far back as to Newton. He asked in the appendix of his 1704 book on optics, whether "Bodies act upon Light at a distance, and by their action bend its Rays <...> ? [Newton, 1704]". It would however be more than 200 years until Einstein formulated his theory of general relativity, that gravity effects on light followed naturally from theory: Light follows the the space-time curvature that the presence of matter-energy imposes. The light deflection of stars around the sun was later observed during a solar eclipse in 1919, and with that the seed was planted for what was to become the powerful astrophysical and cosmological probe that is gravitational lensing.

A logical place to search for gravitational effects is in the context of something with a lot of mass. In his famous paper from 1937, Fritz Zwicky pointed out that galaxy clusters, the most massive self gravitating systems in our universe, could act as convex optical lenses for light sources located behind them [Zwicky, 1937]. This was first observed in the 1970's for a lensing galaxy group that produced two images of the same background source [Walsh et al., 1979]. Multiple images of background sources, arcs of background light smeared around the lens and obvious distortion of the optical field are effects that are currently referred to as strong gravitational lensing. The heavier the lens, the more strongly it affects the background source image, and for this reason strong lensing may be used to determine the mass in the large end of the halo mass function. Strong gravitational lensing is challenged by the fact that light is affected by the mass distributed along the entire line of sight, not just the lens. Complex modelling of strong-lensing systems may account for this if multiple lenses at various redshifts can be observed, but in general this is an intrinsic issue for lensing as a mass estimator.

Gravitational lensing effects have a wide array of applications, and strong lensing phenomena are extensively used for measuring object masses and magnifying highly distant objects. As an example of the powerful applications of strong gravitational lensing, time delay cosmography can be mentioned: It can be shown that the time-delay between events in multiple images of the same lensed source provides a distance measure, which can be used to infer estimates of cosmological parameters (see e.g. Treu and Marshall [2016] for a review). At present, measurements from cosmographic timedelay distances put the Hubble constant H_0 measurements

in a 5.3 σ tension with the one inferred from the cosmic microwave background Wong et al. [2020], questioning the validity of the standard ΛCDM model.

The ΛCDM model of the universe is consistent with a flat space-time on cosmological scales. However on smaller scales, the perturbations i.e. large scale structure of the matter-field influences the path of propagating radiation. Consequently, our astronomical observations are subject to the distorting effect of the large scale structure thus shearing the visual field. This effect is on the order of a percent, and hence the study of cosmic shear γ is referred to as a weak gravitational lensing effect.

For galaxy - galaxy lensing, that is, lensing of background galaxies due to a foreground galaxy lens, the average image shear around the lens can be measured (see Kilbinger [2015] and Bartelmann and Maturi [2017] for reviews, or e.g. Leauthaud et al. [2012] and Mandelbaum et al. [2013] for summaries and applications). Because there is a central lensing object, it is expected that background galaxies are distorted tangentially to the line from the lens center and to each lensed background galaxy. By measuring the ellipticity of lensed background galaxies one obtains a measure of γ around a galaxy. The tangential shear probes the mass overdensity that makes up the lens galaxy, and by averaging azimuthally the magnitude of the tangential distortion, a tangential shear profile γ_t can be obtained. With complementary redshift information on the lens and lensed galaxies, the critical surface density can be calculated as

$$\Sigma_{crit} = \frac{c^2}{4\pi G}\frac{D_{OS}}{D_{OL}D_{LS}},$$

where c is the light speed, G the gravitational constant, D are angular diameter distances between observer and source (OS), observer and lens (OL) and lens and source (LS). The surface mass density contrast $\Delta\Sigma$ is then

$$\Delta\Sigma(R) \equiv \overline{\Sigma}(< R) - \overline{\Sigma}(R) = \gamma_t \Sigma_{\rm crit}$$

Here, $\overline{\Sigma}(< R)$ is the average surface density within projected radius R, and $\overline{\Sigma}(R)$ is the azimuthally averaged surface density at R. The galaxy - galaxy lensing effect amounts to a distortion at the percent level, and thus the S/N ratio is very low for any given galaxy. Thus measuring $\Delta\Sigma(R)$ becomes a statistical exercise, and requires large surveys for bringing down error bars. The $\Delta\Sigma$ profile is cosmology dependent, and can be related to the matter density of the Universe Ω_m and the density fluctuation amplitude at 8 Mpc scales σ_8. The $\Delta\Sigma$ signal can then be measured and readily compared to $\Delta\Sigma$ predictions from cosmological N-body simulations of any given cosmology.

In Leauthaud et al. [2017] the $\Delta\Sigma$ signal is measured between redshift $0.43 > z > 0.7$. They analyse the high-redshift "CMASS" sample of galaxies from the BOSS spectroscopic survey as weak gravitational lenses [Dawson et al., 2013]. For galaxies in the CMASS sample, observations from the Canada-France-Hawaii Telescopes "Lensing Survay" and "Stripe 82 Survey" are used to calculate the actual average $\Delta\Sigma$ profile. These are then compared to numerical predictions from simulations, whose mock galaxy samples have been adjusted to mimic the incompleteness of the CMASS sample. They find that the simulations overpredict the amplitude of the $\Delta\Sigma$ signal by 20-40%. They go on to suggest that this could be reconciled

by lowering the value of the $S_8 = \sigma_8\sqrt{\Omega_m/3}$, in other words suggesting that our best fit cosmological model might need to be reworked.

In the article below, our objective was to reproduce the overprediction of the $\Delta\Sigma$ signal that Leauthaud et al. observe, using state-of-the-art numerical simulations. We produce mock galaxy catalogues from the Illustris-TNG simulation suite, which are magneto-hydrodynamical N-body simulations of box sizes up to 300^3 Mpc, with comprehensive baryonic physics modelling and high particle resolution. This provides a more direct $\Delta\Sigma$ prediction than the simulations of Leauthaud et al., as they rely on stellar to halo abundance matching, which assumes that there exists a monotonic mapping between dark matter halo mass and stellar galactic mass. We find that while Illustris significantly overpredicts the lensing signal, the magnitude of the over prediction is strongly dependent of the numerical resolution of the simulation. If lack of numerical convergence affects the $\Delta\Sigma$ signal in the Illustris TNG simulation suite, then it certainly also affects the simulations of Leauthaud et al., since their numerical resolution is significantly lower. Thus the predictions of Leauthaud et al., or worse, numerical simulations in general, may have to be improved significantly before the CMASS weak galaxy - galaxy lensing signal can be considered competitive for cosmological inference. This could be simply in terms of numerical resolution i.e. computation power, or combined with improvements in the baryonic physics modelling.

3.2 Introduction

Our understanding of cosmology is tied to that of the galaxy-halo connection. Departures from concordance cosmology, if any, should occur at scales $\lesssim 2$ Mpc, where however the mass budget and density profiles are also influenced by baryonic physics [e.g. Parimbelli et al., 2019, Hildebrandt et al., 2020]. Recent measurements from weak galaxy-galaxy lensing (GGL, from Leauthaud et al. 2017, hereafter L17) resulted in lensing profiles that cannot be reconciled with abundance-matching predictions based on clustering measurements [Saito et al., 2016, Rodriguez-Torres et al., 2016], with a statistically significant mismatch. This mismatch has been confirmed independently and is seemingly robust against modelling and inference on the weak-lensing signal [Sonnenfeld et al., 2019] and against different procedures to construct stellar-to-halo relations [Rodriguez-Torres et al., 2016, Behroozi et al., 2019]. This would then question our general understanding of cosmology or of galaxy formation, or both.

Here, we use different simulations from the Illustris suite to compare the GGL profiles of massive galaxies to the measured profiles of L17. We consider different redshift slices and multiple criteria to select isolated massive galaxies, including those by L17. We correct our predictions based on incompleteness estimates from two sources [Saito et al., 2016, Rodriguez-Torres et al., 2016]. We find that the mismatch has a different behaviour with redshift depending on which abundance-matching based incompleteness estimate we use, and that galaxies satisfying the isolation criteria of L17 may actually not be isolated. We also find that such criteria are based on properties of simulated galaxies that are not entirely converged as a function of numerical resolution, which causes the GGL signal inferred from the selected galaxies to vary significantly from simulation to simulation. Different criteria to select massive and isolated galaxies can mitigate the mismatch or artificially inflate it.

This paper is organised as follows: in Section 2 we recall the simulation suites used in this work and their main properties; the construction of weak-lensing profiles is described in Section 3; results are given in Section 4, and the implications are discussed in Section 5. For ease of comparison with the findings of L17, throughout this paper we use comoving distances to compute the weak-lensing mass profiles.

3.3 Data

The Illustris project [Vogelsberger et al., 2014], and its TNG incarnation [Weinberger et al., 2017, Pillepich et al., 2018b,a, Springel et al., 2018, Nelson et al., 2018, Naiman et al., 2018, Marinacci et al., 2018], comprise a suite of cosmological Λ-CDM simulations with N-body treatment of dark matter dynamics, magneto-hydrodynamical treatment of baryon dynamics, radiative cooling, star formation, stellar and active galactic nuclei feedback. The TNG project constitutes a significant update of the physical models implemented in the original Illustris suite. The simulation data from the original Illustris project and TNG are now publicly available [Nelson et al., 2015, 2019]. A halo catalogue, built through a friends-of-friends (FoF)

Table 3.1: Overview of the available simulations of the Illustris [Vogelsberger et al., 2014] and IllustrisTNG suite [Pillepich et al., 2018b] used in this work, through the publicly released catalogs and snapshot data [see Nelson et al., 2015, for a release description]. $M_{\rm bar}$ shows the baryonic particle mass, $M_{\rm dm}$ the dark matter particle mass, $L_{\rm box}$ the box side length and $N_{\rm dm}$ the number of dark matter particles in the box. Rows $N_{a<z<b}$ show the number of subhalos with properties as discussed in the main text that resides within each redshift range $a < z < b$. Note that this number is distributed onto multiple snapshots. The number of snapshots within each redshift range is indicated in the second column.

		TNG300			TNG100			Illustris-1
		1	2	3	1	2	3	1
$M_{\rm bar}$	$[10^6\,{\rm M}_\odot]$	11	88	703	1.4	11.2	89.2	1.3
$M_{\rm dm}$	$[10^6\,{\rm M}_\odot]$	59	470	3760	7.5	59.7	478	6.3
$L_{\rm box}$	[cMpc]	302.6	302.6	302.6	110.7	110.7	110.7	106.5
$N_{\rm dm}$		2500^3	1250^3	625^3	1820^3	910^3	455^3	1820^3
$N_{0.4<z<0.5}$	4 snapshots	7136	3995	1913	610	363	202	778
$N_{0.5<z<0.6}$	5 snapshots	8228	4498	2142	737	424	240	1019
$N_{0.6<z<0.7}$	3 snapshots	4556	2429	1142	404	230	128	629

algorithm, is available for each snapshot of each simulation, with a corresponding subhalo catalogue within each halo generated using the `subfind` algorithm [Springel et al., 2005].

`subfind` computes an adaptively smoothed dark matter density field and then uses a density threshold to identify subhalo candidates. Each subhalo candidate is subjected to a gravitational unbinding procedure in which only bound structures with more than 20 particles are identified as real gravitationally bound subhalos. For each subhalo a list of properties, including its stellar mass, is computed on-the-fly.

Since star formation from gas in subhalos is simulated explicitly in the Illustris and IllustrisTNG suites, the stellar mass in each subhalo is a direct prediction of the simulations. However, it should be kept in mind that the parameters of the sub-resolution models for galactic feedback, which strongly influence the star formation history, have been calibrated in such a way that the predicted stellar mass function is consistent with the observed one at redshift $z = 0$ [Pillepich et al., 2018b]. This calibration is only approximate and is not based on mock observations of the simulated galaxies that would allow to measure stellar masses that are directly compared to observational determinations. For this reason, the subhalo mass vs. stellar mass relationship should be considered as a prediction of the simulations.

In this paper, the subhalo mass vs. stellar mass relation is obtained using the subhalo mass computed by `subfind` with the procedure described above, which corresponds to the total gravitationally bound mass in each system. Pillepich et al. (2018a) considered only the stellar mass in bound particles within 30 kpc of each halo. This may be a problem for the most massive galaxies, and in general it could introduce spurious truncations due to the finite resolution of the simulations. Therefore, here we fit a superposition of two Sersic profiles to the surface brightness of each object, obtained by viewing it along three random directions. The double-Sersic fit was performed for each viewing direction separately, and the total stellar mass can be obtained analytically. Figure 3.3 shows a comparison of the double-Sersic stellar mass (with 68% confidence ranges) versus the particle mass given by `subfind`. The agreement is within better than 2% for most objects. In the following, we use

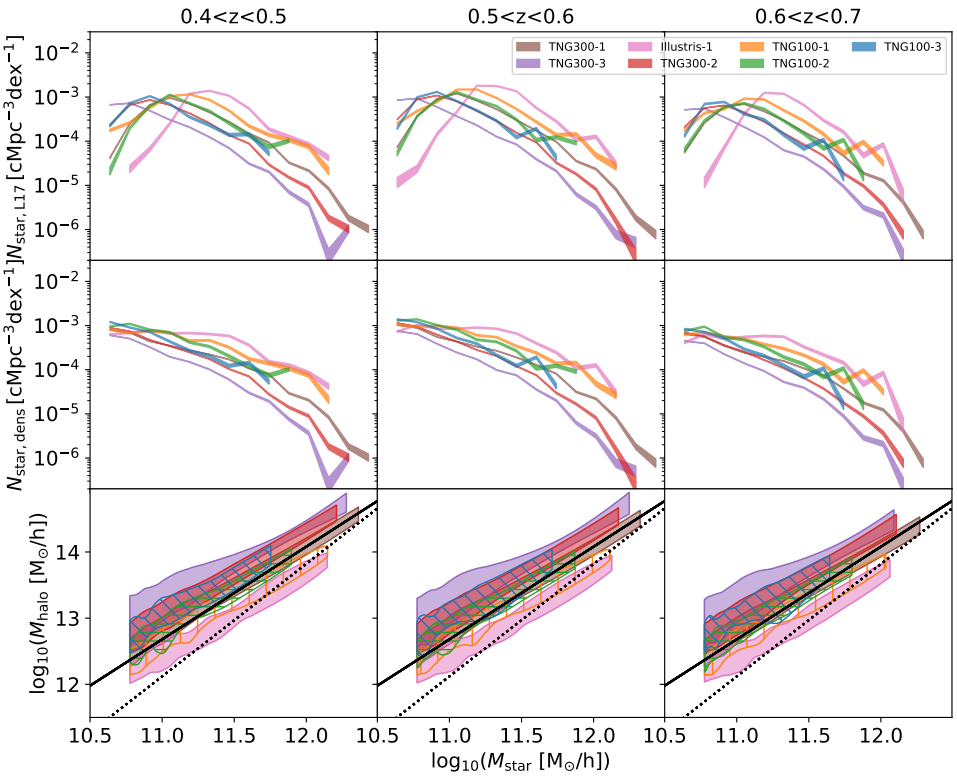

Figure 3.1: Stellar mass functions (top and middle row) and stellar-to-halo mass relations (bottom row) from different Illustris-1/-TNG simulations. The stellar mass functions changes significantly between simulations with different resolution, but (except for the poorest-resolution versions) they all agree around $M_\star \approx 1.1 \times 10^{11} M_\odot$, i.e. only at the lower limit of our weak-lensing selection. By comparison, the solid (resp. dotted) black line results from population models of strong (resp. weak) lensing data [Sonnenfeld et al., 2018, 2019].

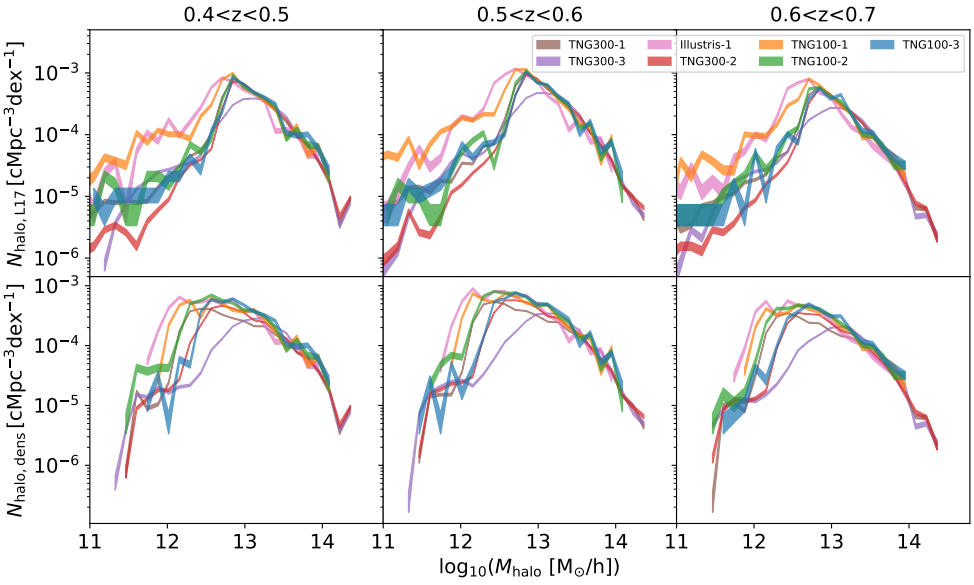

Figure 3.2: Halo mass functions from different Illustris-1/-TNG simulations, binned in the same redshift ranges as before for the L17 v_{max} cut (top row) and for the 3D density cut (bottom row).

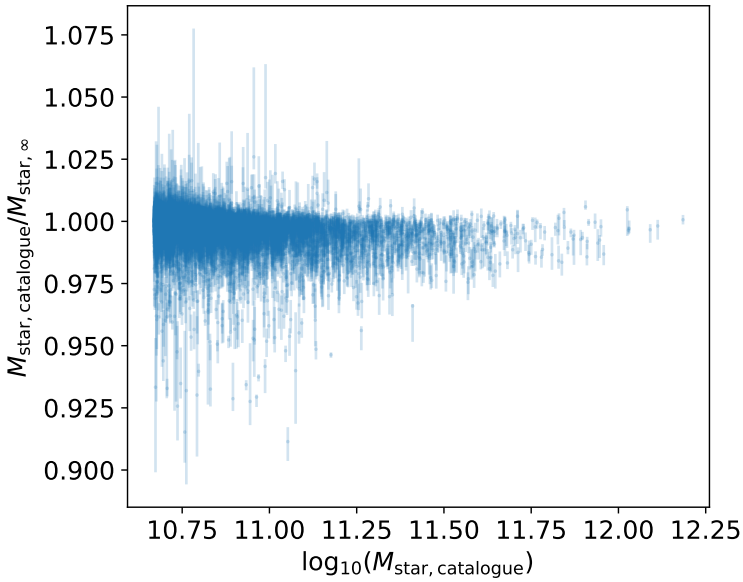

Figure 3.3: Comparison of the catalogue stellar mass $M_{\mathrm{star,catalogue}}$ and fitted double Sersic mass $M_{\mathrm{star},\infty}$ and 68% confidence bands of all subhalos in snapshot 60 of TNG300-2, for v_{max} criteria.

the double-Sersic stellar masses. The double-Sersic fits and their uncertainties also give us a meaningful way of addressing Eddington bias in selecting massive galaxies.

The main properties of each simulation analysed in this work are summarized in Table 1. The public release provides simulation data for two box sizes of volume $110.7\,\mathrm{Mpc}^3$ and $302.6\,\mathrm{Mpc}^3$, which have been named TNG100 and TNG300, respectively. Each of the above has been run at three different resolution choices, both including and excluding the baryonic component. Given the box sizes and the abundance of massive galaxies, these are also the most suited to our study.

3.4 The surface mass density contrast profile

The analyses by L17 and Saito et al. (2016) proceed by selecting galaxies with $M_\star > 10^{11} M_\odot$, in isolation. Here, we revisit the L17 criteria, introduce different criteria, and build weak-lensing profiles.

3.4.1 Selecting isolated and massive galaxies

Different criteria can be devised to select isolated and massive galaxies. L17 imposed lower cut-offs on catalog stellar masses $M_\star > 10^{11}\,M_\odot$ and peak circular velocities $V_{\mathrm{max}} \geq 351\,\mathrm{km/s}$. However, there are two main issues with this approach: first, one rarely has observational data on V_{max} in observations; second, this results in a low density over very large volumes,

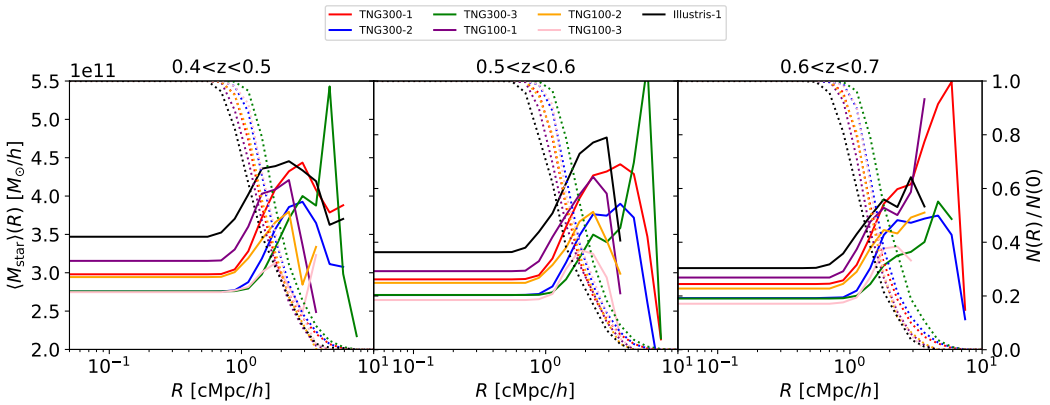

Figure 3.4: The contribution of acceptable subhalos to the GGL analysis in different Illustris-1/-TNG simulation boxes, in three redshift ranges corresponding to the same adopted by L17. The dotted lines indicate the fraction of subhalos with non-zero $R\Delta\Sigma$ signal at different radii. The full lines show the average stellar mass $\langle M_\star \rangle(R)$ contributed by accepted subhalos at different locations.

and a further cutoff on halo mass, but not (necessarily) on the line-of-sight proximity to other galaxies.

For this reason, we also examine two variations, where we discard any cutoff on $V_{\rm max}$. In the *2D* criterion, we require that the stellar mass of the lensing galaxy is higher than any other stellar mass of halos within projected 2 cMpc. In the *3D* criterion, we instead select galaxies based on the density of objects within spheres of 8 cMpc. In particular, we select only galaxies in the lower 10% quantile of the density distribution ($n \lesssim 10^{-3}/\mathrm{cMpc}^3$). A ≈ 10 cMpc sphere radius selection sample does not change the densities appreciably. The 3D criterion suffers from the issue that since the number density of `subfind` halos is higher surrounding more massive galaxies, taking the 10% quantile systematically suppresses the high mass end of the stellar mass function. For this reason, we will not consider a sample cut using the *3D criterion* by itself, but rather require that galaxies meet either the condition of the *2D* criterion or the *3D* criterion in what we will refer to as the *2D or 3D* criterion.

The top panels of Figure 3.1 show the stellar mass function of the velocity-selected subhalos in three redshift bins, $0.4 < z < 0.5$, $0.5 < z < 0.6$, and $0.6 < z < 0.7$, respectively, selected with the *L17* criterion. The stripes indicate the number of halos $N \pm \sqrt{N}$ within each bin in $M_{\rm star}$ assuming a Poisson distribution. The number density of galaxies with $M_\star \approx 10^{11}\,M_\odot$ is comparable across all simulations, and in multiple redshift bins, independently on box size and resolution. Slight but appreciable differences can be seen at lower stellar masses when resolution and box size are varied. The differences become significant, especially at higher stellar masses. This indicates that the simulations do not entirely converge for galaxies selected using the *L17* criteria, and that the effects of cosmic variance may also play a role in setting the observed differences. Nonetheless, simulations with similar resolution (TNG300-1 and TNG100-2) yield comparable galaxy stellar mass functions for our selection.

The middle panels show the stellar mass function (SMF) for the *2D-or-3D* criterion. The SMF at $> 10^{11}\,M_{\odot}$ is comparable to the *L17* criterion stellar mass function in the top row. However, the SMF do not show any sign of converging with increasing resolution.

The bottom panels of Figure 3.1 show the relation between stellar mass and total subhalo mass for the *2D-or-3D* criterion. A *Locally Estimated Scatterplot Smoothing* (LOESS) curve with variability bands was calculated for each simulation in the shown redshift bins, using a smoothing parameter of 0.35 [Scrucca, 2011, Weisberg, 2005]. The plots show that, with increasing resolution, the TNG100 and TNG300 converge to similar relations. On the other hand, the original Illustris-1 simulation is systematically offset with respect to TNG100-1 and TNG300-1: for a fixed subhalo mass, Illustris-1 typically yields larger stellar masses than the TNG simulations. In Fig. 3.2, the halo mass function is presented for the *L17* isolation criteria in the top row, and the 3D criteria in the bottom row.

We note that the *integrated* densities of objects, following cuts in $v_{\rm max}$ (chosen by L17 as an isolation criterion), are the same across different simulations with comparable resolution, as reported in Table 1. However, there are two main issues with this choice. First, isolation criteria should be based on local densities of objects around given subhalos, which is not necessarily the case here. Second, a criterion based on $v_{\rm max}$ is susceptible to resolution in the simulations, and so may not even be a robust indicator of integrated density. Here, we have chosen to examine the isolation criteria by L17 mainly for ease of comparison with their results, based on $z \approx 0.5$ snapshots from Illustris-1.

3.4.2 Computing weak-lensing profiles

For each subhalo within the selected range, the snapshot data of particles within its parent halo were extracted. For each of the projections along the three Cartesian axes, the surface mass density $\Sigma(R)$ was calculated in logarithmically spaced radial bins, as well as the average surface density $\Sigma(< R)$ within circles of corresponding radii. From this, the surface mass density contrast profile of the ith galaxy is directly

$$\Delta\Sigma_i = \Sigma_i(R) - \Sigma_i(< R) \tag{3.1}$$

which is the observable extracted from weak GGL measurements. This procedure was repeated for each accepted subhalo and for different species of particles (stellar, dark matter, gas, black holes)[1]. The final $\Delta\Sigma$ profile can then be averaged directly. However upon comparison with the measured GGL profiles of L17, the incompleteness of their sample should be taken into account. Both Leauthaud et al. [2016] and Rodriguez-Torres et al. [2016] produce stellar mass functions $\Phi(M)$ at multiple redshifts, in which they model the incompleteness of the galaxy sample on which the GGL signal is based. Both models are based on abundance-matching, and the Leauthaud et al. [2016] stellar mass functions are based on the Saito et al. [2016] model that is overpredicting the GGL signal in L17. We reweight our $\Delta\Sigma$ profiles based on stellar mass functions from Leauthaud et al. [2016] or Rodriguez-Torres et al. [2016]

[1]Tables of profiles for selected snapshots of all selected subhalos are publicly available upon request

relative to the uncorrected stellar mass functions of the Illustris simulations. The averaged and incompleteness weighted GGL profile is then

$$\Delta\Sigma = \frac{\sum_i \left(\Phi_{\rm inc}(M_{\star,i})/\Phi_{\rm sim}(M_{\star,i})\right) \Delta\Sigma_i}{\sum_i \left(\Phi_{\rm inc}(M_{\star,i})/\Phi_{\rm sim}(M_{\star,i})\right)}, \tag{3.2}$$

Here $M_{\star,i}$ is the stellar mass of the i'th halo, $\Phi_{\rm inc}$ is the incomplete stellar mass function of either Leauthaud et al. [2016] or Rodriguez-Torres et al. [2016], and $\Phi_{\rm sim}$ is the SMF of the Illustris simulation considered. By doing so, we are able to incorporate incompleteness in our GGL signal predictions. We repeated this procedure for each of the L17, *2D*, and *2D-or-3D* criteria. The number of acceptable subhalos for each simulation box, in three redshift ranges, is summarized in Table 3.1 for the *L17* criterion.

Quite expectedly, subhalos of different mass contribute to the GGL signal in different radial ranges. For this reason, we also recorded the fraction and average stellar mass of contributing subhalos in each radial bin. This is shown in figure 3.4, for different Illustris-1/-TNG simulations and in three redshift ranges matching the measurements of L17. The subhalo contributions are robust within $R \lesssim 0.7$ Mpc. This is also comparable to the radius beyond which also correlated two-halo terms would start to dominate. The average stellar mass of contributing subhalos at $R \lesssim 1$ Mpc is uniform with radius, but it changes across simulations as a result of the differing stellar-mass functions (shown in Fig. 1).

A possible source of concern would be the relation between shear, which is closer to what is actually measured in observations, and the $R\Delta\Sigma$ profiles. However, our criteria for isolation and the stacking over many subhalos ensures that the $R\Delta\Sigma$ is robustly determined, and a full ray-tracing simulation is not necessary. This is reinforced by the fact that our $R\Delta\Sigma$ profiles from Illustris-1 at $z \approx 0.5$, following the L17 criterion, are the same as obtained[2] by L17.

3.5 Results

From the subhalo tables generated in the previous section and for each particle type (dark matter, stars, gas and black holes), the excess profiles were averaged within 3 redshift ranges: $[0.4 < z < 0.5]$, $[0.5 < z < 0.6]$, and $[0.6 < z < 0.7]$. This was done for the sake of direct comparison with the measured GGL profiles by L17. The stacked profiles are shown in Fig. 3.5, and the L17 GGL measurements are displayed with black error-bars. The top row displays the profile for each of the four particle types as well as the total, for the TNG300-1 simulation. Note, that contrary to the rest of the rows, the profiles of this row were not adjusted for incompleteness.

The second row of Fig. 3.5 shows only the total excess profile, but for all of the simulations considered in this work. These profiles have been corrected for incompleteness using the stellar mass functions of Leauthaud et al. [2016] based on the Saito et al. [2016] abundance-matching simulation. A slight decrease in the excess profiles with increasing redshift can

[2] In that work, only $z \approx 0.5$ profiles from Illustris-1 were examined.

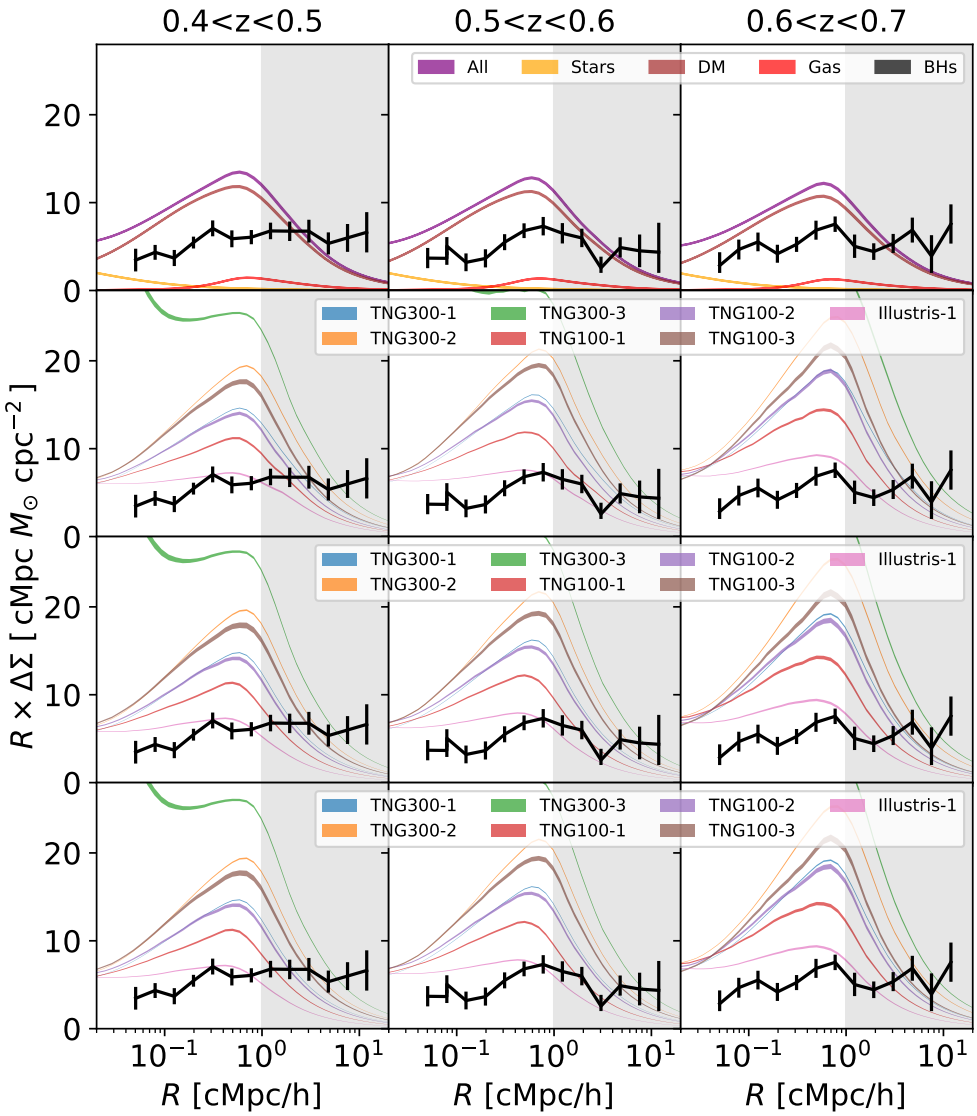

Figure 3.5: The GGL contrast profile $R\Delta\Sigma$ in three redshift ranges. For each panel, the CMASS GGL profile measured by L17 is shown as the black curve with error bars. *First row:* $R\Delta\Sigma$ from the TNG300-1 simulation using the $V_{\rm max}$ isolation criteria, split into the four particle species (stars, dark matter, gas, black holes). Note that the black hole contribution is nearly zero and hardly visible in the figure. *Second row:* Profiles from different Illustris-1/-TNG box sizes and resolutions again isolated via $V_{\rm max}$. In all panels, the width of the line is the standard deviation of $R\Delta\Sigma$ across acceptable subhalos. *Third row:* $R\Delta\Sigma$ profiles from galaxies that meet the 2D isolation criteria, reweighted based on L16 modelled CMASS incompleteness. *Fourth row:* $R\Delta\Sigma$ profiles from galaxies that meet *either* the 2D *or* the 3D isolation criteria, reweighted based on L16 modelled CMASS incompleteness SMF Leauthaud et al. [2016]. All length measures are in co-moving coordinates, as in L17.

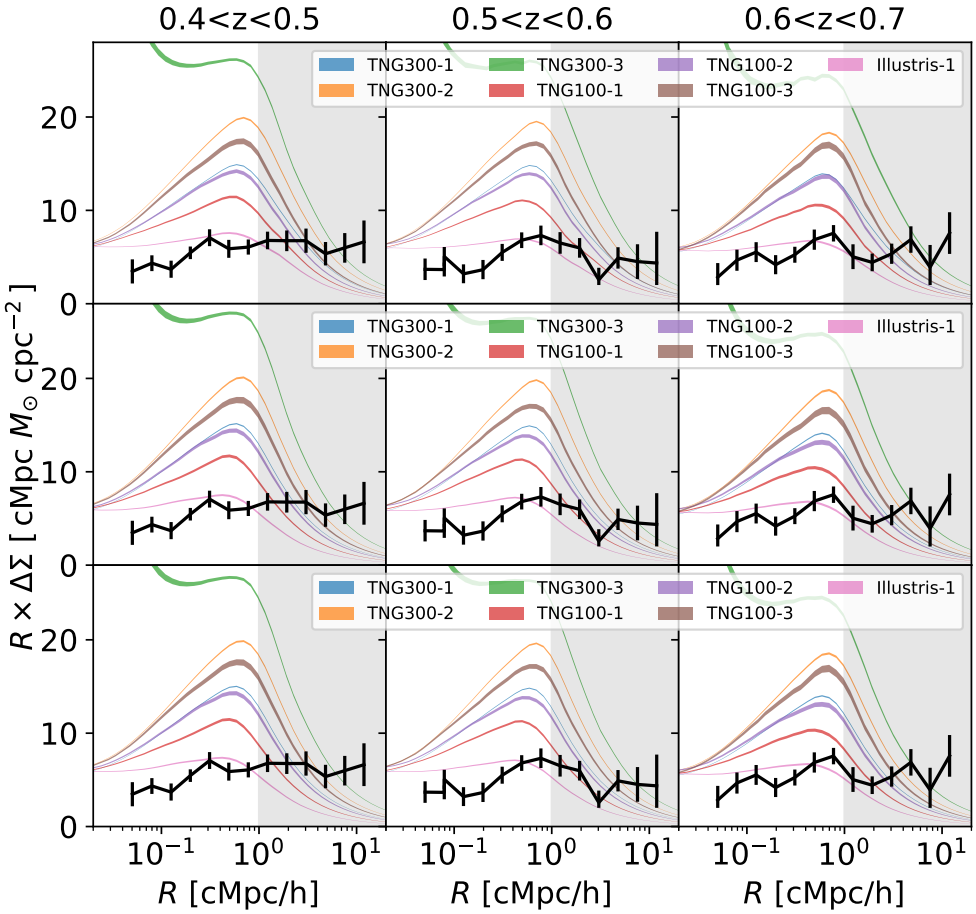

Figure 3.6: The GGL contrast profile $R\Delta\Sigma$ in three redshift ranges. These three rows are identical to row 2, 3 and 4 of Figure 3.5, with the one exception that the SMFs used for reweighting are those based on the model from Rodriguez-Torres et al. [2016], and not those from Leauthaud et al. [2016]. We note that the profiles tend to decrease, rather than increase, for this incompleteness correction.

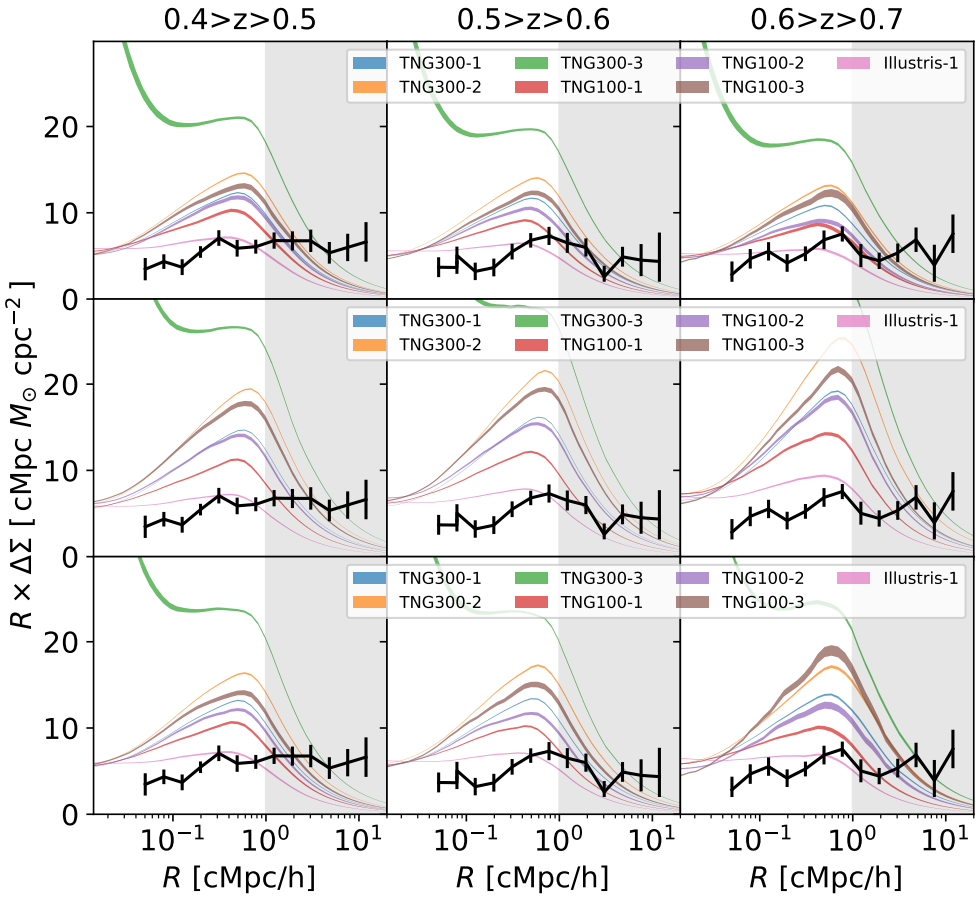

Figure 3.7: The GGL contrast profile $R\Delta\Sigma$ in three redshift ranges. All rows show profiles from the set of galaxies that fulfill the *2D or 3D* criterion. In the top row, an Eddington mass bias was added to the catalogue stellar mass before the population was cut at 10^{11} M$_\odot$. In the second row, for each of the galaxies, its contribution to the GLL profile is reweighted corresponding to the difference between the SMF of the simulation in question, and the SMF of CMASS for each redshift range. For the middle row, a MCMC fit of a double-sersic profile was performed to the stellar particles. Besides weight from the SMF adjustment, the GLL curves are re-weighted for each galaxy according to the fraction of MCMC steps with Sersic mass larger than 10^{11} M$_\odot$. The profiles of the bottom row combines the weights from the middle row with the Eddington-biased stellar masses of the top row.

be seen for all of the simulations. All simulation profiles except that of the older Illustris-1 significantly overestimate the GGL signal, with a clear spread depending on simulation resolution.

The redshift increase of the predicted GGL signal is found most clearly in the third row of Fig. 3.5, which is analogous to the second row, but with the more stringent *2D* isolation criterion on subhalos. These profiles have been weighted with the Saito et al. [2016] stellar mass profiles that include a modelled incompleteness. The mismatch with measured GGL profiles, as well as the growing trend with redshift, is now much more pronounced. The spread of the different resolutions is also very large.

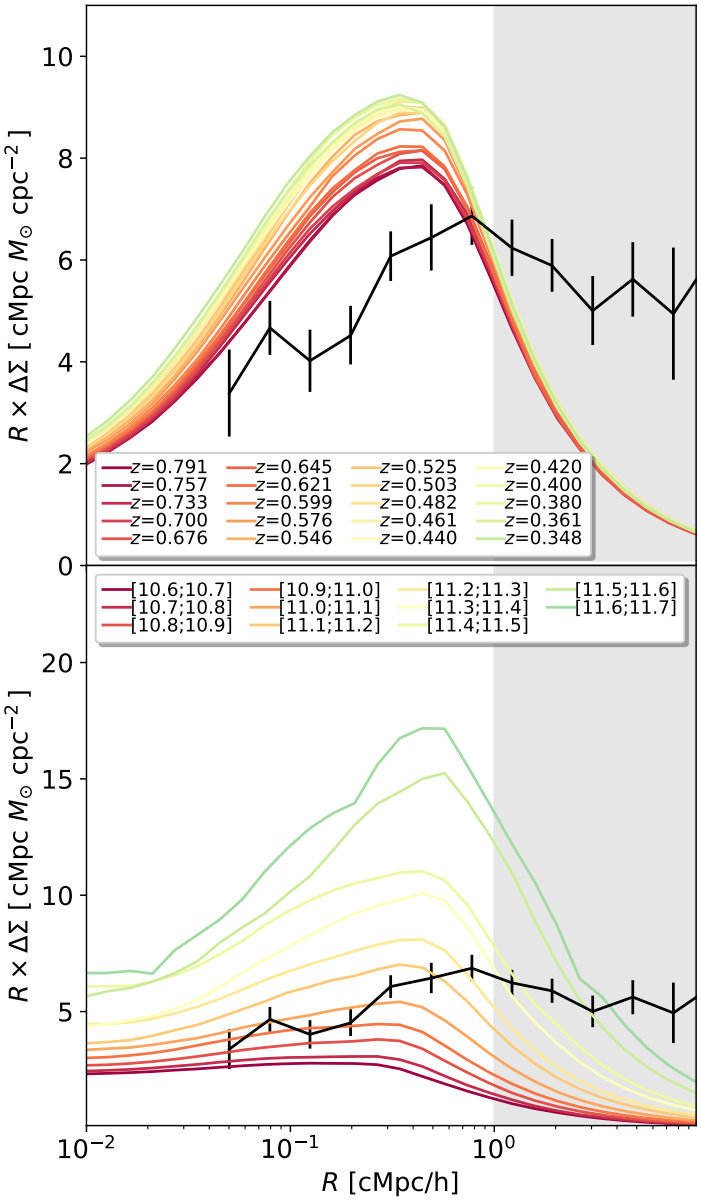

Figure 3.8: Top: Redshift evolution of the $R\Delta\Sigma$ profile for the TNG300-1 simulation, as represented by the coloured lines. The error-bars are the CMASS measurements as obtained from Leauthaud et al. [2017]. Bottom: The $R\Delta\Sigma$ profile for the TNG-300 simulation at redshift $z = 0.5$, split in stellar masses within the range indicated by the legend. The ranges are $\log_{10}(M_{star})$, where M_{star} is in $M_{\odot}/h$.

Finally, the fourth row of Fig. 3.5 shows the same as the third row, but for the *2D-or-3D* criterion. The profiles are very similar to the 2D criterion. We *did* test changing the ball radius between 6 cMpc and 10 cMpc, and the only appreciable change is in the smoothness of the density histograms. The discrepancy, spread and redshift evolution is still the same.

By using instead an incompleteness correction based on the Rodriguez-Torres et al. [2016] stellar mass functions for the *L17*, *2D* and the *2D-or-3D* criteria, the three rows of Fig. 3.6 are obtained. Now the redshift evolution of all profiles decreases slightly with redshift, contrary to the GGL profiles corrected based on Leauthaud et al. [2016] incompleteness estimates. The GGL profiles are less spread out compared to those in Fig. 3.5, but continue to be significantly spread out and overestimate the lensing signal.

As a further check, in order to mimic Eddington bias in observed samples, we also added a random offset to $\log_{10}(M_\star)$ (uniform within -0.1 and 0.1) before enforcing the stellar-mass cut and the *2D-or-3D* criterion, reweighted using Leauthaud et al. [2016] stellar mass functions. The effect of this Eddington bias on the Illustris GGL profiles can be seen in the top row of Figure 3.7. The Eddington bias reduces the Illustris profile overshoot somewhat, and reduces the spread slightly as well. In the middle row the fraction of points in each MCMC double-Sersic fits with a stellar mass above $10^{11}\,M_\odot$ is used as additional weight in the averaging of the individual contribution from galaxies to the GGL average. The bottom row combines the Eddington bias from the first row with the additional MCMC weight from the second row.

Fig. 3.8 shows the evolution the $R\Delta\Sigma$ excess profile of subhalos within the TNG300-1 simulation with redshift (top panel) and stellar mass (bottom panel). The redshift evolution is shown through 20 redshifts from the simulation snapshots between $z = 0.791$ and $z = 0.310$ for all the subhalo masses selected here. The mass evolution of the subhalos in the bottom figure is shown at $z = 0.503$ for 11 $M_{\rm star}$ bins as shown in the legend, between $1 \times 10^{11}\,M_\odot/h$ and $5 \times 10^{12}\,M_\odot/h$. The excess profile increases with increasing stellar mass, but more weakly than linearly. This trend, in the one-halo regime, can simply be interpreted as the result of $R_{\rm vir} \propto M_{\rm vir}^{1/3}$ and more massive halos being (slightly) less concentrated.

3.6 Discussion and Conclusions

In this paper, we measured the GGL signal predicted by the Illustris and IllustrisTNG (TNG100 and TNG300) suite of cosmological hydrodynamical simulations. We selected subhalos with stellar masses $M_\star > 10^{11}\,M_\odot$ and examined different criteria to ascertain isolation and incompleteness correction, to investigate their impact on the GGL signal. L17 found a mismatch between GGL measurements and model predictions, considering abundance-matching models based on clustering, as well as the then available Illustris-1 suite (only showed for $z \approx 0.5$ there). We confirm the existence of a similar mismatch over the wider suite of Illustris-TNG cosmological simulations, in different redshift ranges, for different isolation criteria. However, differently from the findings of L17 on Illustris-1, we find that for different incompleteness estimates the mismatch may either increase or decrease with redshift.

Most importantly however, we observe that simulation resolution significantly affects the amplitude of the predicted GGL signal. We furthermore find that the redshift evolution of the GGL signal may increase, decrease or remain constant, depending on the chosen incompleteness correction. The incompleteness modelling is based on the same abundance-matching models upon which the L17 predictions are based. In L17 it is pointed out that the main difference between the two abundance-matching models and incompleteness estimates is the resolution of the simulations that they are based on. The Illustris-TNG simulations have orders of magnitude better resolution and still yield resolution dependent GGL profiles, so we conclude that the incompleteness estimates and abundance matching predictions as a whole are not sufficiently converged to allow for direct comparison with the measured GGL signal.

We also find that the $v_{\rm max}$ criterion selects galaxies with the most massive halos (hence rarer) rather than galaxies in isolation. The mismatch is greatly reduced if the more physical direct criteria of isolation are used. In all cases, contrary to the L17 findings from clustering-based abundance matching, the mismatch does not necessarily increase with redshift, and can be negligible in the $0.6 < z < 0.7$ redshift bin. We should also emphasize that the CMASS galaxies, which are analysed by L17 and Saito et al. (2016), are not directly selected in terms of $v_{\rm max}$, as this quantity is not directly accessible in observations.

Given the statistical uncertainties on the profiles, the (mis)match is not only a byproduct of cosmic variance across different simulation boxes. Our tests also show that the uncertainties in determining stellar masses are not currently the dominant factor in possible mismatches between theory and observations.

One of possible sources of discrepancy between the GGL profiles measured from different simulations is the shape of the stellar mass function of the samples selected with our criteria. We find that the latter is influenced both by numerical resolution effects and by cosmic variance, if the $v_{\rm max}$ criterion is adopted. Applying a circular velocity cut allows one to construct galaxy samples with similar *integrated* number density in each simulation, but the samples have very different stellar mass functions. This issue is caused by the fact that stellar mass and circular velocity (i.e. the internal dynamics of dark matter halos) are properties that are not numerically converged at the resolutions reached by Illustris/IllustrisTNG. Differences in the stellar mass function yield differences in how massive galaxies are weighted against less massive galaxies when computing the stacked profiles, i.e. the GGL signal. Due to this effect, shallow tails at the high-mass end of stellar mass function produce a higher GGL signal. This spurious effect is much less evident, albeit still present (fig. 1), if the direct (2d, 2d-or-3D0 isolation criteria are chosen.

Another noteworthy effect is the GGL excess profile from gas particles. With the current mismatches and uncertainties, this $\approx 5 - 10\%$ contribution to the GGL signal is still negligible, but it may become a significant source of systematics if the mismatch is resolved. This will hold especially in the regime of the *Vera Rubin Observatory* LSST measurements, where (by a simple scaling of footprint) the uncertainties in measured GGL profiles are expected to shrink by a factor ≈ 10.

These findings have important implications if the role of cosmological parameters is examined. The mismatch between simulations and observations may be resolved if for a fixed stellar mass near the peak of the M_*/M_{total} ratio, the expected host halo mass were ~ 0.3 dex smaller than predicted by the IllustrisTNG simulations. Coincidentally, this is also the mismatch between strong-lensing and weak-lensing relations between stellar and halo masses [Sonnenfeld et al., 2018, 2019], which however is mostly due to the strong-lensing selection bias in deflector-selected samples and the analysis of different lens samples [Sonnenfeld et al., 2019] . Across different simulation suites, we note that a general agreement of high-resolution Illustris GGL profiles with the measured signal is found in Eagle simulations [Velliscig et al., 2017], albeit with large uncertainties due to the further slicing in stellar mass.

As a possible alternative to the mismatch with models based on abundance matching by Saito et al. [2016], L17 advocated for a lower value of the clustering amplitude $S_8 \propto \sigma_8\sqrt{\Omega_m}$ with respect to *Planck* measurements [see Planck Collaboration et al., 2018, and refernces therein]. Similar claims had also been made in the past, considering the pairwise-velocity dispersions of galaxies and their clustering strength [Yang et al., 2003, Li et al., 2009]. In fact, also the clustering of galaxies in IllustrisTNG [Springel et al., 2018] is admittedly higher than current observational results. However, as shown by L17, a smaller value of S_8 would make the GGL mismatch decrease further with increasing redshift, and (depending on sample selection and the resolution of simulations) this may actually exacerbate the mismatch between measurements and profiles from the IllustrisTNG simulations. Moreover, the model GGL profiles examined in this work span length-scales where two-halo terms are negligible, so the discrepancy found by L17 may be linked more fundamentally to uncertainties in stellar masses and the construction of abundance-matching relations, rather than to the relation between clustering and cosmological parameters. Therefore, these findings show that abundance matching recipes are significantly affected by the cosmological simulations that are used, and that using DM-only simulations (as done e.g. by Saito et al. 2016 or Rodriguez-Torres et al. 2016) can significantly bias the stellar-to-halo mass relations.

3.7 Acknowledgements

JS is funded by the Danish council for independent research under the project “Fundamentals of Dark Matter Structures”, DFF - 6108-00470. AA was supported by a grant from VILLUM FONDEN (project number 16599). DM acknowledges support by the Danish National Research Foundation (DNRF132).

Bibliography

Matthias Bartelmann and Matteo Maturi. Weak gravitational lensing. *Scholarpedia*, 12(1): 32440, January 2017. doi: 10.4249/scholarpedia.32440.

Peter Behroozi, Risa H. Wechsler, Andrew P. Hearin, and Charlie Conroy. UNIVERSEMACHINE: The correlation between galaxy growth and dark matter halo assembly from z = 0-10. *Monthly Notices of the Royal Astronomical Society*, 488(3):3143–3194, September 2019. doi: 10.1093/mnras/stz1182.

Kyle S. Dawson, David J. Schlegel, Christopher P. Ahn, Scott F. Anderson, Éric Aubourg, Stephen Bailey, Robert H. Barkhouser, Julian E. Bautista, Alessand ra Beifiori, Andreas A. Berlind, Vaishali Bhardwaj, Dmitry Bizyaev, Cullen H. Blake, Michael R. Blanton, Michael Blomqvist, Adam S. Bolton, Arnaud Borde, Jo Bovy, W. N. Brandt, Howard Brewington, Jon Brinkmann, Peter J. Brown, Joel R. Brownstein, Kevin Bundy, N. G. Busca, William Carithers, Aurelio R. Carnero, Michael A. Carr, Yanmei Chen, Johan Comparat, Natalia Connolly, Frances Cope, Rupert A. C. Croft, Antonio J. Cuesta, Luiz N. da Costa, James R. A. Davenport, Timothée Delubac, Roland de Putter, Saurav Dhital, Anne Ealet, Garrett L. Ebelke, Daniel J. Eisenstein, S. Escoffier, Xiaohui Fan, N. Filiz Ak, Hayley Finley, Andreu Font-Ribera, R. Génova-Santos, James E. Gunn, Hong Guo, Daryl Haggard, Patrick B. Hall, Jean-Christophe Hamilton, Ben Harris, David W. Harris, Shirley Ho, David W. Hogg, Diana Holder, Klaus Honscheid, Joe Huehnerhoff, Beatrice Jordan, Wendell P. Jordan, Guinevere Kauffmann, Eyal A. Kazin, David Kirkby, Mark A. Klaene, Jean-Paul Kneib, Jean-Marc Le Goff, Khee-Gan Lee, Daniel C. Long, Craig P. Loomis, Britt Lundgren, Robert H. Lupton, Marcio A. G. Maia, Martin Makler, Elena Malanushenko, Viktor Malanushenko, Rachel Mandelbaum, Marc Manera, Claudia Maraston, Daniel Margala, Karen L. Masters, Cameron K. McBride, Patrick McDonald, Ian D. McGreer, Richard G. McMahon, Olga Mena, Jordi Miralda-Escudé, Antonio D. Montero-Dorta, Francesco Montesano, Demitri Muna, Adam D. Myers, Tracy Naugle, Robert C. Nichol, Pasquier Noterdaeme, Sebastián E. Nuza, Matthew D. Olmstead, Audrey Oravetz, Daniel J. Oravetz, Russell Owen, Nikhil Padmanabhan, Nathalie Palanque-Delabrouille, Kaike Pan, John K. Parejko, Isabelle Pâris, Will J. Percival, Ismael Pérez-Fournon, Ignasi Pérez-Ràfols, Patrick Petitjean, Robert Pfaffenberger, Janine Pforr, Matthew M. Pieri, Francisco Prada, Adrian M. Price-Whelan, M. Jordan Raddick, Rafael Rebolo, James Rich, Gordon T. Richards, Constance M. Rockosi, Natalie A. Roe, Ashley J. Ross, Nicholas P. Ross, Graziano Rossi, J. A. Rubiño-Martin, Lado Samushia, Ariel G. Sánchez, Conor Sayres, Sarah J. Schmidt, Donald P. Schneider, C. G. Scóccola, Hee-Jong Seo, Alaina Shelden, Erin Sheldon, Yue Shen, Yiping Shu, Anže Slosar, Stephen A. Smee, Stephanie A.

Snedden, Fritz Stauffer, Oliver Steele, Michael A. Strauss, Alina Streblyanska, Nao Suzuki, Molly E. C. Swanson, Tomer Tal, Masayuki Tanaka, Daniel Thomas, Jeremy L. Tinker, Rita Tojeiro, Christy A. Tremonti, M. Vargas Magaña, Licia Verde, Matteo Viel, David A. Wake, Mike Watson, Benjamin A. Weaver, David H. Weinberg, Benjamin J. Weiner, Andrew A. West, Martin White, W. M. Wood-Vasey, Christophe Yeche, Idit Zehavi, Gong-Bo Zhao, and Zheng Zheng. The Baryon Oscillation Spectroscopic Survey of SDSS-III. *The Astronomical Journal*, 145(1):10, January 2013. doi: 10.1088/0004-6256/145/1/10.

H. Hildebrandt, F. Köhlinger, J. L. van den Busch, B. Joachimi, C. Heymans, A. Kannawadi, A. H. Wright, M. Asgari, C. Blake, H. Hoekstra, S. Joudaki, K. Kuijken, L. Miller, C. B. Morrison, T. Tröster, A. Amon, M. Archidiacono, S. Brieden, A. Choi, J. T. A. de Jong, T. Erben, B. Giblin, A. Mead, J. A. Peacock, M. Radovich, P. Schneider, C. Sifón, and M. Tewes. KiDS+VIKING-450: Cosmic shear tomography with optical and infrared data. *A&A*, 633:A69, January 2020. doi: 10.1051/0004-6361/201834878.

Martin Kilbinger. Cosmology with cosmic shear observations: a review. *Reports on Progress in Physics*, 78(8):086901, July 2015. doi: 10.1088/0034-4885/78/8/086901.

Alexie Leauthaud, Jeremy Tinker, Kevin Bundy, Peter S. Behroozi, Richard Massey, Jason Rhodes, Matthew R. George, Jean-Paul Kneib, Andrew Benson, Risa H. Wechsler, Michael T. Busha, Peter Capak, Marina Cortês, Olivier Ilbert, Anton M. Koekemoer, Oliver Le Fèvre, Simon Lilly, Henry J. McCracken, Mara Salvato, Tim Schrabback, Nick Scoville, Tristan Smith, and James E. Taylor. New Constraints on the Evolution of the Stellar-to-dark Matter Connection: A Combined Analysis of Galaxy-Galaxy Lensing, Clustering, and Stellar Mass Functions from z = 0.2 to z =1. *The Astrophysical Journal*, 744(2):159, January 2012. doi: 10.1088/0004-637X/744/2/159.

Alexie Leauthaud, Kevin Bundy, Shun Saito, Jeremy Tinker, Claudia Maraston, Rita Tojeiro, Song Huang, Joel R. Brownstein, Donald P. Schneider, and Daniel Thomas. The Stripe 82 Massive Galaxy Project - II. Stellar mass completeness of spectroscopic galaxy samples from the Baryon Oscillation Spectroscopic Survey. *Monthly Notices of the Royal Astronomical Society*, 457(4):4021–4037, April 2016. doi: 10.1093/mnras/stw117.

Alexie Leauthaud, Shun Saito, Stefan Hilbert, Alexandre Barreira, Surhud More, Martin White, Shadab Alam, Peter Behroozi, Kevin Bundy, Jean Coupon, Thomas Erben, Catherine Heymans, Hendrik Hildebrandt, Rachel Mandelbaum, Lance Miller, Bruno Moraes, Maria E. S. Pereira, Sergio A. Rodríguez-Torres, Fabian Schmidt, Huan-Yuan Shan, Matteo Viel, and Francisco Villaescusa-Navarro. Lensing is low: cosmology, galaxy formation or new physics? *MNRAS*, 467(3):3024–3047, May 2017. doi: 10.1093/mnras/stx258.

Ran Li, H. J. Mo, Zuhui Fan, Marcello Cacciato, Frank C. van den Bosch, Xiaohu Yang, and Surhud More. Modelling galaxy-galaxy weak lensing with Sloan Digital Sky Survey groups. *MNRAS*, 394(2):1016–1030, April 2009. doi: 10.1111/j.1365-2966.2009.14407.x.

Rachel Mandelbaum, Anže Slosar, Tobias Baldauf, Uroš Seljak, Christopher M. Hirata, Reiko Nakajima, Reinabelle Reyes, and Robert E. Smith. Cosmological parameter constraints from galaxy-galaxy lensing and galaxy clustering with the SDSS DR7. *Monthly Notices of the Royal Astronomical Society*, 432(2):1544–1575, June 2013. doi: 10.1093/mnras/stt572.

Federico Marinacci, Mark Vogelsberger, Rüdiger Pakmor, Paul Torrey, Volker Springel, Lars Hernquist, Dylan Nelson, Rainer Weinberger, Annalisa Pillepich, Jill Naiman, and Shy Genel. First results from the IllustrisTNG simulations: radio haloes and magnetic fields. *MNRAS*, 480(4):5113–5139, November 2018. doi: 10.1093/mnras/sty2206.

Jill P. Naiman, Annalisa Pillepich, Volker Springel, Enrico Ramirez-Ruiz, Paul Torrey, Mark Vogelsberger, Rüdiger Pakmor, Dylan Nelson, Federico Marinacci, Lars Hernquist, Rainer Weinberger, and Shy Genel. First results from the IllustrisTNG simulations: a tale of two elements - chemical evolution of magnesium and europium. *MNRAS*, 477(1):1206–1224, June 2018. doi: 10.1093/mnras/sty618.

D. Nelson, A. Pillepich, S. Genel, M. Vogelsberger, V. Springel, P. Torrey, V. Rodriguez-Gomez, D. Sijacki, G. F. Snyder, B. Griffen, F. Marinacci, L. Blecha, L. Sales, D. Xu, and L. Hernquist. The illustris simulation: Public data release. *Astronomy and Computing*, 13:12–37, November 2015. doi: 10.1016/j.ascom.2015.09.003.

Dylan Nelson, Annalisa Pillepich, Volker Springel, Rainer Weinberger, Lars Hernquist, Rüdiger Pakmor, Shy Genel, Paul Torrey, Mark Vogelsberger, Guinevere Kauffmann, Federico Marinacci, and Jill Naiman. First results from the IllustrisTNG simulations: the galaxy colour bimodality. *MNRAS*, 475(1):624–647, March 2018. doi: 10.1093/mnras/stx3040.

Dylan Nelson, Volker Springel, Annalisa Pillepich, Vicente Rodriguez-Gomez, Paul Torrey, Shy Genel, Mark Vogelsberger, Ruediger Pakmor, Federico Marinacci, Rainer Weinberger, Luke Kelley, Mark Lovell, Benedikt Diemer, and Lars Hernquist. The IllustrisTNG simulations: public data release. *Computational Astrophysics and Cosmology*, 6(1):2, May 2019. doi: 10.1186/s40668-019-0028-x.

I. Newton. *Opticks:: Or, a Treatise of the Reflexions, Refractions, Inflexions and Colours of Light. Also Two Treatises of the Species and Magnitude of Curvilinear Figures.*. Eighteenth century collections online. Smith and Walford, 1704. URL `https://books.google.dk/books?id=mxhfAAAAcAAJ`.

Gabriele Parimbelli, Matteo Viel, and Emiliano Sefusatti. On the degeneracy between baryon feedback and massive neutrinos as probed by matter clustering and weak lensing. *J. Cosmology Astropart. Phys.*, 2019(1):010, January 2019. doi: 10.1088/1475-7516/2019/01/010.

Annalisa Pillepich, Dylan Nelson, Lars Hernquist, Volker Springel, Rüdiger Pakmor, Paul Torrey, Rainer Weinberger, Shy Genel, Jill P. Naiman, Federico Marinacci, and Mark Vogelsberger. First results from the IllustrisTNG simulations: the stellar mass content of groups and clusters of galaxies. *MNRAS*, 475(1):648–675, March 2018a. doi: 10.1093/mnras/stx3112.

Annalisa Pillepich, Volker Springel, Dylan Nelson, Shy Genel, Jill Naiman, Rüdiger Pakmor, Lars Hernquist, Paul Torrey, Mark Vogelsberger, Rainer Weinberger, and Federico Marinacci. Simulating galaxy formation with the IllustrisTNG model. *MNRAS*, 473(3):4077–4106, January 2018b. doi: 10.1093/mnras/stx2656.

Planck Collaboration, N. Aghanim, Y. Akrami, M. Ashdown, J. Aumont, C. Baccigalupi, M. Ballardini, A. J. Banday, R. B. Barreiro, N. Bartolo, S. Basak, R. Battye, K. Benabed, J. P. Bernard, M. Bersanelli, P. Bielewicz, J. J. Bock, J. R. Bond, J. Borrill, F. R. Bouchet,

F. Boulanger, M. Bucher, C. Burigana, R. C. Butler, E. Calabrese, J. F. Cardoso, J. Carron, A. Challinor, H. C. Chiang, J. Chluba, L. P. L. Colombo, C. Combet, D. Contreras, B. P. Crill, F. Cuttaia, P. de Bernardis, G. de Zotti, J. Delabrouille, J. M. Delouis, E. Di Valentino, J. M. Diego, O. Doré, M. Douspis, A. Ducout, X. Dupac, S. Dusini, G. Efstathiou, F. Elsner, T. A. Enßlin, H. K. Eriksen, Y. Fantaye, M. Farhang, J. Fergusson, R. Fernandez-Cobos, F. Finelli, F. Forastieri, M. Frailis, A. A. Fraisse, E. Franceschi, A. Frolov, S. Galeotta, S. Galli, K. Ganga, R. T. Génova-Santos, M. Gerbino, T. Ghosh, J. González-Nuevo, K. M. Górski, S. Gratton, A. Gruppuso, J. E. Gudmundsson, J. Hamann, W. Handley, F. K. Hansen, D. Herranz, S. R. Hildebrandt, E. Hivon, Z. Huang, A. H. Jaffe, W. C. Jones, A. Karakci, E. Keihänen, R. Keskitalo, K. Kiiveri, J. Kim, T. S. Kisner, L. Knox, N. Krachmalnicoff, M. Kunz, H. Kurki-Suonio, G. Lagache, J. M. Lamarre, A. Lasenby, M. Lattanzi, C. R. Lawrence, M. Le Jeune, P. Lemos, J. Lesgourgues, F. Levrier, A. Lewis, M. Liguori, P. B. Lilje, M. Lilley, V. Lindholm, M. López-Caniego, P. M. Lubin, Y. Z. Ma, J. F. Macías-Pérez, G. Maggio, D. Maino, N. Mandolesi, A. Mangilli, A. Marcos-Caballero, M. Maris, P. G. Martin, M. Martinelli, E. Martínez-González, S. Matarrese, N. Mauri, J. D. McEwen, P. R. Meinhold, A. Melchiorri, A. Mennella, M. Migliaccio, M. Millea, S. Mitra, M. A. Miville-Deschênes, D. Molinari, L. Montier, G. Morgante, A. Moss, P. Natoli, H. U. Nørgaard-Nielsen, L. Pagano, D. Paoletti, B. Partridge, G. Patanchon, H. V. Peiris, F. Perrotta, V. Pettorino, F. Piacentini, L. Polastri, G. Polenta, J. L. Puget, J. P. Rachen, M. Reinecke, M. Remazeilles, A. Renzi, G. Rocha, C. Rosset, G. Roudier, J. A. Rubiño-Martín, B. Ruiz-Granados, L. Salvati, M. Sandri, M. Savelainen, D. Scott, E. P. S. Shellard, C. Sirignano, G. Sirri, L. D. Spencer, R. Sunyaev, A. S. Suur-Uski, J. A. Tauber, D. Tavagnacco, M. Tenti, L. Toffolatti, M. Tomasi, T. Trombetti, L. Valenziano, J. Valiviita, B. Van Tent, L. Vibert, P. Vielva, F. Villa, N. Vittorio, B. D. Wand elt, I. K. Wehus, M. White, S. D. M. White, A. Zacchei, and A. Zonca. Planck 2018 results. VI. Cosmological parameters. *arXiv e-prints*, art. arXiv:1807.06209, July 2018.

Sergio A. Rodriguez-Torres, Chia-Hsun Chuang, Francisco Prada, Hong Guo, Anatoly Klypin, Peter Behroozi, Chang Hoon Hahn, Johan Comparat, Gustavo Yepes, Antonio D. Montero-Dorta, Joel R. Brownstein, Claudia Maraston, Cameron K. McBride, Jeremy Tinker, Stefan Gottlöber, Ginevra Favole, Yiping Shu, Francisco-Shu Kitaura, Adam Bolton, Román Scoccimarro, Lado Samushia, David Schlegel, Donald P. Schneider, and Daniel Thomas. The clustering of galaxies in the SDSS-III Baryon Oscillation Spectroscopic Survey: modelling the clustering and halo occupation distribution of BOSS CMASS galaxies in the Final Data Release. *MNRAS*, 460(2):1173–1187, August 2016. doi: 10.1093/mnras/stw1014.

Shun Saito, Alexie Leauthaud, Andrew P. Hearin, Kevin Bundy, Andrew R. Zentner, Peter S. Behroozi, Beth A. Reid, Manodeep Sinha, Jean Coupon, Jeremy L. Tinker, Martin White, and Donald P. Schneider. Connecting massive galaxies to dark matter haloes in BOSS - I. Is galaxy colour a stochastic process in high-mass haloes? *MNRAS*, 460(2):1457–1475, August 2016. doi: 10.1093/mnras/stw1080.

Luca Scrucca. Model-based sir for dimension reduction. *Computational Statistics & Data Analysis*, 55(11):3010 – 3026, 2011. ISSN 0167-9473. doi: https://doi.org/10.1016/j.csda.2011.05.006. URL `http://www.sciencedirect.com/science/article/pii/S0167947311001721`.

Alessandro Sonnenfeld, Alexie Leauthaud, Matthew W. Auger, Raphael Gavazzi, Tommaso Treu, Surhud More, and Yutaka Komiyama. Evidence for radial variations in the stellar

mass-to-light ratio of massive galaxies from weak and strong lensing. *MNRAS*, 481(1): 164–184, November 2018. doi: 10.1093/mnras/sty2262.

Alessandro Sonnenfeld, Wenting Wang, and Neta Bahcall. Hyper Suprime-Cam view of the CMASS galaxy sample. Halo mass as a function of stellar mass, size, and Sérsic index. *A&A*, 622:A30, February 2019. doi: 10.1051/0004-6361/201834260.

Volker Springel, Simon D. M. White, Adrian Jenkins, Carlos S. Frenk, Naoki Yoshida, Liang Gao, Julio Navarro, Robert Thacker, Darren Croton, John Helly, John A. Peacock, Shaun Cole, Peter Thomas, Hugh Couchman, August Evrard, Jörg Colberg, and Frazer Pearce. Simulations of the formation, evolution and clustering of galaxies and quasars. *Nature*, 435 (7042):629–636, June 2005. doi: 10.1038/nature03597.

Volker Springel, Rüdiger Pakmor, Annalisa Pillepich, Rainer Weinberger, Dylan Nelson, Lars Hernquist, Mark Vogelsberger, Shy Genel, Paul Torrey, Federico Marinacci, and Jill Naiman. First results from the IllustrisTNG simulations: matter and galaxy clustering. *MNRAS*, 475 (1):676–698, March 2018. doi: 10.1093/mnras/stx3304.

Tommaso Treu and Philip J. Marshall. Time delay cosmography. *Astronomy and Astrophysics Reviews*, 24(1):11, July 2016. doi: 10.1007/s00159-016-0096-8.

Marco Velliscig, Marcello Cacciato, Henk Hoekstra, Joop Schaye, Catherine Heymans, Hendrik Hildebrandt, Jon Loveday, Peder Norberg, Cristóbal Sifón, Peter Schneider, Edo van Uitert, Massimo Viola, Sarah Brough, Thomas Erben, Benne W. Holwerda, Andrew M. Hopkins, and Konrad Kuijken. Galaxy-galaxy lensing in EAGLE: comparison with data from 180 deg^2 of the KiDS and GAMA surveys. *MNRAS*, 471(3):2856–2870, November 2017. doi: 10.1093/mnras/stx1789.

Mark Vogelsberger, Shy Genel, Volker Springel, Paul Torrey, Debora Sijacki, Dandan Xu, Greg Snyder, Dylan Nelson, and Lars Hernquist. Introducing the Illustris Project: simulating the coevolution of dark and visible matter in the Universe. *MNRAS*, 444(2):1518–1547, October 2014. doi: 10.1093/mnras/stu1536.

D. Walsh, R. F. Carswell, and R. J. Weymann. 0957+561 A, B: twin quasistellar objects or gravitational lens? *Nature*, 279:381–384, May 1979. doi: 10.1038/279381a0.

Rainer Weinberger, Volker Springel, Lars Hernquist, Annalisa Pillepich, Federico Marinacci, Rüdiger Pakmor, Dylan Nelson, Shy Genel, Mark Vogelsberger, Jill Naiman, and Paul Torrey. Simulating galaxy formation with black hole driven thermal and kinetic feedback. *MNRAS*, 465(3):3291–3308, March 2017. doi: 10.1093/mnras/stw2944.

Sanford Weisberg. *Applied Linear Regression*, pages 275–278. Wiley, Hoboken NJ, third edition, 2005. URL `http://www.stat.umn.edu/alr`.

Kenneth C. Wong, Sherry H. Suyu, Geoff C. F. Chen, Cristian E. Rusu, Martin Millon, Dominique Sluse, Vivien Bonvin, Christopher D. Fassnacht, Stefan Taubenberger, Matthew W. Auger, Simon Birrer, James H. H. Chan, Frederic Courbin, Stefan Hilbert, Olga Tihhonova, Tommaso Treu, Adriano Agnello, Xuheng Ding, Inh Jee, Eiichiro Komatsu, Anowar J. Shajib, Alessandro Sonnenfeld, Roger D. Bland ford, Léon V. E. Koopmans, Philip J. Marshall, and Georges Meylan. H0LiCOW XIII. A 2.4% measurement of H_0 from lensed quasars: 5.3σ

tension between early and late-Universe probes. *Monthly Notices of the Royal Astronomical Society*, June 2020. doi: 10.1093/mnras/stz3094.

Xiaohu Yang, H. J. Mo, and Frank C. van den Bosch. Constraining galaxy formation and cosmology with the conditional luminosity function of galaxies. *MNRAS*, 339(4):1057–1080, March 2003. doi: 10.1046/j.1365-8711.2003.06254.x.

F. Zwicky. Nebulae as Gravitational Lenses. *Physical Review*, 51(4):290–290, February 1937. doi: 10.1103/PhysRev.51.290.

4

Ion-induced condensation: Experiments

Increased ionization supports growth of aerosols into cloud condensation nuclei

Nature Communications, December 2017
DOI 10.1038/s41467-017-02082-2

Henrik Svensmark[1], **Martin B. Enghoff**[1], **Nir J. Shaviv**[2], **Jacob Svensmark**[1,3]

[1] National Space Institute, Technical University of Denmark, Elektrovej, Building 328, 2800 Lyngby, Denmark.

[2] Racah Institute of Physics, Hebrew University of Jerusalem, Jerusalem 91904, Israel.

[3] Dark Cosmology Centre, Niels Bohr Institute, University of Copenhagen, Juliane Maries Vej 30, 2100 Copenhagen, Denmark.

Abstract

Ions produced by cosmic rays have been thought to influence aerosols and clouds. In this study, the effect of ionization on the growth of aerosols into cloud condensation nuclei is investigated theoretically and experimentally. We show that the mass-flux of small ions can constitute an important addition to the growth caused by condensation of neutral molecules. Under atmospheric conditions the growth from ions can constitute several percent of the neutral growth. We performed experimental studies which quantify the effect of ions on the growth of aerosols between nucleation and sizes >20 nm and find good agreement with theory. Ion-induced condensation should be of importance not just in Earth's present day atmosphere for the growth of aerosols into cloud condensation nuclei under pristine marine conditions, but also under elevated atmospheric ionization caused by increased supernova activity.

4.1 Summary

A long standing paradox within the field of climate science is that our climate co-varies with solar activity. The sun provides the main influx of energy into our climate system, and it is therefore naturally expected that variations in its output would have consequences for our atmosphere. The sun varies on time scales from seconds and upwards, but the paradox is that on some of these, the amplitude of the variation is far to small to explain the correlation we see with our climate.

The term “Solar activity” encompasses a range of solar magnetic phenomena and their consequences. Notably, the sun displays a quasi-periodic activity cycle of 11-years. During the quiet period of this cycle, the surface of the sun appears homogeneous. As its activity level builds up, solar flares, ejections of magnetized coronal plasma becomes more frequent and the solar wind intensifies. At or close to peak activity, the sun reverses the orientation of its magnetic field poles. Increasing amounts of convective areas of high magnetic field line density shows as black patches or “sunspots” on the solar surface. Systematic observations of sunspot numbers extends back to the 1700, however with daily values only since 1818, and the 11-year cycle shows clearly since then [Clette et al., 2014].

The sun provides the terrestrial atmosphere with roughly 340 W/m^2 of energy through its total solar irradiance (TSI). The TSI correlates strongly with sunspot number, with am amplitude of around a tenth of a percentKirkby [2007]. Though well established, this climate forcing variation is generally recognized as too small to impact climate. However, correlations between the solar activity 11-year cycle and climate have been observed in several studies. Notably, by using the oceans as a calorimeter, four independent data sets shows an 11-year solar cycle variation of heat entering and leaving the oceans of about 1.5,W/m^2, almost a factor of 10 larger than the direct variation in TSI. This opens up the possibility of an amplification mechanism at work, which is driven or modulated by solar activity. Besides direct heating effects from the TSI, the ultraviolet (UV) component varies significantly more in some wavelengths. It has been suggested that the UV component influences the temperature of the stratosphere, which in turn could influence atmospheric circulation. Global circulation models have so far deemed the effect negligible.

Dickinson pointed to the fact that galactic cosmic rays from the interstellar medium of our Milky way are modulated by the solar magnetic field [Dickinson, 1975]. Cosmic rays consist mainly of energetic protons and act as the main ionizing agent of the atmosphere. Dickinson [1975] suggests that ions might affect cloud radiative properties by influencing atmospheric aerosols and their action as cloud condensation nuclei. Since then, multiple studies have pointed to observational correlations in support of this hypothesis. Svensmark and Friis-Christensen [1997] found correlations between cosmic rays flux and global cloud coverage from the International Satellite Cloud Climatology Project (ISCCP) data through most of a solar cycle. The correlation has been less apparent on longer time scales, however firm conclusions are hindered by the the difficulty of obtaining long term stability in satellite measurements of cloud cover. On timescales of millennia, cosmogenic isotopes can be used

as a proxy of cosmic ray flux over the last 10-thousand years. Δ^{14}C records from tree rings correlate beautifully to the $\delta^{18}O$ record of a stalagmite in a cage in northern Oman [Neff et al., 2001]. $\delta^{18}O$ is here used as a proxy for the monsoon rainfall intensity, and the correlation with Δ^{14}C links cosmic rays to climate. Δ^{14}C and Δ^{10}Be from ice cores have similarly been correlated to the amount of ice raft debris extracted from deep sea sediment cores. This link however rests on the assumption that the TSI has not changed notably during this time, however long term variations in solar irradiance has not been ruled out.

On shorter time scales, coronal mass ejections and their subsequent week-long Forbush decrease of the atmospheric cosmic ray flux has been found to correlate with cloud properties. One study found significant signals in 3 independent satellite based cloud data sets and one ground based aerosol data setSvensmark et al. [2009]. Other studies of this phenomenon have detected no Forbush decrease signal, and the IPCC summary of the field is that no firm conclusion is reached on the issue. In summary, there has been much discussion of what constitutes a Forbush decrease, and how the statistical processing of observations should be performed. Svensmark et al. [2016] expands on the Svensmark et al. [2009] Forbush decrease list, ranked after ionization impact on the lower atmosphere, and defines a statistical bootstrap MC for determining the significance of an observed impact. In this study, correlations between cosmic ray flux and several cloud parameters measured by the MODIS instrument aboard the Terra satellite and ISCCP satellite network. Work is continuing in this field, and promising results are found in the failure of weather models to predict cloud behaviour during Forbush decreases [Kaas et al., 2019].

The scientific discussion surrounding the above correlations emphasize the need for a microphysical or chemical mechanism that directly links cosmic rays to clouds. This has been approached in the laboratory through the use of atmospheric reaction chambers, in which sulfuric aerosol formation and growth can be facilitated and monitored. In Svensmark et al. [2007] it was shown that increasing ionization levels inside an experimental environment replicating marine air conditions caused an increase on the nucleation of atmospheric aerosols at the 1 nm scale. This was later reproduced in the CLOUD project at CERN [Duplissy et al., 2010, Kirkby et al., 2011]. The now fairly established process of ion-induced nucleation put an experimental link between cosmic rays and the formation of aerosol formation. However, whether or not changes in aerosol *nucleation* translates into changes in *cloud condensation nuclei* remained to be shown.

The executive summary of Chapter 7 of the IPCC of 2013 report states that:

> *Cosmic rays enhance new particle formation in the free troposphere, but the effect on the concentration of cloud condensation nuclei is too weak to have any detectable climatic influence during a solar cycle or over the last century (medium evidence, high agreement). No robust association between changes in cosmic rays and cloudiness has been identified.* ***In the event that such an association existed, a mechanism other than cosmic ray-induced nucleation of new aerosol particles would be needed to explain it.*** *[Boucher et. al, 2013]*

In the article below, a mechanism that associates ions with aerosol growth rate enhancements is presented and measured in the laboratory. It is shown that aerosol growth rate is proportional to the ion concentration, due to the mass influx of the rapidly charging and discharging ions of the aerosols. A theoretical description of this mechanism as an additional source of growth by condensation is formulated, and shown to be consistent with a series of laboratory growth profiles of an aerosol population. The experiments were performed using an 8 m^3 atmospheric reaction chamber located at the Technical University of Denmark. In parallel, a numerical model was being developed for simulating aerosol growth processes while taking charge into consideration. The next article introduces this model, and shows that it reproduces the ion-induced condensation result, and a first effort to put the effect in context of other aerosol growth processes from a theoretical and numerical perspective is presented. It is shown, that charged condensation changes growth dynamics of aerosol, but that it is an ion-density independent process, leaving ion-induced condensation as candidate linking mechanism for the link between solar variations and terrestrial climate.

The future of the ion-condensation mechanism points towards implementation in global circulation models. This is necessary a necessary step to explore whether ions can actually affect the global aerosol distribution though ion-condensation, and specifically how cloud condensation nuclei concentrations are affected. If ion-condensation is found to be a significant aerosol modulating agent, it would spawn research into optimal conditions for it to work. The geospatial location of the strongest signal may inspire future observational efforts on cloud formation, past climate conditions could be simulated top gain understanding of climate variations during the holocene period. Finally it may put further constrains on aerosol growth and cloud formation feedback mechanisms, which is currently one the largest sources of uncertainty in our climate understanding.

4.2 Introduction

Clouds are a fundamental part of the terrestrial energy budget, and any process that can cause systematic changes in cloud micro-physics is of general interest. To form a cloud droplet, water vapour needs to condense to aerosols acting as cloud condensation nuclei (CCN) of sizes of at least 50-100 nm [Seinfeld and Pandis, 2006], and changes in the number of CCN will influence the cloud microphysics [Twomey et al., 1987, Pierce and Adams, 2009]. One process that has been pursued is driven by ionization caused by cosmic rays, which has been suggested to be of importance by influencing the density of CCN in the atmosphere and thereby Earth's cloud cover [Dickinson, 1975, Svensmark and Friis-Christensen, 1997, Svensmark et al., 2009, 2016]. Support for this idea came from experiments, which demonstrated that ions significantly amplify the nucleation rate of small aerosols (≈ 1.7 nm) [Svensmark et al., 2007, Kirkby et al., 2011]. However, to affect cloud properties, any change in small aerosols needs to propagate to CCN sizes 50-100 nm, but such changes were subsequently found by numerical modelling to be too small to affect clouds [Pierce and Adams, 2009, Snow-Kropla et al., 2011, Yu and Luo, 2014]. The proposed explanation for this deficit is that additional aerosols reduce the concentration of the gases from which the particles grow, and a slower growth increases the probability of smaller aerosols being lost to pre-existing aerosols. This has lead to the conclusion that no significant link between cosmic rays and clouds exists in Earth's atmosphere.

This conclusion stands in stark contrast to a recent experiment demonstrating that when excess ions are present in the experimental volume, all extra nucleated aerosols can grow to CCN sizes [Svensmark et al., 2013]. But without excess ions in the experimental volume, any extra small aerosols (3 nm) are lost before reaching CCN sizes, in accordance with the above mentioned model results. The conjecture was that an unknown mechanism is operating, whereby ions facilitate the growth and formation of CCN. Additional evidence comes from atmospheric observations of sudden decreases in cosmic rays during solar eruptions in which a subsequent response is observed in aerosols and clouds [Svensmark et al., 2009, 2016]. Again, this is in agreement with a mechanism by which a change in ionization translates into a change in CCN number density. However, the nature of this micro-physical link has been elusive.

In this work we demonstrate, theoretically and experimentally, the presence of an ion-mechanism, relevant under atmospheric conditions, where variations in the ion-density enhance the growth rate from condensation nuclei (≈ 1.7 nm) to CCN. It is found that an increase in ionization results in a faster aerosol growth, which lowers the probability for the growing aerosol to be lost to existing particles, and more aerosols can survive to CCN sizes. It is argued that the mechanism is significant under present atmospheric conditions and even more so during prehistoric elevated ionization caused by a nearby supernova. The mechanism could therefore be a natural explanation for the observed correlations between past climate variations and cosmic rays, modulated by either solar activity [Eddy, 1976, Svensmark, 1998, Neff et al., 2001, Bond et al., 2001, Shaviv, 2008] or caused by supernova activity in the solar

neighbourhood on very long time scales where the mechanism will be of profound importance [Shaviv, 2002, 2003, Svensmark, 2012].

4.3 Results

4.3.1 Theoretical model and predictions

Cosmic rays are the main producers of ions in Earth's lower atmosphere [Laakso et al., 2004]. These ions interact with the existing aerosols, and charge a fraction of them. However, this fraction of charged aerosols is independent of the ionization rate in steady state—even though the electrostatic interactions enhance the interactions among the charged aerosols and between these aerosols and neutral molecules, the increased recombination ensures that the equilibrium aerosol charged fraction remains the same [Hoppel, 1985]. Ion induced nucleation will cause the small nucleated aerosols to be more frequently charged relative to an equilibrium charge distribution, but ion-recombination will move the distribution towards charge equilibrium, typically before the aerosols reach ~ 4 nm [Laakso et al., 2007]. Changing the ionization is therefore not expected to have an influence on the number of CCN through Coulomb interactions between aerosols.

However, this argument disregards that the frequency of interactions between ions and aerosols is a function of the ion density, and that each time an ion condenses onto an aerosol, a small mass (m_{ion}) is added to the aerosol. As a result, a change in ion density has a small but important effect on the aerosol growth rate, since the mass flux from the ions to the aerosols increases with the ion density. This mass flux is normally neglected when compared to the mass flux of neutral molecules (for example sulphuric acid, SA) to the aerosols by condensation growth, as can be seen from the following simple estimate: The typical ion concentration in the atmosphere is on the order of $\approx 10^3$ ions cm^{-3}, however, the condensing vapour concentration (SA) is typically on the order of $\approx 10^6$ molecules cm^{-3}. The ratio between them is 10^{-3}, from which one might conclude that the effect of ions on the aerosol growth is negligible. Why this is not always the case will now be shown.

The mass flux to neutral aerosols consists not only of the condensation of neutral molecules, but also of two terms which add mass due to recombination of a positive (negative) ion and a negative (positive) aerosol. Furthermore, as an ion charges a neutral aerosol, the ion adds m_{ion} to its mass. Explicitly, taking the above mentioned flux of ion mass into account, the growth of aerosols by condensation of a neutral gas and singly charged ions becomes,

$$\frac{\partial N^i(r,t)}{\partial t} = -\sum_j \frac{\partial}{\partial r} I_{i,j}(r,t) N^j(r,t), \tag{4.1}$$

$$I_{i,j}(r,t) = \begin{pmatrix} A^0 n^0 \beta^{00} & A^- n^- \beta^{-+} & A^+ n^+ \beta^{+-} \\ A^+ n^+ \beta^{+0} & A^0 n^0 \beta^{0+} & 0 \\ A^- n^- \beta^{-0} & 0 & A^0 n^0 \beta^{0-} \end{pmatrix},$$

with i and $j = (0, +, -)$ referring to neutral, positively, and negatively charged particles. Here r and t are the radius of the aerosol and the time. $N^i = (N^0, N^+, N^-)$ is the number density of neutral, positive, and negative aerosols. n^0 is the concentration of condensible gas, $n^+,\ n^-$ are the concentration of positive and negative ions, while $A^i = (m^i/4\pi r^2\rho)$, with m^i being the mass of the neutral gas molecule ($i = 0$), and the average mass of positive/negative ions, $i = (+, -)$, ρ is the mass density of condensed gas, and β is the interaction coefficient between the molecules (or ions) and neutral and/or charged aerosols (see Methods section).

β^{00}, β^{+0}, and β^{-0} correspond to the interaction coefficients describing the interaction between neutral aerosols of radius r and neutral molecules, positive ions and negative ions respectively, whereas β^{0+}, and β^{0-} are the interaction coefficients between neutral molecules and positively/negatively charged aerosols. Finally β^{+-} corresponds to the recombination between a positive ion and a negative aerosol of radius r, and vice versa for β^{-+} [Yu and Turco, 1998]. If no ions are present, the above equations simplify to the well known condensation equation [Seinfeld and Pandis, 1998], where

$$I_{0,0}(r,t) = \frac{dr}{dt} = A^0 n^0 \beta^{00}, \tag{4.2}$$

is the growth rate of the aerosol radius due to the condensation of molecules onto the aerosols. It is the change in growth rate caused by ions that is of interest here.

By assuming a steady state for the interactions between ions and aerosols, we find [Hoppel, 1985]

$$\frac{N^+}{N^0} = \frac{n^+\beta^{+0}}{n^-\beta^{-+}}, \qquad \frac{N^-}{N^0} = \frac{n^-\beta^{-0}}{n^+\beta^{+-}}, \tag{4.3}$$

which using $N^{\mathrm{tot}} = N^0 + N^+ + N^-$ gives

$$\frac{N^0(r,t)}{N^{\mathrm{tot}}(r,t)} = \left[1 + \frac{n^+\beta^{+0}}{n^-\beta^{-+}} + \frac{n^-\beta^{-0}}{n^+\beta^{+-}}\right]^{-1}. \tag{4.4}$$

Eqs. (4.3) and (4.4) can be inserted into the components of Eqs. (4.1) (for $i = (0, +, -)$). Assuming symmetry between the positive and negative charges, i.e. $m_{ion} \equiv m^+ = m^-$, $\beta^{\pm 0} \equiv \beta^{-0} = \beta^{+0}$, $\beta^{\pm\mp} \equiv \beta^{+-} = \beta^{-+}$ and $n_{ion} \equiv n^+ = n^-$, finally leads to (see also Methods section):

$$\frac{\partial N^{\mathrm{tot}}(r,t)}{\partial t} = -\frac{\partial}{\partial r}\left[A_0 n^0 \beta^{00}\left(1+\Gamma\right) N^{\mathrm{tot}}(r,t)\right], \tag{4.5}$$

where

$$\Gamma = 4\left(\frac{n_{\mathrm{ion}}}{n_0}\right)\left(\frac{\beta^{\pm 0}}{\beta^{00}}\right)\left(\frac{m_{\mathrm{ion}}}{m_0}\right)\left(\frac{N^0(r,t)}{N^{\mathrm{tot}}(r,t)}\right). \tag{4.6}$$

The 1 term appearing in Eq. (4.5) is the result of the approximation $(1+2(\beta^{0\pm}\beta^{\pm 0})/(\beta^{\pm\mp}\beta^{00}))/(1+2\beta^{\pm 0}/\beta^{\pm\mp}) \approx 1$, good to $3{\cdot}10^{-4}$ for a 10 nm aerosol and decreasing for $d > 10$ nm. The bracketed term in Eq. (4.5) is related to the rate of change in the aerosol radius:

$$\frac{dr}{dt} = A_0 n^0 \beta^{00}\left[1+\Gamma\right]. \tag{4.7}$$

This growth rate is one of the characteristic equations describing aerosol evolution, and it is valid independent of any losses [Kuang et al., 2009].

It is Γ, in Eq. (4.6), which quantifies the net effect of ion condensation. The term $4(\beta^{\pm 0}/\beta^{00})(N^0/N^{\mathrm{tot}})$ depends on electro-static interactions, and where (n_{ion}/n_0) and (m_{ion}/m_0) depend on the specific concentrations and parameters. Fig. 4.1a) portrays this part together with $(\beta^{\pm 0}/\beta^{00})$ and (N^0/N^{tot}). Fig. 4.1b depicts the size of Γ in % of the neutral condensation, as a function of the ionization rate q and diameter d of the aerosols for an average atmospheric sulfuric acid concentration of $n^0 \approx 1 \cdot 10^6$ molecules cm^{-3} and $m_0 = 100$ AMU and a mass ratio (m_{ion}/m_0) of 2.25 (see Methods section). It should be noted that the terms $\beta^{\pm 0}$ and β^{00} also depend on the mass and diameter of the ions and neutral molecules, which may vary depending on composition. Both exact masses and the mass asymmetry between ions can vary - observationally positive ions tend to be heavier than negative ions [Hõrrak et al., 1998]. There are additional caveats to the theory, which will be examined in the Discussion section.

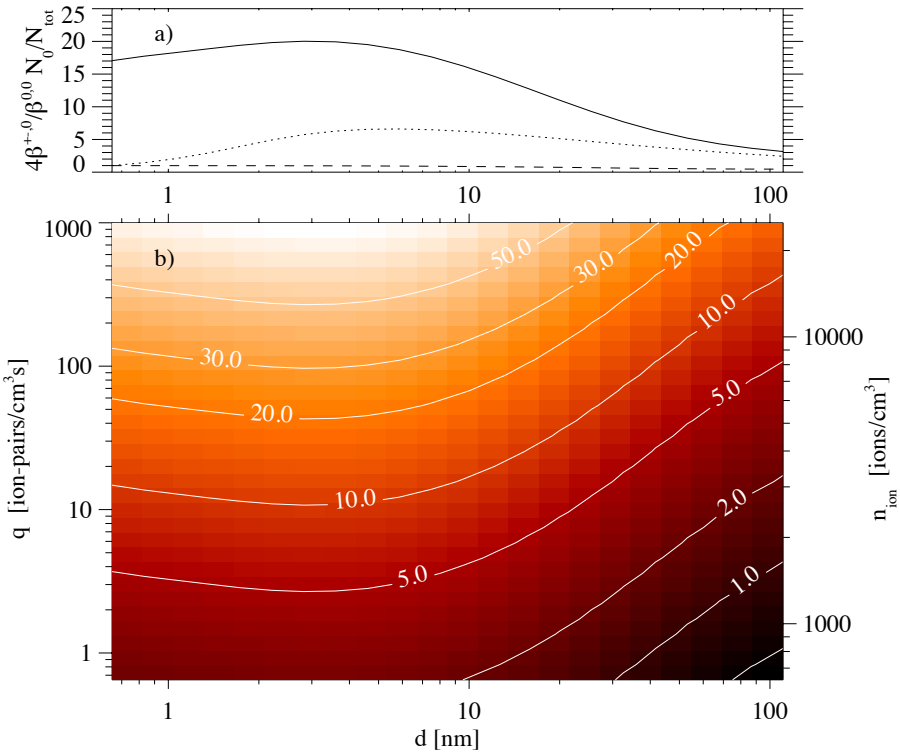

Figure 4.1: Calculation of ion contribution to growth. a) The average relative electrostatic enhancement $4(\beta^{\pm 0}/\beta^{00})(N^0/N^{\mathrm{tot}})$ between ions and aerosols of diameter d (solid line). The dotted line is $(\beta^{\pm 0}/\beta^{00})$, and the dashed line is (N^0/N^{tot}). b) The relative size of the ion condensation, Γ (Eq. 4.6) in %, in an atmosphere with a condensible gas concentration of $1{\cdot}10^6$ molecules cm^{-3} as a function of aerosol diameter d and ionization rate q (left hand axis) or ion density (right hand axis). The contour lines show the relative size of the growth due to ion condensation in % of the usual condensation growth. The mass ratio (m_{ion}/m_0) is set to 2.25, and the mass of the neutral molecule is set to 100 AMU.

4.3.2 Experimental Results

We now proceed to show that the predictions of the theory of ion-induced condensation outlined above can be measured in experiments. The latter were done in an 8 m^3 stainless steel reaction chamber [Svensmark et al., 2013]. Due to wall losses, the growth rate of the aerosols could not be too slow, therefore the sulphuric acid concentration needed to be larger than $n^0 \approx 2{\cdot}10^7$ molecules cm^{-3}. This decreases the effect that ionization has on the aerosol growth by more than an order of magnitude when compared to typical atmospheric values. It is however a necessary constraint given the finite size of the chamber. The number of nucleated particles had to be low enough that coagulation was unimportant, thus keeping the growth fronts in size-space relatively sharp, allowing accurate growth rate measurements.

The ionization in the chamber could be varied from 16 to 212 ion-pairs cm^{-3} s^{-1} using two γ-sources. At maximum ionization, the nucleation rate of aerosols was increased by $\sim$30% over the minimum ionization.

The experiments were performed with a constant UV photolytic production of sulfuric acid, and every 4 (in some cases 2) hours the ionization was changed from one extreme to the next, giving a cycle period P of 8 (or 4) hours (see Methods section). The effect of ion-induced nucleation during the part of the cycle with maximum ionization results in an increased formation of new aerosols (see Fig. 4.2 a). To improve the statistics, the cycle P was repeated up to 99 times. A total of 11 experimental runs were performed, representing 3100 hours. Each data set was subsequently superposed over the period P resulting in a statistically averaged cycle. An example of a superposed cycle can be seen in Fig. 4.2 b), where locations of the transition regions between the low and high aerosol density data can be used to extract the effect of ions on aerosols growth. The two transitions determine two trajectories, profile 1 and profile 2, in the (d, t)-plane, from which it is possible to estimate the difference in the growth time to a particular size d (see Methods section). A CI API-ToF mass spectrometer was used to measure the sulphuric acid concentration during some of the experiments and to estimate the average ion mass [Jokinen et al., 2012].

The above theory predicts a difference in the time it takes the two profiles to reach a size r due to a growth velocity difference caused by ion condensation. The time it takes for aerosols to grow to size r along the two possible profiles is expressed as

$$t_i(r) \quad = \quad \int_0^r \left[\left(\frac{dr}{dt} \right)_i \right]^{-1} dr, \tag{4.8}$$

where t_1 and t_2 refers to the time it takes profile 1 and 2 to reach size r. The integrand is given by Eq. (4.7) and it considers that after half the period, the γ-sources are switched off (or on). The above equations can be integrated numerically to find $\Delta T = t_2(r) - t_1(r)$ and allow comparison with the experiments.

During the first $\sim$12 nm of growth, profile 1 grows with the γ-sources on and it thus grows faster than profile 2 in the γ-off region, consequently, $t_1(r) < t_2(r)$ and ΔT is increasing (see Fig. 4.2 b)). This increase is du e to the (nearly) constant difference in growth rate

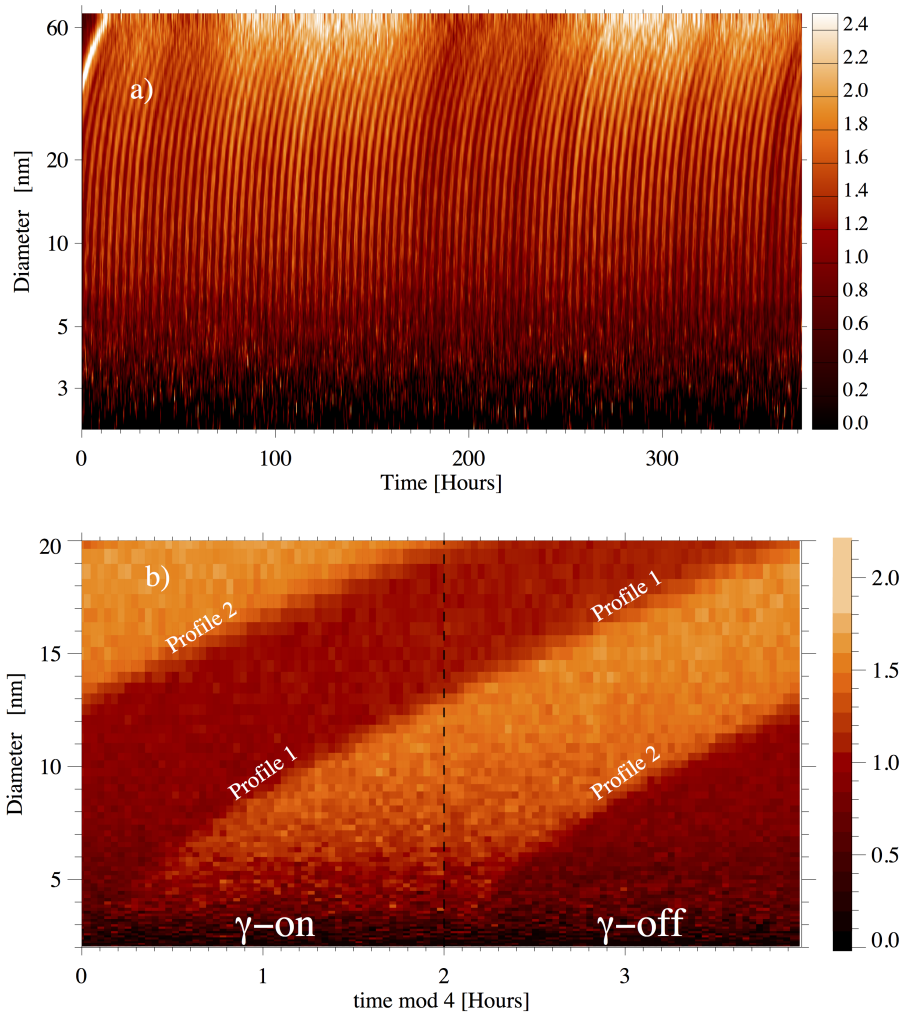

Figure 4.2: Experimental growth profiles. a) Aerosol number density $N^{\mathrm{tot}}(d,t)/(1/T\int_0^T N^{\mathrm{tot}}(d,t')dt')$, normalized by the average of 97 cycles of 4 hours ($T = 388$ hours), as a function of diameter d and time t. b) Data superposed over the 4 hour period. The time $t_1(d)$ (or $t_2(d)$) that the profile 1 (or profile 2) reaches d is determined by the local maximum of a Gaussian fit to $(dN^{\mathrm{tot}}(d,t)/dt)^2$ (see Methods section). Note that profile 1 (profile 2) is initially growing with γ-on (γ-off) until $d \approx 13$ nm. However when $d > 13$ nm profile 1 (profile 2) grows with γ-off (γ-on). It is the difference in timing of profile 1 and 2 that contain information about the effect of ions on the growth rate.

between the two profiles. But when profile 1 enters the second part of the cycle, when the γ-sources are off, profile 2 enters the high ion state and is now growing faster than profile 1. Therefore, it is now profile 2 that grows faster and ΔT starts to decrease. Figure 4.3 depicts three examples of ΔT as a function of the diameter d. It is seen that the data scatter around the theoretical curves (red (γ-on) and blue (γ-off)) obtained from Eqs. (4.7) & (4.8). The grey curves were produced by performing a LOESS smoothing of the experimental data. It also indicates that the enhanced growth is continuing up to at least 20 nm, and in good agreement with theory. Note that although some of the experiments contain size distribution data above 20 nm, the profiles at those sizes become poorly defined at which point we stop the analysis. All 11 experimental runs are summarized in Fig. 4.4, where ΔT is averaged between 6 and 12 nm, and shown as a function of the SA concentration, which is obtained from either CI-API-ToF measurements and/or slopes of the growth profiles. The red curve is

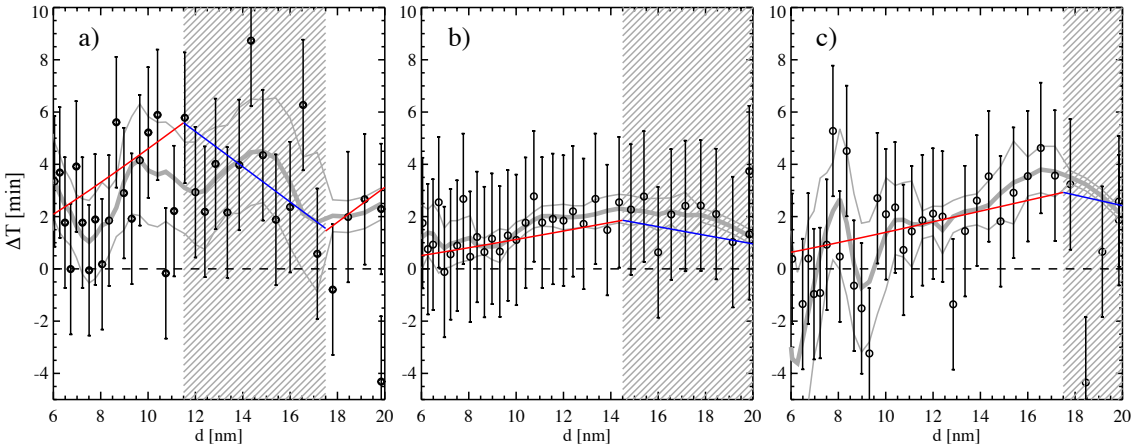

Figure 4.3: Temporal evolution of growth time difference. Three examples of growth time differences ΔT versus diameter is shown as black diamond symbols along with 1 std. dev. uncertainty. Red (Blue) curves are the theoretical expectations during gamma on(off) periods based on numerical integration of Eqs. (4.7). a) Experimental run V9 (see Fig. 4.4), based on 45 cycles of 8 hours. b) Experimental run V11, based on 99 cycles of 8 hours. c) Experimental run V7, based on 4 cycles of 8 hours. The hatched regions denotes growth periods in the γ-off state. The grey curves are a LOEES smoothing of the experimental data, together with the 1 std. dev. uncertainty. The scattering of points is smallest for run V11, which has the most cycles.

the theoretical expectation for the γ-sources at maximum, and the blue curve is obtained with a 45% reduction in the ion-density. Both are found by numerically solving Eqs. (4.7) & (4.8). The relative importance of ion condensation increases as the SA concentration is lowered, as predicted and in good agreement with theory.

4.4 Discussion

The most common effect of ions considered in aerosol models is aerosol charging which increases the interaction between the charged aerosols and neutral aerosols/molecules, thereby increasing aerosol growth. However, as mentioned previously, the ion-density does not affect the steady state fraction of aerosols that are charged such that the ion induced interactions remain nearly constant, implying that no effect on the aerosol growth is expected by changing the background ionization. Nonetheless, experiments and observations do suggest that ions have an effect on the formation of CCN, the question has therefore been, how is this possible?

The present work demonstrates that the mass flux associated with the aerosol charging by ions and ion-aerosol recombination is important and should not be neglected. Γ in Eq. (4.7) contains the effect of the mass-flux of ions to aerosols and demonstrates the inherent amplifications by the interaction between the ions and aerosols. This function Γ shows that the initial estimate of the mass-flux, $(n_{\text{ion}}/n^0) = 10^{-3}$, made in the introduction, gets multiplied by the size dependent function $4(\beta^{\pm 0}/\beta^{00})(\frac{m_{\text{ion}}}{m_0})(N_0/N_{tot})$ which at maximum is about 60 ($m_{\text{ion}}/m_0 \sim 2.25$), and therefore nearly two orders of magnitude larger, than the naive estimate. The simple expression for the growth rate, Eq. (4.7), can conveniently be used as a parametrization in global aerosol models.

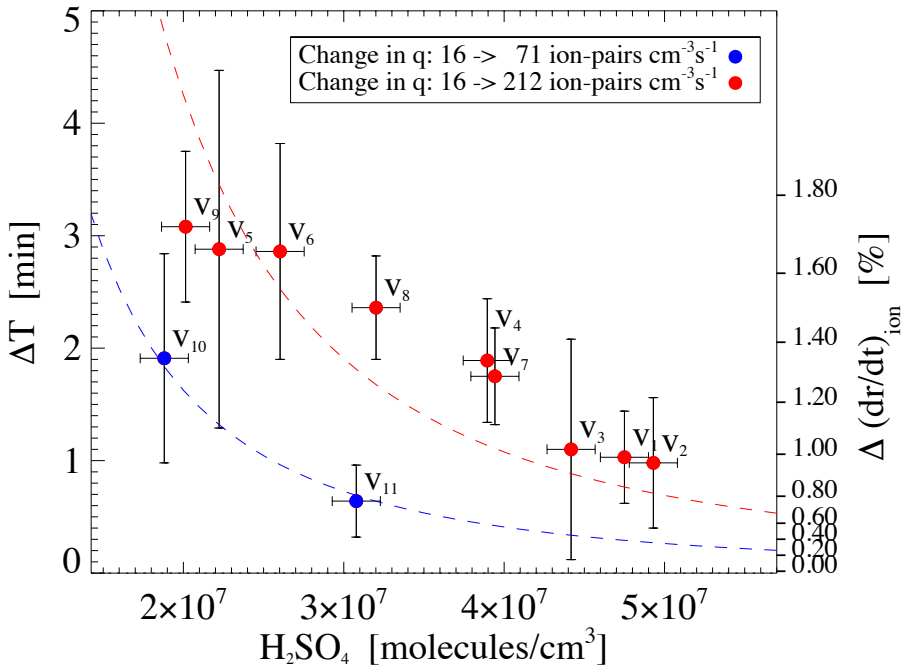

Figure 4.4: Comparison of experiments and theory. Time difference between γ-on profile and γ-off profile averaged between d=6 nm and d=12 nm as a function of sulfuric acid concentration. The red circle symbols are for Δq = 196 ion-pairs cm^{-3} s^{-1} and blue circles are for Δq = 55 ion-pairs cm^{-3} s^{-1}. Errorbars are the 1 std. dev. uncertainty. The red (blue) curve is the theoretical expectation based on Eqs. (4.7) and (4.8). Right-hand axis is the relative change in growth rate averaged between d=6 nm and d=12 nm, in %.

As a test of the theoretical model, extensive experiments were performed to study the effect on growth of the flux of ion-mass to the aerosols. One complication in the experiments was that aerosols were lost to the walls of the chamber. This meant that the concentration of SA could not be as low as the typical values in the atmosphere $\sim 10^6$molecules cm^{-3}, but had to be higher than $\sim 2{\cdot}10^7$molecules cm^{-3}. Therefore, the relative effect on the growth caused by the ions was more than an order of magnitude smaller, as can be seen from Eq. (4.7). The experimental challenge was therefore to measure a $< 1\%$ change in growth rate, which was done by cyclic repeating the experiments up to 99 times and average the results in order to minimize the fluctuations, with a total of 3100 hours of experiments. Figs. 4.3 and 4.4 demonstrate both the importance of varying the neutral SA gas concentration and the effect of changing the ion-density, and show excellent agreement with the theoretical expectations. One important feature is that the effect on the growth rate continues up to $\sim$ 20 nm, as can be seen in Fig. 4.3, which is larger sizes than predicted for charged aerosols interacting with neutral molecules [Yu and Turco, 2001, Nadykto and Yu, 2003, Lushnikov and Kulmala, 2004], and is expected to increase for atmospherically relevant concentrations of SA. It should be noted that the early stages of growth are very important since the smallest aerosols are the most vulnerable to scavenging by large pre-existing aerosols, and by reaching larger sizes $\sim$20 nm faster, the survivability increases fast.

The presented theory is an approximation to a complex problem, and a number of simplifications have been made which gives rise to some questions. We will now discuss the most pertinent: Will the material that constitute the ions condense onto the aerosols in any case

as neutral molecules? This will certainly be the case for the negative HSO_4^- ions. Assuming that all negative ions, n^-, are HSO_4^-, then the number of neutral SA molecules would be $n_0 - n^-$, where n^- is the total negative ion-density. Inserting values in the right hand side of Eq. (4.7), for example for the present experiment $n_0 \sim 10^7$ molecules cm^{-3}, and $n^- \sim 10^4$ ions cm^{-3} the correction to the growth rate from the decrease in neutral molecules is, $\mid \Delta(dr/dt)/(dr/dt) \mid \sim \mid ((n^0 - n^-) - n^0)/n^0 \mid < 10^{-3}$, but the ion condensation impact on the growth rate is of the order 10^{-2} (see Fig. 4.4) and therefore an order of magnitude smaller. So even if the neutral molecules would condense eventually, it does not change the estimated growth rate by ion condensation significantly. This would also be the case under atmospheric conditions, where n_0 is of the order 10^6 cm^{-3} and $n_{ion} \sim 10^3$ ions cm^{-3}, again a correction an order of magnitude lower than the ion condensation effect. Also note that the mass-flux from ions is larger than from the neutral molecules, which is part of the faster growth rate. In fact, even if the larger particles grow slightly slower due to a decrease in neutral molecules, the growth rate of the smaller particles is enhanced due to the ion-interactions, which make the cross-section of the small particles larger (e.g., see Fig. 4.5). This leads to the second question: Will the ion-mass that condenses onto the small aerosols stay in the aerosol and not evaporate after the aerosol is neutralized? This is slightly more difficult to answer, since the composition of all the ions are not known. The abundant terminal negative HSO_4^- ions are not more likely to evaporate than the neutral SA molecules. With respect to unknown positive or negative ions the possibility of evaporation is more uncertain. If the material of some of the ions are prone to evaporate more readily, it would of course diminish the ion effect. The present experimental conditions did not indicate that this was a serious problem, but in an atmosphere of e.g. more volatile organics it could be. Another issue is that sulphate ions typically carry more water than their neutral counterparts [Kurtén et al., 2007], and it is uncertain what happens with this excess water after neutralization of the aerosol. It was also assumed that the ion-density was in steady state with the aerosol density at all times. This is of course an approximation, but from measurements of the ion-density with a Gerdien tube [Gerdien, 1905] the typical time scale for reaching steady state is minutes and the assumption of an ion-density in steady state is thus a reasonable approximation [Svensmark et al., 2013]. It is worth noting that in the experiments two types of losses for ions are present, in addition to recombination: Wall losses and condensation sink to aerosols. Based on the loss rate of sulphuric acid the wall loss rate is about $7 \cdot 10^{-4}$ s^{-1}, while the condensation sink for experiment V2 was $1.2 \cdot 10^{-4}$ s^{-1}. This means that the wall losses were dominant and changes in the aerosol population will thus have a minimal influence on the ion concentration. Furthermore recombination is by far the dominant loss mechanism for ions. For an ion production rate of 16 cm^{-3} s^{-1} the actual ion concentration is 92% of what a calculation based only on recombination gives - for larger ion production the recombination becomes more dominant and vice versa. Under atmospheric conditions of high condensation sink and low ion production this may constitute a significant decrease to the effect due to the reduced ion concentration, but under clean conditions and in the experiment the condensation sink has an minor effect. In order to calculate the interaction coefficients between ions and aerosols it is necessary to know the mass of the ions and mass of the aerosols. This is complex due to the many ion species and their water content, and as a simplification an average ion mass was chosen to be 225 AMU. The sensitivity of the theory to changes in ion mass in the range (130-300 AMU) and mass of a neutral SA molecule in the range (100-130) could change the important ratio $\left(\beta^{\pm 0}/\beta^{00}\right)$ by up to 20%. The possible

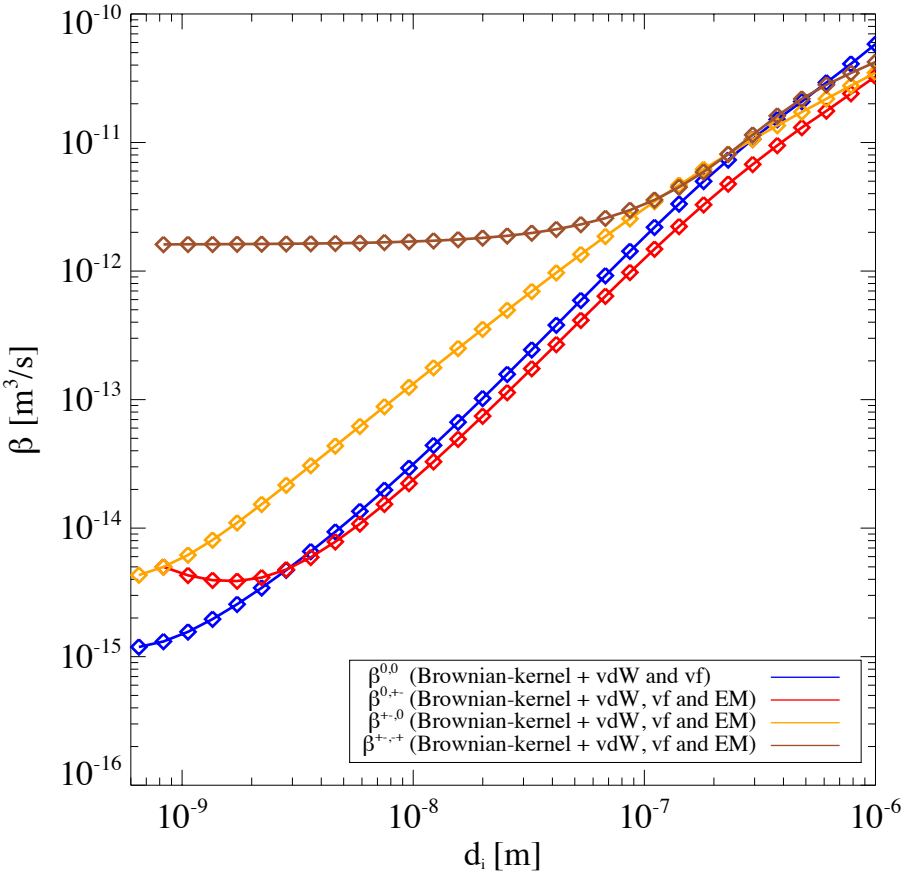

Figure 4.5: Interaction coefficients. The interaction coefficients between a small neutral particle of mass 100 AMU and a small ion of mass 225 AMU interacting with aerosols of diameter d. The interaction between neutral particles, β^{00}, is given by the blue curve, the interaction between small neutral particles and charged aerosols, $\beta^{0\pm}$, is given by the red curve. The interaction between a positive or negative ion and neutral aerosols, $\beta^{\pm 0}$, is described with the yellow curve. Finally, the recombination coefficient between two oppositely charged particles is given by the brown curve. The coefficients were calculated assuming Brownian diffusion while including Van der Waals-forces, Coulomb-forces (including image charges) and viscous forces [Yu and Turco, 1998]. Symmetry between positive and negative ions has been assumed, see text.

relevance of the presented theory in Earth's atmosphere will now be discussed. From Eq. 4.6, the factor (n_{ion}/n^0) indicates that the relative importance of ion condensation will be largest when the concentration of condensing gas n_0 is small and the ion density is large. Secondly, the number density of aerosols should also be small so the majority of ions are not located on aerosols. This points to pristine marine settings over the oceans, away from continental and polluted areas. Results based on airborne measurements suggest that the free troposphere is a major source of CCN for the Pacific boundary layer, where nucleation of new aerosols in clean cloud processed air in the Inter-Tropical Convergence Zone are carried aloft with the Hadley circulation and via long tele-connections distributed over $\sim \pm$ 30 deg latitude [Clarke et al., 1999, 2013]. In these flight measurements, the typical growth rate of aerosols was estimated to be of the order $\sim$ 0.4 nm/hour [Clarke et al., 2013], which implies an average low gas concentration of condensing gas of $n_0 \sim 4 \cdot 10^6$ molecules cm^{-3}. Measurements and simulations of SA concentration in the free troposphere annually averaged over day and night is of the order $n_0 \sim 10^6$ molecules cm^{-3}p[Dunne et al., 2016]. This may well be consistent

with the above slightly larger estimate, since the aerosol cross-section for scavenging smaller aerosols increases with size, which adds to the growth rate. Secondly, the observations suggest that as the aerosols enters the marine boundary layer, some of the aerosols are further grown to CCN sizes [Clarke et al., 2013]. Since the effect of ion condensation scales inversely with n_0, a concentration of $n_0 \sim 4 \cdot 10^6$ molecules cm^{-3} would diminish the effect by a factor of four. As can be seen in Fig. 4.1b, the effect of ion condensation for an ionization rate of $q = 10$ ion-pairs cm^{-3}s^{-1} would change from 10% to 2.5% which may still be important. Note that other gasses than sulphuric acid can contribute to n_0 in the atmosphere. As aerosols are transported in the Hadley circulation they are moved in to the higher part of the troposphere where the intensity and variation in cosmic rays ionization are the largest [Bazilevskaya et al., 2008]. This suggests that there are vast regions where conditions are such that the proposed mechanism could be important, i.e. where aerosols are nucleated in Inter-Tropical Convergence Zone and moved to regions where relative large variations ionization can be found. Here the aerosols could grow faster under the influence of ion condensation, and the perturbed growth rate will influence the survivability of the aerosols and thereby the resulting CCN density. Finally the aerosols are brought down and entrained into the marine boundary layer, where clouds properties are sensitive to the CCN density [Twomey et al., 1987].

Although the above is on its own speculative, there are observations to further support the idea. On rare occasions the Sun ejects solar plasma (coronal mass ejections) that may pass Earth, with the effect that the cosmic ray flux decreases suddenly and stays low for a week or two. Such events, with a significant reduction in the cosmic rays flux, are called Forbush decreases, and can be used to test the link between cosmic ray ionization and clouds. A recent comprehensive study identified the strongest Forbush decreases, ranked them according to strength, and disussed some of the controversies that have surrounded this subject [Svensmark et al., 2016]. Atmospheric data consisted of three independent cloud satellite data sets and one dataset for aerosols. A clear response to the five strongest Forbush decreases was seen in both aerosols and all low cloud data[Svensmark et al., 2016]. The global average response time from the change in ionization to the change in clouds was $\sim$ 7 days [Svensmark et al., 2016], consistent with the above growth rate of $\sim$ 0.4 nm/hour. The five strongest Forbush decreases (with ionization changes comparable to those observed over a solar cycle) exhibited inferred aerosol changes and cloud micro-physics changes of the order $\sim 2\%$ [Svensmark et al., 2016]. The range of ion production in the atmosphere varies between 2-35 ions-pairs s^{-1} cm^{-3}[Bazilevskaya et al., 2008] and from Fig. 4.1b it can be inferred from that a 20% variation in the ion production can impact the growth rate in the range 1-4% (under the pristine conditions). It is suggested that such changes in the growth rate can explain the $\sim 2\%$ changes in clouds and aerosol change observed during Forbush decreases [Svensmark et al., 2016]. It should be stressed that there is not just one effect of CCN on clouds, but that the impact will depend on regional differences and cloud types. In regions with a relative high number of CCN the presented effect will be small, in addition the effect on convective clouds and on ice clouds is expected to be negligible. Additional CCNs can even result in fewer clouds [Koren et al., 2008]. Since the ion condensation effect is largest for low SA concentrations and aerosol densities the impact is believed to be largest in marine stratus clouds.

On astronomical timescales, as the solar system moves through spiral-arms and inter-arm regions of the Galaxy, changes in the cosmic ray flux can be much larger [Shaviv, 2002, 2003, Svensmark, 2012]. Inter-arm regions can have half the present day cosmic ray flux, whereas spiral arm regions should have at least 1.5 times the present day flux. This should correspond to a $\sim$ 10% change in aerosol growth rate, between arm and inter-arm regions. Finally, if a near-Earth supernova occurs, as may have happened between 2-3 million years ago [Knie et al., 2004], the ionization can increase 100 to 1000 fold depending on its distance to Earth and time since event. Figure 4.1b shows that the aerosol growth rate in this case increases by more than 50%. Such large changes should have profound impact on CCN concentrations, the formation of clouds and ultimately climate.

In conclusion, a mechanism by which ions condense their mass onto small aerosols and thereby increase the growth rate of the aerosols, has been formulated theoretically and shown to be in good agreement with extensive experiments. The mechanism of ion-induced condensation may be relevant in the Earth's atmosphere under pristine conditions, and able to influence the formation of cloud condensation nuclei. It is conjectured that this mechanism could be the explanation for the observed correlations between past climate variations and cosmic rays, modulated by either solar activity [Eddy, 1976, Svensmark, 1998, Neff et al., 2001, Bond et al., 2001, Shaviv, 2008] or supernova activity in the solar neighbourhood on very long time scales[Shaviv, 2002, 2003, Svensmark, 2012]. The theory of ion-induced condensation should be incorporated into global aerosol models, to fully test the atmospheric implications.

4.5 Methods

4.5.1 Correction to condensation due to ions

Expanding Eqs. (4.1) gives

$$\begin{aligned}
\frac{\partial N^0}{\partial t} &= -\frac{\partial}{\partial r}\left(A^0 n^0 \beta^{00} N^0 + A^- n^- \beta^{-+} N^+ \right. \\
&\quad \left. + A^+ n^+ \beta^{+-} N^- \right) \\
\frac{\partial N^+}{\partial t} &= -\frac{\partial}{\partial r}\left(A^0 n^0 \beta^{0+} N^+ + A^+ n^+ \beta^{+0} N^0\right) \\
\frac{\partial N^-}{\partial t} &= -\frac{\partial}{\partial r}\left(A^0 n^0 \beta^{0-} N^- + A^- n^- \beta^{-0} N^0\right). \qquad (4.9)
\end{aligned}$$

where the indexes 0,$+$ and $-$ refer to neutral, positively, and negatively charged particles. Here r and t are the radius of the aerosol and the time. N^0, N^+, and N^- is the number density of neutral, positive, and negative aerosols. n^0 is the concentration of the condensible gas (usually sulfuric acid in the gas phase), n^+ and n^- are the concentration of positive and negative ions, $A^0 = (m^0/4\pi r^2\rho)$, $A^+ = (m^+/4\pi r^2\rho)$, and $A^- = (m^-/4\pi r^2\rho)$, where m^0 is the mass of the neutral gas molecule, m^+ and m^- are the average mass of positive/negative ions, ρ is the mass density of condensing gas, and β the interaction coefficient between the monomers and the neutral and/or charged aerosols. The parameters of the above model are shown in Fig. (4.5).

Using equilibrium between aerosols and ions we have

$$\frac{N^+}{N^0} \approx \frac{n^+\beta^{+0}}{n^-\beta^{-+}}, \qquad \frac{N^-}{N^0} \approx \frac{n^-\beta^{-0}}{n^+\beta^{+-}}, \tag{4.10}$$

while defining $N^{tot} = N^0 + N^+ + N^-$ gives

$$\frac{N^0(r,t)}{N^{tot}(r,t)} = \left[1 + \frac{n^+\beta^{+0}}{n^-\beta^{-+}} + \frac{n^-\beta^{-0}}{n^+\beta^{+-}}\right]^{-1}. \tag{4.11}$$

If we further assume symmetry between the positive and negative charges, i.e. that $m_{\rm ion} \equiv m^+ = m^-$, $\beta^{\pm 0} \equiv \beta^{-0} = \beta^{+0}$, $\beta^{\pm\mp} \equiv \beta^{+-} = \beta^{-+}$ as well as $n_{ion} \equiv n^+ = n^-$, such that $A^\pm \equiv A^+ = A^-$, we find

$$\frac{N^\pm}{N^0} = \frac{\beta^{\pm 0}}{\beta^{\mp\pm}}, \tag{4.12}$$

and for $N^{tot} = N^0 + N^+ + N^-$, we obtain

$$\frac{N^0(r,t)}{N^{tot}(r,t)} = \left[1 + 2\frac{\beta^{\pm 0}}{\beta^{\mp\pm}}\right]^{-1}. \tag{4.13}$$

Using Eqs. (4.12) in Eq. (4.9) and using the charge symmetry gives

$$\begin{aligned}
\frac{\partial N^0}{\partial t} &= -\frac{\partial}{\partial r}([A^0 n^0 \beta^{00} + 2A^\pm n_{ion}\beta^{\pm 0}]N^0) \\
\frac{\partial N^+}{\partial t} &= -\frac{\partial}{\partial r}([A^0 n^0 \beta^{0\pm}\frac{\beta^{\pm 0}}{\beta^{\mp\pm}} + A^\pm n_{ion}\beta^{\pm 0}]N^0) \\
\frac{\partial N^-}{\partial t} &= -\frac{\partial}{\partial r}([A^0 n^0 \beta^{0\pm}\frac{\beta^{\pm 0}}{\beta^{\mp\pm}} + A^\pm n_{ion}\beta^{\pm 0}]N^0).
\end{aligned}$$

Adding the three equations then results in

$$\frac{\partial N^{\rm tot}}{\partial t} = -\frac{\partial}{\partial r}\left(\left[A^0 n^0(\beta^{00} + 2\beta^{0\pm}\frac{\beta^{\pm 0}}{\beta^{\mp\pm}}) \;\; + 4A^\pm n_{ion}\beta^{\pm 0}\right] N^0\right).$$

Using N^{tot} as a common factor, we then have

$$\frac{\partial N^{\rm tot}}{\partial t} = -\frac{\partial}{\partial r}\left(\left[A^0 n^0(\beta^{00} + 2\beta^{0\pm}\frac{\beta^{\pm 0}}{\beta^{\mp\pm}})\frac{N^0}{N^{\rm tot}} \;\; + 4A^\pm n_{ion}\beta^{\pm 0}\frac{N^0}{N^{\rm tot}}\right] N^{\rm tot}\right)$$

Taking β^{00} as a common factor and plugging Eq. (4.13) into the first term gives the expression

$$F = \frac{(1 + 2\beta^{0\pm}\beta^{\pm 0}/(\beta^{\mp\pm}\beta^{00}))}{[1 + 2\beta^{\pm 0}/\beta^{\mp\pm}]} \tag{4.14}$$

The above function is equal to $1+\mathcal{O}(10^{-2})$, and F is therefore replaced with 1. A simple rearrangement provides the final form

$$\frac{\partial N^{\rm tot}(r,t)}{\partial t} = -\frac{\partial}{\partial r}\left[A_0 n^0 \beta^{00}\,(1+\Gamma)\,N^{\rm tot}(r,t)\right], \tag{4.15}$$

where

$$\Gamma = 4\left(\frac{n_{\mathrm{ion}}}{n_{\mathrm{sa}}}\right)\left(\frac{\beta^{\pm 0}}{\beta^{00}}\right)\left(\frac{m_{\mathrm{ion}}}{m^{0}}\right)\left(\frac{N^{0}(r,t)}{N^{\mathrm{tot}}(r,t)}\right). \tag{4.16}$$

4.5.2 Detailed description of the experimental setup

The experiments were conducted in a cubic 8 m^3 stainless steel reaction chamber used in Svensmark et al 2013 [Svensmark et al., 2013], and shown schematically in Fig. 4.6. One side of the chamber is made of Teflon foil to allow the transmission of collimated UV light (253.7 nm), that was used for photolysis of ozone to generate sulfuric acid that initiates aerosol nucleation. The chamber was continuously flushed with 20 L/min of purified air passing through a humidifier, 5 L/min of purified air passing through an ozone generator, and 3.5 mL/min of SO_2 (5 ppm in air, AGA). The purified air was supplied by a compressor with a drying unit and a filter with active charcoal and citric acid. The chamber was equipped with

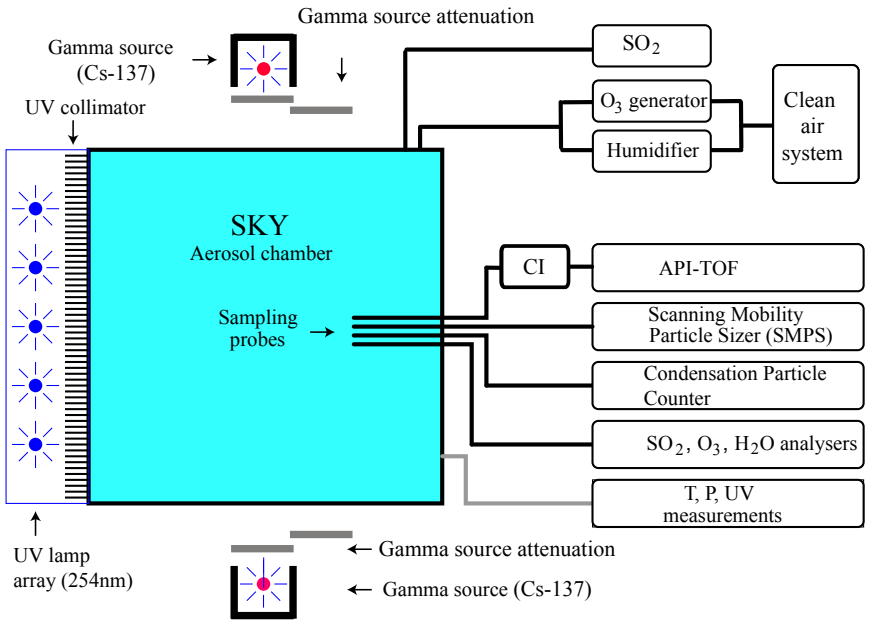

Figure 4.6: The Experimental Setup.

gas analyzers for ozone and sulfur dioxide (a Teledyne 400 and Thermo 43 CTL, respectively) and sensors for temperature and relative humidity. For aerosol measurements, a scanning mobility particle sizing (SMPS) system was used. The system consisted of an electrostatic classifier (TSI model 3080 with a model 3077A Kr-85 neutralizer) using a nano-DMA (TSI model 3085) along with either one of two condensation particle counters (TSI model 3775 or 3776). For some of the experiments, a CI API-ToF [Jokinen et al., 2012] using HNO_3 as the ionizing agent was used to measure the sulfuric acid in the chamber. The ionization in the chamber could be increased by two 27 MBq Cs-137 gamma sources placed 0.6 metres from opposing sides of the chamber, with the option of putting attenuating lead plates of 0.5, 1.0, and 2.0 cm thickness in front of each source. At full strength the sources increase the ionization in the chamber to 212 ion-pairs cm^{-3} s^{-1}.

4.5.3 Details of the data analysis

A total of 11 experimental runs totalling 3100 hours of measurements were made with varying settings. The settings for each of the experiments are shown in Table 4.1.

To detect an eventual difference in growth rate the following method was employed. For each experimental run each size-bin was normalized and then the individual periods were superposed to reduce the noise in the data, as shown in Fig. 4.2 of the main paper. The superposed data was then used for further analysis. For each size-bin recorded by the SMPS, the number of aerosols relative to the mean number ($\langle N(d)\rangle = 1/T \int_0^T N^{\mathrm{tot}}(d,t')dt'$) was then plotted - as exemplified in the top curve of Fig. 4.7. The derivative of this curve, is the rate of change of aerosol density of a given size, is used to determine the temporal position of the profiles 1 and 2. This can be achieved by first calculating the derivative ($(d(N^{\mathrm{tot}}/\langle N(d)\rangle)/dt)^2$), then normalizing with this function's maximum value at diameter d, (the square was used to get a positive definite and sharply defined profile), and then smoothed using a boxcar filter with a width of typically 7 to 16 minutes - shown as the lower black curve in Fig. 4.7. The width of the boxcar filter was typically determined from the requirement that the Gaussian fit converged - for instance, in some cases with low sulphuric acid concentration a longer boxcar filter was used, due to the relatively higher noise. On top of the black curve in Fig. 4.7, a dashed red and a dashed blue curve are superimposed. These are Gaussian fits to the two maxima. The position of the center of each of the Gaussian profiles gives the growth time relative to the time the γ sources were opened (profile 1) or closed (profile 2). Figure 4.8 plots $(d(N^{\mathrm{tot}}/\langle N(d)\rangle)/dt)^2$, normalized with this functions maximum value at diameter d, in the (d,t)-plane. The position of the maxima are easily seen. The black dashed and red curves in Fig. 4.8 are the maxima obtained from the Gaussian fits of profile 1 and profile 2. The difference between these growth times then gives the ΔT for each bin size, as shown in Fig. 4.3. The ΔT values can then be compared with the theoretical expectations. Averaging the individual ΔT values for sizes between 6 and 12 nm finally results in the ΔT shown in Fig. 4.4.

4.5.4 The m_{ion}/m_0 ratio

Table 4.2 summarizes the average masses (m/q) of a series of runs using the API-ToF without the CI-unit to measure negative ions in order to determine the ratio m_{ion}/m_0. Note that water evaporates in the API-ToF so the masses measured are lower than the actual masses of the clusters. The ratio of 2.25 for m_{ion}/m_0 used in the calculations would imply that for a dry (0 water) neutral sulfuric acid molecule (98 amu) m_{ion} should be 220 m/q. The amount of water on a sulfuric acid molecule varies according to relative humidity - for 50 % RH it is typically 1-2 water molecules. Assuming 1.5 waters and m_{ion}/m_0=2.25 this would give a wet mass of 281 amu. However, the experiments were performed at lower RH than 50 % and also note that hydrogen sulfate ions attract more water than the neutral sulfuric acid molecule [Kurtén et al., 2007]. Last, the positive ions were not measured and these are typically heavier than the negative ions [Hõrrak et al., 1998].

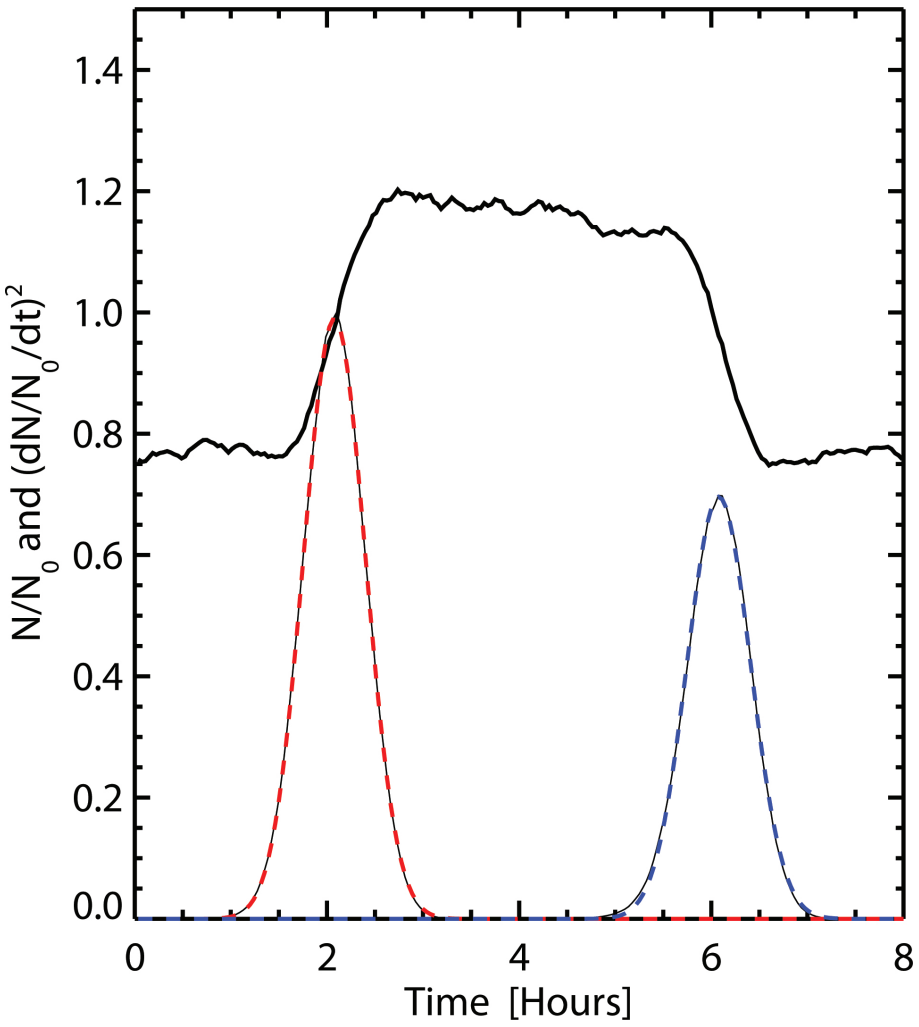

Figure 4.7: Superposed data and gaussian fits using the data from experiment V9 and SMPS size-bins centered on d = 7.51 nm.

4.5.5 Acknowledgements

Jacob Svensmark is funded by the Danish council for independent research under the project "Fundamentals of Dark Matter Structures", DFF 6108-00470. HS thanks the late Nigel Calder for many discussions in the early part of this work.

4.6 Tables

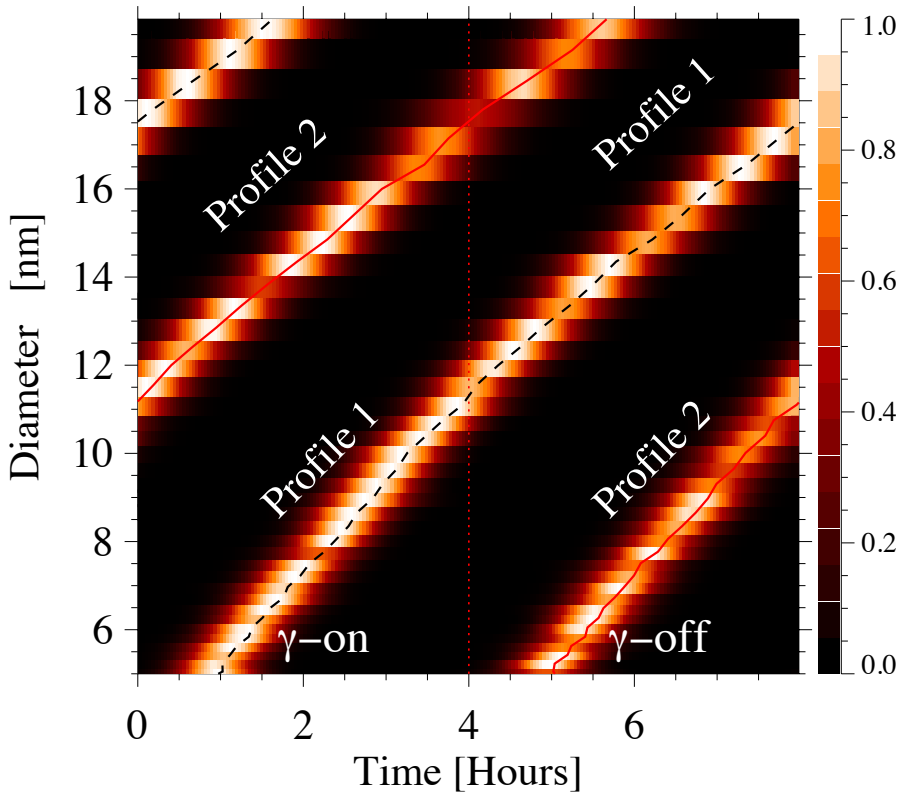

Figure 4.8: Example of $(d(N^{\mathrm{tot}}(d,t)/\langle N(d)\rangle)/dt)^2$, normalized with this functions maximum value at diameter d, in the (d,t)-plane. From experiment V9. The black dashed line and red lines are the maximum values, found from a Gaussian fit, and determine the evolution of the profiles 1 and 2.

Exp.*	P†	N‡	Scan range**	UV††	RH‡‡	CPC♠	Lead♣
-	hours	#	nm	%	%	Model	cm
V1*	4	23	3.5-118	80	14	3775	0
V2*	4	97	2-63.8	70	23	3776	0
V3*	8	16	2-63.8	70	23	3776	0
V4*	4	77	2-63.8	50	23	3776	0
V5*	8	44	2-63.8	40	15	3775	0
V6	8	22	2-63.8	35	21	3775	0
V7	8	4	4.0-20.2	35	37	3775	0
V8	8	12	4.0-20.2	25	38	3775	0
V9	8	45	4.0-20.2	15	38	3775	0
V10	8	47	4.0-20.2	15	38	3775	1
V11	8	99	4.0-20.2	25	37	3775	1

Table 4.1: Overview of experimental runs. *) shows the name of the experiment, used for reference. An asterisk (*) next to the name indicates that sulfuric acid was measured during the experiment. †) is the length of the period (P) where a P of 4 hours means that the experiment had 2 hours of γ-rays on and 2 hours of γ-rays off. ‡) is the number of repetitions (periods) of the experiment. **) is the scan range of the DMA, which was narrowed in later runs without changing the scan-time to improve counting statistics. ††) is the setting of the UV light used to produce sulfuric acid, in percentage of maximum power. ‡‡) shows the relative humidity in the chamber. ♠) shows the TSI model number of the CPC used. ♣) shows the amount of lead in front of the gamma sources during the gamma-on time.

UV	Gamma	Mass	Mass w. water
%	-	m/q	m/q
0	off	258	280
25	off	177	214
25	on	174	209
50	off	189	227
70	off	183	220
70	on	175	212

Table 4.2: Average mass spectra. Each line shows the conditions and average m/q for a 4-hour API-ToF mass spectrum without the CI. Column 1 shows the UV level as percentage of maximum power. Column 2 shows whether the γ-ray sources were on or off. Column 3 is the average m/q of the spectrum. Column 4 is the average mass of the spectrum, when 1 water (m/q 18) has been added to all masses except the first four sulfuric acid peaks (m/q 97, 195, 293, 391) which has 1.5 water per sulfuric acid.

Bibliography

G. A. Bazilevskaya, I. G. Usoskin, E. O. Flückiger, R. G. Harrison, L. Desorgher, R. Bütikofer, M. B. Krainev, V. S. Makhmutov, Y. I. Stozhkov, A. K. Svirzhevskaya, N. S. Svirzhevsky, and G. A. Kovaltsov. Cosmic Ray Induced Ion Production in the Atmosphere. *Space Science Reviews*, 137:149–173, June 2008. doi: 10.1007/s11214-008-9339-y.

G. Bond, B. Kromer, J. Beer, R. Muscheler, M. N. Evans, W. Showers, S. Hoffmann, R. Lotti-Bond, I. Hajdas, and G. Bonani. Persistent Solar Influence on North Atlantic Climate During the Holocene. *Science*, 294:2130–2136, December 2001. doi: 10.1126/science.1065680.

O. Boucher et. al. *Clouds and Aerosols*, book section 7, pages 571–657. Cambridge University Press, 2013. ISBN ISBN 978-1-107-66182-0. doi: 10.1017/CBO9781107415324.018. URL `www.climatechange2013.org`.

A. D. Clarke, F. Eisele, V. N. Kapustin, K. Moore, D. Tanner, L. Mauldin, M. Litchy, B. Lienert, M. A. Carroll, and G. Albercook. Nucleation in the equatorial free troposphere: Favorable environments during pem-tropics. *Journal of Geophysical Research: Atmospheres*, 104(D5): 5735–5744, 1999. ISSN 2156-2202. doi: 10.1029/98JD02303. URL `http://dx.doi.org/10.1029/98JD02303`.

A. D. Clarke, S. Freitag, R. M. C. Simpson, J. G. Hudson, S. G. Howell, V. L. Brekhovskikh, T. Campos, V. N. Kapustin, and J. Zhou. Free troposphere as a major source of ccn for the equatorial pacific boundary layer: long-range transport and teleconnections. *Atmospheric Chemistry and Physics*, 13(15):7511–7529, 2013. doi: 10.5194/acp-13-7511-2013. URL `https://www.atmos-chem-phys.net/13/7511/2013/`.

Frédéric Clette, Leif Svalgaard, JoséM. Vaquero, and Edward W. Cliver. Revisiting the sunspot number. *Space Science Reviews*, 186(1):35–103, 2014. doi: 10.1007/s11214-014-0074-2.

Robert E. Dickinson. Solar variability and the lower atmosphere. *Bulletin American Meteorological Society*, 56(12):1240–1248, 1975.

Eimear M. Dunne, Hamish Gordon, Andreas Kürten, João Almeida, Jonathan Duplissy, Christina Williamson, Ismael K. Ortega, Kirsty J. Pringle, Alexey Adamov, Urs Baltensperger, Peter Barmet, Francois Benduhn, Federico Bianchi, Martin Breitenlechner, Antony Clarke, Joachim Curtius, Josef Dommen, Neil M. Donahue, Sebastian Ehrhart, Richard C. Flagan, Alessandro Franchin, Roberto Guida, Jani Hakala, Armin Hansel, Martin Heinritzi, Tuija Jokinen, Juha Kangasluoma, Jasper Kirkby, Markku Kulmala, Agnieszka Kupc, Michael J. Lawler, Katrianne Lehtipalo, Vladimir Makhmutov, Graham Mann, Serge

Mathot, Joonas Merikanto, Pasi Miettinen, Athanasios Nenes, Antti Onnela, Alexandru Rap, Carly L. S. Reddington, Francesco Riccobono, Nigel A. D. Richards, Matti P. Rissanen, Linda Rondo, Nina Sarnela, Siegfried Schobesberger, Kamalika Sengupta, Mario Simon, Mikko Sipilä, James N. Smith, Yuri Stozkhov, Antonio Tomé, Jasmin Tröstl, Paul E. Wagner, Daniela Wimmer, Paul M. Winkler, Douglas R. Worsnop, and Kenneth S. Carslaw. Global atmospheric particle formation from cern cloud measurements. *Science*, 354(6316):1119–1124, 2016. ISSN 0036-8075. doi: 10.1126/science.aaf2649. URL `http://science.sciencemag.org/content/354/6316/1119`.

J. Duplissy, M. B. Enghoff, K. L. Aplin, F. Arnold, H. Aufmhoff, M. Avngaard, U. Baltensperger, T. Bondo, R. Bingham, K. Carslaw, J. Curtius, A. David, B. Fastrup, S. Gagné, F. Hahn, R. G. Harrison, B. Kellett, J. Kirkby, M. Kulmala, L. Laakso, A. Laaksonen, E. Lillestol, M. Lockwood, J. Mäkelä, V. Makhmutov, N. D. Marsh, T. Nieminen, A. Onnela, E. Pedersen, J. O. P. Pedersen, J. Polny, U. Reichl, J. H. Seinfeld, M. Sipilä, Y. Stozhkov, F. Stratmann, H. Svensmark, J. Svensmark, R. Veenhof, B. Verheggen, Y. Viisanen, P. E. Wagner, G. Wehrle, E. Weingartner, H. Wex, M. Wilhelmsson, and P. M. Winkler. Results from the CERN pilot CLOUD experiment. *Atmospheric Chemistry & Physics*, 10(4):1635–1647, February 2010.

J. A. Eddy. The Maunder Minimum. *Science*, 192:1189–1202, June 1976.

H. Gerdien. Demonstration eines apparates zur absoluten messung der elektrischen leitfahigheit der luft. *Phys. Zeitung*, 6:800–801, 1905.

William A. Hoppel. Ion-aerosol attachment coefficients, ion depletion, and the charge distribution on aerosols. *Journal of Geophysical Research: Atmospheres*, 90(D4):5917–5923, 1985. doi: 10.1029/JD090iD04p05917. URL `https://agupubs.onlinelibrary.wiley.com/doi/abs/10.1029/JD090iD04p05917`.

U. Hõrrak, J. Salm, and H. Tammet. Bursts of intermediate ions in atmospheric air. *Journal of Geophysical Research: Atmospheres*, 103(D12):13909–13915, 1998. doi: 10.1029/97JD01570.

T. Jokinen, M. Sipilä, H. Junninen, M. Ehn, G. Lönn, J. Hakala, T. Petäjä, R. L. Mauldin III, M. Kulmala, and D. R. Worsnop. Atmospheric sulphuric acid and neutral cluster measurements using ci-api-tof. *Atmospheric Chemistry and Physics*, 12(9):4117–4125, 2012. doi: 10.5194/acp-12-4117-2012. URL `https://www.atmos-chem-phys.net/12/4117/2012/`.

Eigil Kaas, Patrick Bülov, and Jacob Svensmark. Using varying ERA-I reforecast errors to study a possible link between cloud cover and galactic cosmic rays. In *EGU General Assembly Conference Abstracts*, EGU General Assembly Conference Abstracts, page 16996, April 2019.

J. Kirkby, J. Curtius, J. Almeida, E. Dunne, J. Duplissy, S. Ehrhart, A. Franchin, S. Gagne, L. Ickes, A. Kurten, A. Kupc, A. Metzger, F. Riccobono, L. Rondo, S. Schobesberger, G. Tsagkogeorgas, D. Wimmer, A. Amorim, F. Bianchi, M. Breitenlechner, A. David, J. Dommen, A. Downard, M. Ehn, R. C. Flagan, S. Haider, A. Hansel, D. Hauser, W. Jud, H. Junninen, F. Kreissl, A. Kvashin, A. Laaksonen, K. Lehtipalo, J. Lima, E. R. Lovejoy, V. Makhmutov, S. Mathot, J. Mikkila, P. Minginette, S. Mogo, T. Nieminen, A. Onnela, P. Pereira, T. Petaja, R. Schnitzhofer, J. H. Seinfeld, M. Sipila, Y. Stozhkov, F. Stratmann, A. Tome, J. Vanhanen, Y. Viisanen, A. Vrtala, P. E. Wagner, H. Walther, E. Weingartner, H. Wex, P. M. Winkler, K. S.

Carslaw, D. R. Worsnop, U. Baltensperger, and M. Kulmala. Role of sulphuric acid, ammonia and galactic cosmic rays in atmospheric aerosol nucleation. *Nature*, 476:429–433, August 2011. doi: 10.1038/nature10343.

Jasper Kirkby. Cosmic Rays and Climate. *Surveys in Geophysics*, 28(5-6):333–375, November 2007. doi: 10.1007/s10712-008-9030-6.

K. Knie, G. Korschinek, T. Faestermann, E. A. Dorfi, G. Rugel, and A. Wallner. ^{60}Fe anomaly in a deep-sea manganese crust and implications for a nearby supernova source. *Phys. Rev. Lett.*, 93:171103, 10 2004. doi: 10.1103/PhysRevLett.93.171103. URL `http://link.aps.org/doi/10.1103/PhysRevLett.93.171103`.

Ilan Koren, J. Vanderlei Martins, Lorraine A. Remer, and Hila Afargan. Smoke invigoration versus inhibition of clouds over the amazon. *Science*, 321(5891):946–949, 2008. ISSN 0036-8075. doi: 10.1126/science.1159185. URL `http://science.sciencemag.org/content/321/5891/946`.

C. Kuang, P. H. McMurry, and A. V. McCormick. Determination of cloud condensation nuclei production from measured new particle formation events. *Geophysical Research Letters*, 36(9):n/a–n/a, 2009. ISSN 1944-8007. doi: 10.1029/2009GL037584. URL `http://dx.doi.org/10.1029/2009GL037584`. L09822.

Theo Kurtén, Madis Noppel, Hanna Vehkamäki, Martta Salonen, and Markku Kulmala. Quantum chemical studies of hydrate formation of h_2so_4 and hso_4^-. *Boreal Environment Research*, 12:431–453, 2007.

L Laakso, T. Petäjä, K. E. J. Lehtinen, M. Kulmala, J. Paatero, U. Hõrrak, H. Tammet, and J. Joutsensaari. Ion production rate in a boreal forest based on ion particle and radiation measurements. *Atmosperic Chemistry and Physics*, 4:1933–1943, 2004.

L. Laakso, S. Gagné, T. Petäjä, A. Hirsikko, P. P. Aalto, M. Kulmala, and V.-M. Kerminen. Detecting charging state of ultra-fine particles: instrumental development and ambient measurements. *Atmospheric Chemistry and Physics*, 7:1333–1345, 2007.

A. A. Lushnikov and M. Kulmala. Charging of aerosol particles in the near free-molecule regime. *The European Physical Journal D - Atomic, Molecular, Optical and Plasma Physics*, 29(3):345–355, 2004. ISSN 1434-6079. doi: 10.1140/epjd/e2004-00047-9. URL `http://dx.doi.org/10.1140/epjd/e2004-00047-9`.

Alexey B. Nadykto and Fangqun Yu. Uptake of neutral polar vapor molecules by charged clusters/particles: Enhancement due to dipole-charge interaction. *Journal of Geophysical Research: Atmospheres*, 108(D23):n/a–n/a, 2003. ISSN 2156-2202. doi: 10.1029/2003JD003664. URL `http://dx.doi.org/10.1029/2003JD003664`. 4717.

U. Neff, S. J. Burns, A. Mangini, M. Mudelsee, D. Fleitmann, and A. Matter. Strong coherence between solar variability and the monsoon in Oman between 9 and 6kyr ago. *Nature*, 411:290–293, May 2001.

J. R. Pierce and P. J. Adams. Can cosmic rays affect cloud condensation nuclei by altering new particle formation rates? *Geophysical Research Letters*, 36:L09820, May 2009. doi: 10.1029/2009GL037946.

J. H. Seinfeld and S. N. Pandis. *Atmospheric Chemistry and Physics: From Air Pollution to Climate Change*. John Wiley & Sons, Inc., 2nd edition, 2006. ISBN 0-471-72018-6.

John H. Seinfeld and Spyros N. Pandis. *Atmospheric Chemistry and Physics: From Air Pollution to Climate Change*. John Wiley and Sons, 1998.

N. J. Shaviv. Cosmic Ray Diffusion from the Galactic Spiral Arms, Iron Meteorites, and a Possible Climatic Connection. *Phys. Rev. Lett.*, 89(5):051102–+, 2002. doi: 10.1103/PhysRevLett.89.051102.

N. J. Shaviv. The spiral structure of the Milky Way, cosmic rays, and ice age epochs on Earth. *New Astronomy*, 8:39–77, January 2003. doi: 10.1016/S1384-1076(02)00193-8.

N. J. Shaviv. Using the oceans as a calorimeter to quantify the solar radiative forcing. *Journal of Geophysical Research (Space Physics)*, 113(A12):A11101, November 2008. doi: 10.1029/2007JA012989.

E. J. Snow-Kropla, J. R. Pierce, D. M. Westervelt, and W. Trivitayanurak. Cosmic rays, aerosol formation and cloud-condensation nuclei: sensitivities to model uncertainties. *Atmospheric Chemistry and Physics*, 11(8):4001–4013, 2011. doi: 10.5194/acp-11-4001-2011. URL `https://www.atmos-chem-phys.net/11/4001/2011/`.

H. Svensmark. Evidence of nearby supernovae affecting life on Earth. *Monthly Notices of the Royal Astronomical Society*, 423:1234–1253, June 2012. doi: 10.1111/j.1365-2966.2012.20953.x.

H. Svensmark and E. Friis-Christensen. Variation of cosmic ray flux and global cloud coverage - a missing link in solar-climate relationships. *Journal of Atmospheric and Solar-Terrestrial Physics*, 59(11):1225–1232, July 1997.

H. Svensmark, J. O. P. Pedersen, N. D. Marsh, M. B. Enghoff, and U. I. Uggerhøj. Experimental evidence for the role of ions in particle nucleation under atmospheric conditions. *Proceedings of the Royal Society of London Series A*, 463:385–396, 02 2007. doi: 10.1098/rspa.2006.1773.

H. Svensmark, T. Bondo, and J. Svensmark. Cosmic ray decreases affect atmospheric aerosols and clouds. *Geophysical Research Letters*, 36:L15101, August 2009. doi: 10.1029/2009GL038429.

Henrik Svensmark. Influence of cosmic rays on earth's climate. *Phys. Rev. Lett.*, 81:5027–5030, 11 1998. doi: 10.1103/PhysRevLett.81.5027. URL `http://link.aps.org/doi/10.1103/PhysRevLett.81.5027`.

Henrik Svensmark, Martin B. Enghoff, and Jens Olaf Pepke Pedersen. Response of cloud condensation nuclei (>50 nm) to changes in ion-nucleation. *Physics Letters A*, 377(37):2343 – 2347, 2013. ISSN 0375-9601. doi: http://dx.doi.org/10.1016/j.physleta.2013.07.004. URL `http://www.sciencedirect.com/science/article/pii/S0375960113006294`.

J. Svensmark, M. B. Enghoff, N. J. Shaviv, and H. Svensmark. The response of clouds and aerosols to cosmic ray decreases. *Journal of Geophysical Research (Space Physics)*, 121:8152–8181, 09 2016. doi: 10.1002/2016JA022689.

S. Twomey, R. Gall, and M. Leuthold. Pollution and cloud reflectance. *Boundary-Layer Meteorology*, 41(1):335–348, 12 1987. ISSN 1573-1472. doi: 10.1007/BF00120449. URL https://doi.org/10.1007/BF00120449.

F. Yu and R. P. Turco. The formation and evolution of aerosols in stratospheric aircraft plumes: Numerical simulations and comparisons with observations. *Journal of Geophysical Research: Atmospheres*, 103:25915–25934, 1998. doi: 10.1029/98JD02453.

Fangqun Yu and Gan Luo. Effect of solar variations on particle formation and cloud condensation nuclei. *Environmental Research Letters*, 9(4):045004, 2014. URL http://stacks.iop.org/1748-9326/9/i=4/a=045004.

Fangqun Yu and Richard P. Turco. From molecular clusters to nanoparticles: Role of ambient ionization in tropospheric aerosol formation. *Journal of Geophysical Research: Atmospheres*, 106(D5):4797–4814, 2001. ISSN 2156-2202. doi: 10.1029/2000JD900539. URL http://dx.doi.org/10.1029/2000JD900539.

5

Ion-induced condensation: Numerical Model

The Ion and Charged Aerosol Growth Enhancement (ION-CAGE) code: A numerical model for the growth of charged and neutral aerosols

Earth and Space Science, July 2020, DOI 10.1029/2020EA001142

Jacob Svensmark[1,2], **Nir J. Shaviv**[3], **Martin B. Enghoff**[2], **Henrik Svensmark**[2]

[1] Dark Cosmology Centre, Niels Bohr Institute, University of Copenhagen, Juliane Maries Vej 30, 2100 Copenhagen, Denmark.

[1] National Space Institute, Technical University of Denmark, Elektrovej, Building 328, 2800 Lyngby, Denmark.

[3] Racah Institute of Physics, Hebrew University of Jerusalem, Jerusalem 91904, Israel.

Abstract

The presence of small ions influences the growth dynamics of a size distribution of aerosols. Specifically, the often neglected mass of small ions influences the aerosol growth rate, which may be important for terrestrial cloud formation. To this end, we develop the Ion and Charged Aerosol Growth Enhancement (ION-CAGE) code, a numerical model to calculate the growth of a species of aerosols in the presence of charge, which explicitly includes terms for ion condensation. It is shown that a positive contribution to aerosol growth rate is obtained by increasing the ion-pair concentration through this ion condensation effect, consistent with recent experimental findings. The ion condensation effect is then compared to aerosol growth from charged aerosol coagulation, which is seen to be independent of ion-pair concentration. Growth rate enhancements by ion condensation are largest for aerosol sizes less than $\sim$25 nm and increases proportional to the ion concentration. The effect of ion condensation is expected to be most important over pristine marine areas. The model source code is made available through a public repository.

5.1 Introduction

There is no shortage of numerical models aimed at describing the production, growth and transport of aerosols for a broad range of parameters, environments and applications. Often the scenarios that these models describe turn out very demanding from a computational point of view. Thus, as with any model, a number of optimizations and compromises must be made in terms of included effects and mechanisms, dimensionality, resolution, etc. Recent advances in our understanding of the interplay between atmospheric aerosols and electrical charge has heightened the need for aerosol growth modeling that takes charge into account in a detailed way, as charge seems to act as an enhancing agent for aerosol growth rate under atmospheric conditions relevant for marine aerosols [Svensmark et al., 2017, hereafter "SESS17 paper"]. In order to conduct tests of theoretical assumptions, or design and understand future experimental efforts in which charged aerosols are present, a complementary simple, modifiable, open-source numerical model can be helpful. Several advanced models describing aerosol dynamics have been developed, e.g., Pierce and Adams [2009], Yu and Turco [2001], Laakso et al. [2002], Kazil and Lovejoy [2004], Leppä et al. [2009], McGrath et al. [2012]. While some of these models take the charge of aerosols into account, none so far study the mechanism of ion-induced condensation, i.e. the accelerated growth caused by the mass of ions. Leppä et al. [2009] includes charge but does not explicitly model the condensation of ions onto aerosols, and the code is not freely available. Others, such as Prakash et al. [2003] are open-source, however do not include charge at all.

In the present work we introduce the Ion and Charged Aerosol Growth Enhancement (ION-CAGE) model: A zero-dimensional box model capable of solving the general dynamics equation (GDE) numerically for both single-charged and neutral aerosol species. Uniquely this model includes terms considering the addition of the non-zero mass of ions upon interactions with aerosols. It is coded in a way that allows for the easy in- or exclusion of a selection of the usual GDE terms, as well as code structure that can easily be modified to include new terms where desired. For this work the model is set up to simulate the growth of sulfuric acid aerosols in an environment corresponding to clean marine air, as relevant for the SESS17 experiment. The numerical solutions involving ion accelerated growth of aerosols demonstrate excellent agreement with the SESS17 theoretical results. To further test the theory, it would be useful to incorporate it into more advanced models, like those mentioned above. However, the results presented here already makes it feasible to test the SESS17 theory in computationally heavy global circulation models.

In the following sections we present the terms of the GDE that are included in the model and demonstrate that it operates in correspondence with expectations. We apply the model by reproducing and expanding on the results of the SESS17 paper, by probing the growth rate of aerosols exposed to varying concentrations of ions-pairs and aerosols, considering also aerosol coagulation.

5.2 Model overview

The ION-CAGE model considers the temporal evolution of number concentrations for the following species: Neutral and charged small stable and condensable molecular clusters (henceforth "neutral clusters" and "ions" respectively) and neutral as well as singly charged aerosols of both signs. Ions and neutral clusters are set at a certain diameter and number density, whereas the aerosols exist at a number N_{tot} of logarithmically spaced nodes in volume as indicated by the index $k \in [1, N_{\mathrm{tot}}]$. This helps the model span the several orders of magnitude in volume that corresponds to aerosol diameters of typically between 1 nm and 100 nm. Given a set of initial conditions for a distribution of neutral clusters, ions, and aerosols along all volume nodes, as well as interaction coefficients, production and loss parameters and other relevant inputs (see below for all parameters), the initial distribution is propagated through forward integration of the GDE using a 4th order Runge-Kutta algorithm [Fehlberg, 1969, Shampine et al., 1976]. As shall be explored below, the GDE contains terms describing the nucleation of new aerosols, the condensation of neutral clusters and ions onto the aerosols, the coagulation of two aerosols into a single larger aerosol and production and loss terms all while keeping track of the exchange of charge between all species, except between neutral clusters and ions. Importantly the mass of the ion can be taken into account such that its small but important contribution to the condensation term is included. The model is written in the FORTRAN language, and its source code is downloadable from a public repository at `https://github.com/jacobsvensmark/ioncage`.

5.2.1 Size nodes

To create a set of N_{tot} volume nodes v_k distributed linearly in logarithmic space between two volumes v_{min} and v_{max}, we use the following

$$v_k = 10^{\log(v_{\mathrm{min}}) + \frac{k-1}{N_{\mathrm{tot}}-1}(\log(v_{\mathrm{max}}) - \log(v_{\mathrm{min}}))}, \tag{5.1}$$

where k is an integer between 1 and N_{tot}. In this way two neighboring nodes are separated by a factor C such that $v_k = C v_{k-1}$. Aerosols in the model have a charge of $q = [0, -, +]$, i.e., 0, -1 or 1 elementary charge. The concentration of aerosols at volume v_k and charge q is denoted N_k^q, and thus the model keeps track of $3N_{\mathrm{tot}}$ aerosol concentrations. A diagram of the node structure can be seen in Figure 5.1. Additionally the model has neutral condensable clusters at concentration n^0, as well as condensable positive and negative ions at concentrations n^+ and n^-, all of which we refer to as monomers. These concentrations constitute the state of the model, and following a set of terms that make up the GDE of this model, the state is propagated forward in time. The terms that govern the dynamics of this process are presented in the next section.

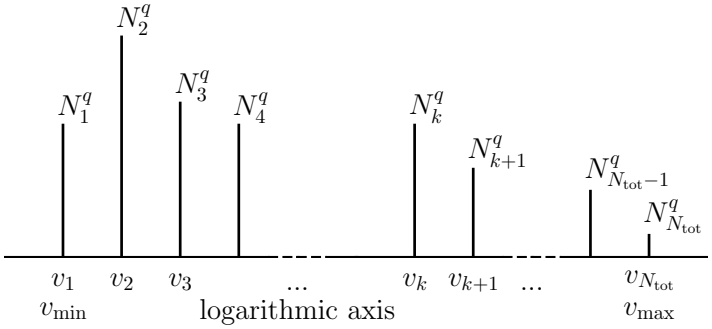

Figure 5.1: Overview of the node structure of the volume bins, and the concentrations at each node for a given charge q. Note that the scale is logarithmic, that each node is a factor of C larger than its smaller neighbor: $v_k = Cv_{k-1}$.

5.3 Interactions

In the following we formulate the interactions governing the temporal derivatives between charged and neutral aerosols, ions and neutral condensable clusters.

A diagram showing the condensation and coagulation rules can be seen in 5.2. Since the sizes of the aerosols of interest are typically in the range 1 - 100 nm, only singly charged aerosols are considered. In depth discussions on the information presented here can be found in e.g. Seigneur et al. [1986], Zhang et al. [1999], Seinfeld and Pandis [2006].

The overall dynamical equations for aerosols at charge $q = [0, -, +]$ are

$$\frac{dN_k^q}{dt} = \frac{dN_k^q}{dt}\Big]_{\mathrm{nucleation}} + \frac{dN_k^q}{dt}\Big]_{\mathrm{condensation}} + \frac{dN_k^q}{dt}\Big]_{\mathrm{coagulation}} + \frac{dN_k^q}{dt}\Big]_{\mathrm{loss}}. \tag{5.2}$$

The first term on the right hand side of Equation 5.2 contains a simple contribution to the nucleation of new aerosol particles of charge $q = [0, -, +]$. The second contains the condensation of neutral clusters and ion mass onto aerosols, while keeping track of the charge of the aerosols in this process. The third term is the most computationally expensive term and describes the coagulation of two aerosols into a larger common aerosol, again taking charge into account. The fourth and final term adds losses in the form of scavenging by large particles and losses to walls required for modelling an experimental situation.

Similarly for the neutral cluster and ion concentrations n^q the terms of the overall GDE are

$$\frac{dn^q}{dt} = \frac{dn^q}{dt}\Big]_{\mathrm{nucleation}} + \frac{dn^q}{dt}\Big]_{\mathrm{condensation}} + \frac{dn^q}{dt}\Big]_{\mathrm{production}} + \frac{dn^q}{dt}\Big]_{\mathrm{loss}}. \tag{5.3}$$

Here the first and second term on the right hand side describe the same processes as those of Equation 5.2. The third term includes production of monomers, and the final loss term takes ion recombination into account in addition to wall losses. The number of coupled equations become $3N_{\mathrm{tot}}$ +3, where the numbers three denote the three charging states of the aerosols

and three rate equations for neutral clusters and ions. The code is written in a modular form to allow easy modification, expansion or decoupling of each of the terms.

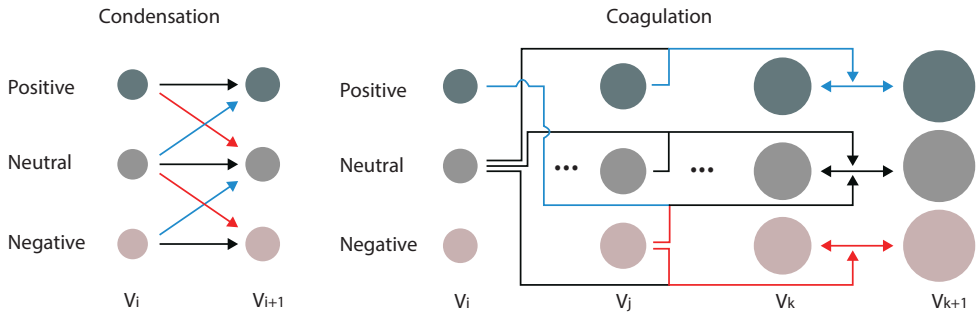

Figure 5.2: Diagram showing how condensation (left) and coagulation (right) transports . For the condensation, the charge of the condensing element is symbolized by the color of arrow (red for negative, black for neutral, blue for positive). For the coagulation, the joint volume of aerosols v_i and v_j is split between node at volume v_k and v_{k+1} taking charge into account.

5.3.1 Nucleation

A nucleation term specifies the amount of new aerosols generated per unit time at a specified critical volume v_*^q, where $q = [0, -, +]$ denotes the charge. The production of new aerosols at this size is set to a fixed rate J^q. The volume of the nucleated particles may fall in between two nodes, or below the lowest node. Following the design of Prakash et al. [2003] the number concentration is then scaled by volume and placed in the node immediately above it, such that

$$\left.\frac{dN_k^q}{dt}\right]_{\text{nucleation}} = \begin{cases} J^q \frac{v_*^q}{v_1}, & \text{for} \quad v_*^q \leq v_1 \\ J^q \frac{v_*^q}{v_k}, & \text{for} \quad v_{k-1} < v_*^q \leq v_k \\ 0, & \text{otherwise.} \end{cases} \tag{5.4}$$

Once ion-nucleation is applied it is important to maintain charge conservation. Positively and negatively nucleated aerosols take their charge from the ions in a number corresponding to what was nucleated at the critical volume, and this charge has to be subtracted from the positive and negative ion equations, i.e.,

$$\begin{aligned} \left.\frac{dn^-}{dt}\right]_{\text{nucleation}} &= -J^-, \\ \left.\frac{dn^+}{dt}\right]_{\text{nucleation}} &= -J^+. \end{aligned} \tag{5.5}$$

This simplistic view on aerosol nucleation is easily expanded. The nucleation could be modified to depend on other quantities in the model such as neutral cluster and ion concentrations, temperature and/or further parametrisation [Yu, 2010, Dunne et al., 2016, Määttänen et al.].

Table 5.1: Table with variables and their descriptions used in the present paper.

Symbol	Unit	Description
v_k	m^3	Volume of aerosol node k.
v^q	m^3	Volume of monomer of charge q.
v_{min}	m^3	Volume of the smallest node.
v_{max}	m^3	Volume of the largest node.
v_*^q	m^3	Critical volume at which nucleation tales place for aerosols at charge q.
t	s	Time.
C		Ratio between volumes of two neighbouring nodes
N_{tot}		Number of logarithmically spaced size nodes.
q, p		Indices specifying charge, may be $(0, -, +)$ dictating negative, neutral and positive charge respectively.
i, j, k		Indices specifying node number.
σ		Index with values 1,2,3,4.
N_k^q	m^{-3}	Particle concentration of particles at node number k and charge q.
N_L	m^{-3}	Concentration of large mode aerosols used in scavenging loss term.
n^q	m^{-3}	Concentrations of neutral ($q = 0$) or ion monomers ($q = -$ or $q = +$).
J^q	$m^{-3}s^{-1}$	Nucleation rate of charged or neutral aerosols.
β_k^{qp}	m^3s^{-1}	Condensation coefficient of interactions between a monomer of charge q and an aerosol of charge p at size node k.
$\kappa_{i,j}^{qp}$	m^3s^{-1}	Coagulation coefficient of interactions between an aerosol from size node i and charge q, and another aerosol from size node j and charge p.
β_L^{q0}	m^3s^{-1}	Condensation coefficient for loss of monomers of charge q onto large mode scavenging aerosols.
$\kappa_{k,L}^{q0}$	m^3s^{-1}	Coagulation coefficient for losses of an aerosol from size node k and charge q, and a large mode scavenging aerosol.
$S_{i,j}$		Splitting matrix denoting the fractional contribution of two coagulating particles from node i and j to two neighboring nodes.
P	$m^{-3}s^{-1}$	Neutral cluster production rate.
Q	$m^{-3}s^{-1}$	Ion-pair production rate.
α	m^3s^{-1}	Recombination coefficient.
d	m	Aerosol diameter.

5.3.2 Condensation

Three channels of condensation of clusters onto aerosol particles are allowed: Neutral clusters of concentration n^0 condensing onto all aerosols, and two classes of ions n^+ and n^- with a single charge condensing onto neutral aerosols or aerosols of opposite sign. Schematically we write:

$$\left.\frac{dN_k^q}{dt}\right]_{\text{condensation}} = \left.\frac{dN_k^q}{dt}\right]_{\text{cond},n^0} + \left.\frac{dN_k^q}{dt}\right]_{\text{cond},n^+} + \left.\frac{dN_k^q}{dt}\right]_{\text{cond},n^-}, \tag{5.6}$$

where $q = [0, -, +]$ indicate the neutral, positive and negative charges respectively. This yields three equations of three terms summarized in the following equation:

$$\left.\frac{dN_k^q}{dt}\right]_{\text{condensation}} = -\sum_p I_k^{qp} N_k^p + \sum_p I_{k-1}^{qp} N_{k-1}^p, \tag{5.7}$$

where

$$I_k^{qp}(r,t) = \begin{pmatrix} A_k^0 n^0 \beta_k^{00} & A_k^+ n^+ \beta_k^{+-} & A_k^- n^- \beta_k^{-+} \\ A_k^- n^- \beta_k^{-0} & A_k^0 n^0 \beta_k^{0-} & 0 \\ A_k^+ n^+ \beta_k^{+0} & 0 & A_k^0 n^0 \beta_k^{0+} \end{pmatrix}. \tag{5.8}$$

For an aerosol to grow from volume v_k to v_{k+1}, a number $(v_{k+1} - v_k)/v^q$ of condensing monomers of volume v^q is needed. The coefficients $A_k^q = v^q/(v_{k+1} - v_k)$ are thus the fractional volume that one condensing monomer contributes to growing an aerosol from volume v_k to v_{k+1}. This is analogous to the treatment of condensation in e.g. Prakash et al. [2003]. q and p indicate the charge, and the β_k^{qp} denotes the interaction coefficient between a monomer (neutral or ion) of charge $q = [0, -, +]$ and an aerosol at size node k and charge $p = [0, -, +]$. The diagonal elements account for the usual condensation of neutral clusters, while the other four non-zero elements make up the terms related to the condensation of ions. The 0-terms in the matrix represent the negligible interactions between like-charged ions and aerosols.

As monomers condense onto the aerosols, neutral cluster and ion concentrations change accordingly:

$$\begin{aligned} \left.\frac{dn^0}{dt}\right]_{\text{condensation}} &= -n^0 \sum_{k=1}^{N_{\text{tot}}} \left(\beta_k^{00} N_k^0 + \beta_k^{0+} N_k^+ + \beta_k^{0-} N_k^-\right), \\ \left.\frac{dn^-}{dt}\right]_{\text{condensation}} &= -n^- \sum_{k=1}^{N_{\text{tot}}} \left(\beta_k^{-0} N_k^0 + \beta_k^{-+} N_k^+\right), \\ \left.\frac{dn^+}{dt}\right]_{\text{condensation}} &= -n^+ \sum_{k=1}^{N_{\text{tot}}} \left(\beta_k^{+0} N_k^0 + \beta_k^{+-} N_k^-\right). \end{aligned} \tag{5.9}$$

The code can easily switch on/off the terms related to the usual condensation and ion-condensation separately. The reverse process, loss of aerosol volume due to evaporation, is not implemented in the present model since only stable clusters are considered. Note that evaporation is not needed for demonstrating the novel feature of ion-condensation. It is straight forward to include evaporation as a future extension of the model.

5.3.3 Monomer production

A term describing the production of the monomers is included in the model in the following simple way

$$\left.\frac{dn^0}{dt}\right]_{\text{production}} = P, \tag{5.10}$$

$$\left.\frac{dn^-}{dt}\right]_{\text{production}} = Q, \tag{5.11}$$

$$\left.\frac{dn^+}{dt}\right]_{\text{production}} = Q. \tag{5.12}$$

Here, P is the production rate of the neutral cluster elements n^0, Q is the ion-pair production rate. Both rates are input to the model as constants, but can easily be generalized to describe more advanced cases. The code allows for bypassing the production rates to keep a constant concentration of any of the n^q. Note that the production of monomers is a term different from the nucleation term: Production is the process with which monomers is introduced into the model. Nucleation is the process where monomers join to become stable aerosols.

5.3.4 Coagulation

When particles of volume v_i and v_j coagulate, they produce a new particle with a volume $v_i + v_j$, which may in general lie between two nodes k and $k+1$. Thus the coagulated volume needs to be split and distributed between N_k^q and N_{k+1}^q. To do so, we calculate a matrix giving for each i, j pair the index k of the node immediately below the new coagulated volume:

$$V_{ij} = f_k(v_i + v_j) = \text{floor}\left[N_{\text{tot}}\left(\frac{\log(v_i + v_j) - \log v_{\text{min}}}{\log v_{\text{max}} - \log v_{\text{min}}}\right)\right]. \tag{5.13}$$

v_{min} is the volume of the smallest node, and v_{max} that of the largest. We also calculate a splitting fraction function

$$f_s(v) = \frac{v_{k+1} - v}{v_{k+1} - v_k}, \tag{5.14}$$

where $f_s(v)$ is a function giving the volume fraction added to node $k = f_k(v)$ while $1 - f_s(v)$ is added to node $k+1$. The function $f_s(v)$ is defined such that $v = f_s(v_k)v_k + (1 - f_s(v_k))v_{k+1}$, implying that the total volume is conserved with this definition of splitting.

To save computing time, a splitting matrix is calculated during initialization and used throughout the calculation. Its terms are

$$S_{ij} = f_s(v_i + v_j) = \frac{v_{k+1} - (v_i + v_j)}{v_{k+1} - v_k}. \tag{5.15}$$

The charge gives rise to four types of coagulation between the aerosols: Neutral with neutral, positive with neutral, neutral with negative, and positive with negative. These have four corresponding coagulation coefficient matrices: $\kappa_{ij}^{00}, \kappa_{ij}^{+0}, \kappa_{ij}^{0-}, \kappa_{ij}^{+-}$, each of dimension $N_{\text{tot}} \times$

N_{tot}. Coagulation of like-signed aerosols is neglected, as the model only incorporates single-charge species. During one time step, we can then calculate the interaction terms from each coagulation contribution:

$$\widetilde{I_{ij}^{\sigma}} = \begin{pmatrix} I_{ij}^{00} \\ I_{ij}^{+0} \\ I_{ij}^{0-} \\ I_{ij}^{+-} \end{pmatrix} = \begin{pmatrix} \kappa_{ij}^{00} N_i^0 N_j^0 \\ \kappa_{ij}^{+0} N_i^+ N_j^0 \\ \kappa_{ij}^{0-} N_i^0 N_j^- \\ \kappa_{ij}^{+-} N_i^+ N_j^- \end{pmatrix}. \tag{5.16}$$

The rules for mapping coagulation of two particles of given charges into its electrically relevant node are summarized by the following three matrices:

$$K^{q\sigma} = \begin{pmatrix} \frac{1}{2} & 0 & 0 & 1 \\ 0 & 0 & 1 & 0 \\ 0 & 1 & 0 & 0 \end{pmatrix}, \quad L^{q\sigma} = \begin{pmatrix} -\frac{1}{2} & 0 & -1 & 0 \\ 0 & 0 & 0 & 0 \\ 0 & -1 & 0 & -1 \end{pmatrix}, \quad M^{q\sigma} = \begin{pmatrix} -\frac{1}{2} & -1 & 0 & 0 \\ 0 & 0 & -1 & -1 \\ 0 & 0 & 0 & 0 \end{pmatrix}. \tag{5.17}$$

As before, q denotes the charge of the end-product, and σ is a number between 1 and 4 denoting one of the four possible types of coagulation.

As aerosols at size node i coagulate with those at node j, and distribute their joined volume between node k and $k+1$ where k is a function of i and j, the rate of change in the four nodes is as follows:

$$\begin{aligned} \left.\frac{dN_k^q}{dt}\right]_{\mathrm{coag}} &= S_{ij} \sum_{\sigma} K^{q\sigma} \widetilde{I_{ij}^{\sigma}}, \\ \left.\frac{dN_{k+1}^q}{dt}\right]_{\mathrm{coag}} &= (1 - S_{ij}) \sum_{\sigma} K^{q\sigma} \widetilde{I_{ij}^{\sigma}}, \\ \left.\frac{dN_i^q}{dt}\right]_{\mathrm{coag}} &= \sum_{\sigma} L^{q\sigma} \widetilde{I_{ij}^{\sigma}}, \\ \left.\frac{dN_j^q}{dt}\right]_{\mathrm{coag}} &= \sum_{\sigma} M^{q\sigma} \widetilde{I_{ij}^{\sigma}}. \end{aligned} \tag{5.18}$$

Repeating this for all combinations of i and j yields the total coagulation term. All coagulation channels are covered within the four terms of Eq (5.16) as the summation runs through all combinations of i and j. The neutral - neutral interactions however are counted twice since e.g. the coagulation for $i = 1$ and $j = 2$ represents the same process as $i = 2$ and $j = 1$ if both particles are neutral. This is compensated for by the factor of $\frac{1}{2}$ on all neutral - neutral coagulation terms from the matrices of Eq. (5.17).

5.3.5 Loss terms

When simulating an experimental situation where an atmospheric reaction chamber is used, loss of aerosols to the walls may be of importance. To accommodate this, a size dependent loss on N_k^q, $n^{\pm}$, and n_0 is added to the model. An example of such a loss term was found empirically to depend on aerosol diameter as $dN_k/dt = -\lambda(d/d_0)^{-\gamma} N_k$, where $\gamma = 0.69$ and $\lambda = 6.2 \times 10^{-4}\,\mathrm{s}^{-1}$ and $d_0 = 2\,\mathrm{nm}$, for an $8\,\mathrm{m}^3$ reaction chamber [Svensmark et al.,

2013]. Furthermore, we include losses to large aerosols at concentration N_L and diameter d_L. Extending this to charged aerosols and monomers, the wall loss term can be written for the aerosols as

$$\left.\frac{dN_k^q}{dt}\right]_{\text{loss}} = -\lambda\left(\frac{d_k}{d_{\text{loss}}}\right)^{-\gamma} N_k^q - N_k^q \kappa_{kL}^{q0} N_L, \tag{5.19}$$

where $d_{\text{loss}} = 2\,\text{nm}$ and d_k is the diameter corresponding to volume node k, and κ_{kL}^{q0} is the coagulation coefficient between the k'th aerosol of charge q and the large aerosol. For the monomers we have

$$\left.\frac{dn^q}{dt}\right]_{\text{loss}} = -\lambda\left(\frac{d^q}{d_{\text{loss}}}\right)^{-\gamma} n^q - n^q \beta_L^{q0} N_L + \left.\frac{dn^q}{dt}\right]_{\text{recomb}}, \tag{5.20}$$

where d^q are the diameters of the monomers, and β_L^{q0} is the interaction coefficient between the k'th aerosol of charge q and the large aerosol. Here λ, γ, d_{loss}, d_L and N_L as well as the coefficents β_k^{qp} and κ_{ij}^{qp} serve as inputs to the model. The losses due to ion-ion recombination are implemented through the recombination coefficient α, such that the recombination term in Equation 5.20 contains

$$\left.\frac{dn^-}{dt}\right]_{\text{recomb}} = -\alpha n^- n^+, \tag{5.21}$$

$$\left.\frac{dn^+}{dt}\right]_{\text{recomb}} = -\alpha n^- n^+, \tag{5.22}$$

$$\left.\frac{dn^0}{dt}\right]_{\text{recomb}} = 0. \tag{5.23}$$

This means that recombining ions effectively disappear from the model. Note that the recombination coefficient $\alpha = 1.6 \times 10^{-6}\,\text{cm}^3\text{s}^{-1}$ is used, and set as a constraint on the coefficients β_k^{qp} and κ_{ij}^{qp} we use for demonstration purposes here (see section on parameters and the Appendix). Condensation of monomers onto aerosols in the largest size node are also lost from the model. Coagulation of an aerosol pair outside the range spanned by the size nodes have their joint volume split according to the splitting matrix in Equation 5.15, and the upwards moving fraction is lost. Other types of loss such as rain out could be added in the code.

5.3.6 Parameters

To accurately simulate the interactions of aerosols through the channels mentioned above, the interaction coefficients β_k^{qp} and κ_{ij}^{qp} must be described as accurately as possible. These interactions depend on the species that are modeled and the environment they exist in. We model the interaction caused by condensation of hydrated sulphuric acid clusters onto sulphuric acid-water-aerosols and ions in later parts of the present work. To do that we model neutral clusters, ions and aerosols as electrostatically interacting spheres including their image induction in one another. Furthermore Van der Waals forces, viscous forces and dipole moment of the sulfuric acid population are included along with Brownian coagulation to make up the coefficients β. Further information on how the coefficients have been calculated can be found in the Appendix. Figure 5.3 displays the β coefficients as a function of aerosol diameter.

The choice of parameters for this figure are $m^0 = 100\,\text{AMU}$, $m^+ = m^- = 225\,\text{AMU}$ to match theoretical assumptions of SESS17, and densities are set to $\rho^0 = \rho^+ = \rho^- = 1200\,\text{kg m}^{-3}$ (Figure 10.13 of Seinfeld and Pandis [2006]). This models the behavior of hydrated sulphuric acid clusters, ions, and aerosols at 300 K. These coefficients are used throughout the paper, unless otherwise is explicitly stated. The model takes condensation and coagulation coefficient tables as input prior to any calculations, and thus any relevant coefficients may be provided.

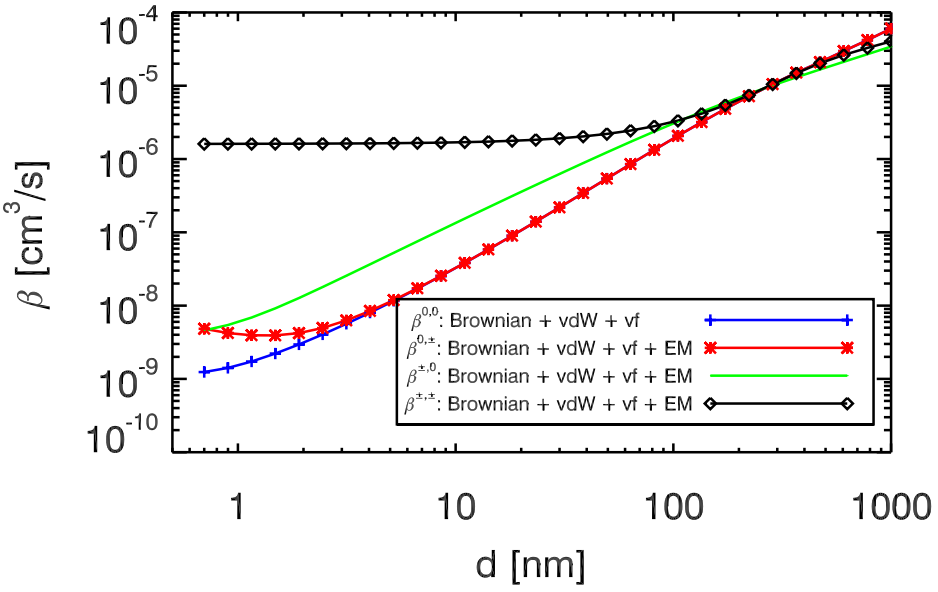

Figure 5.3: The condensation coefficients β for a neutral cluster monomer or charged ion interacting with aerosols. The potentials are: vdW: Van der Waals potential. vf: Viscious forces. EM: Electrostatic potential. The neutral clusters are here H_2SO_4 and are assumed to have a mass of 100 AMU. Ions have masses of 225 AMU.

5.4 Benchmarking the model

To validate the model, we test whether it can reproduce known solutions to the GDE for simple initial conditions. Thus a number of benchmark tests are performed. First a visual representation of the model output is shown in Figure 5.4. In this example the model was initiated with a steady state distribution. Then, after 8 hours the nucleation rate was increased by a factor of 2 along with a change in the ion-pair production rate from $16\,\text{cm}^{-3}\text{s}^{-1}$ to $500\,\text{cm}^{-3}\text{s}^{-1}$. After 8 additional hours the ion-pair production and nucleation rate was stepped back down, and this process was repeated 5 times. The figure displays in the first panel the distribution for all aerosols (i.e. $N_k^0 + N_k^+ + N_k^-$) as a function of time. In the lower panels are the neutral, positive and negative aerosols only also as a function of time. In all figures a clear growth profile is seen with a period of 16 hours, however significant numerical diffusion affects the simulation for higher radii.

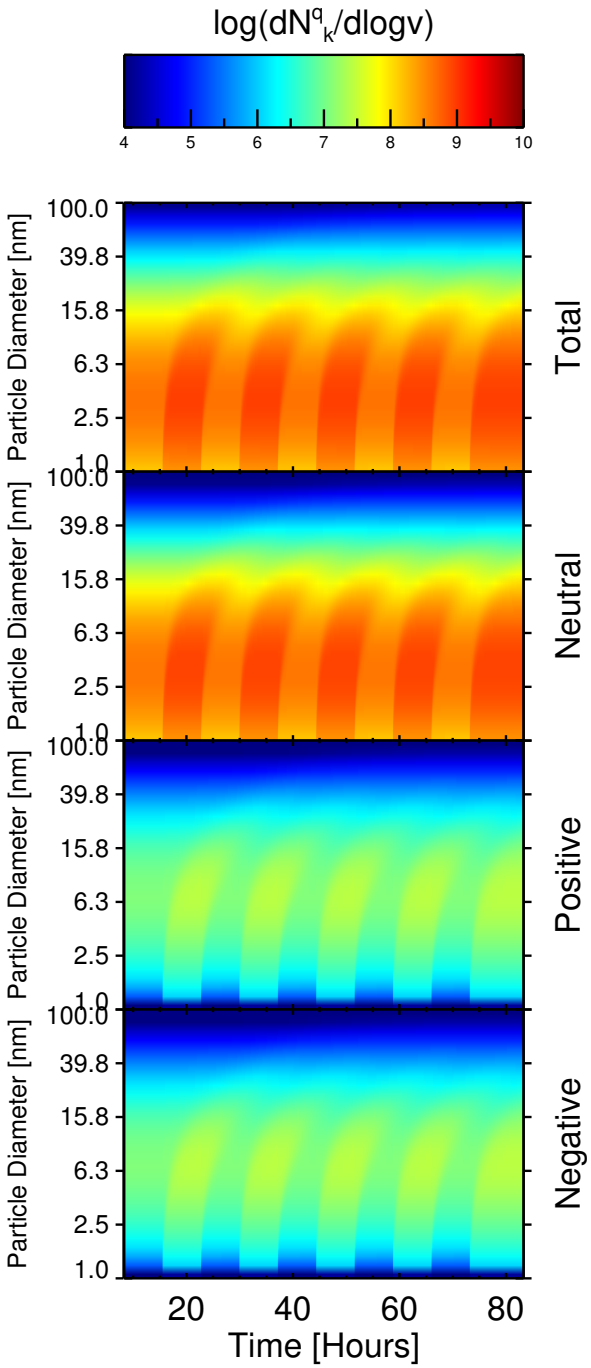

Figure 5.4: 16 hour cycles of neutral aerosol nucleation rate $J^0 = 0.1\,\mathrm{cm}^{-3}\mathrm{s}^{-1}$ and $J^0 = 0.2\,\mathrm{cm}^{-3}\mathrm{s}^{-1}$, with ionization rates also alternating between $Q = 16\,\mathrm{cm}^{-3}\mathrm{s}^{-1}$ and $Q = 500\,\mathrm{cm}^{-3}\mathrm{s}^{-1}$. Coagulation is not included for this particular calculation.

5.4.1 Testing condensation and coagulation

To see that the condensation mechanism is on par with expectations, a known distribution of aerosols is propagated forward in time while neglecting all contributions to the GDE other

than the condensation term. The numerical model output can then be compared to an analytic temporal evolution of the same initial conditions. The condensation equation can be written as

$$\frac{\partial n(d,t)}{\partial t} + \frac{A}{d}\frac{\partial n(d,t)}{\partial d} = \frac{A}{d^2}n(d,t) \tag{5.24}$$

where $A = 4D_i M_i(p_i - p_{\mathrm{eq,i}})/RT\rho_p$ is a constant. An initial continuous lognormal aerosol distribution

$$n(d,0) = \frac{N_0}{\sqrt{2\pi}d\,\ln\sigma_g}\exp\left(-\frac{\ln^2(d/D_g)}{2\ln^2\sigma_g}\right) \tag{5.25}$$

is grown using only the condensation section of the model (see eg. Seinfeld and Pandis [2006] Equation (13.26)). Here N_0 is the number of aerosols, while D_g and σ_g determine the shape of the distribution. Analytically, this solves to

$$n(d,t) = \frac{d}{(d^2-2At)}\frac{N_0}{\sqrt{2\pi}d\,\ln\sigma_g}\exp\left(-\frac{\ln^2\left[(d^2-2At)^{1/2}/D_g\right]}{2\ln^2\sigma_g}\right). \tag{5.26}$$

In figure 5.5, the analytical solution as well as a corresponding simulation is seen for the parameters i.e. interaction coefficients written in the Figure caption. As can be seen, the peak of the distribution follows the analytical form as expected, however as the number of volume nodes decreases the numerical diffusion becomes more apparent. The significant numerical diffusion notably becomes an issue for low number of nodes, and as such direct implementation of the present algorithm in larger scale atmospheric models will be difficult due to computational cost. Here, moving center or two-moment methods could be considered.

We will now test the coagulation. The coagulation equation (Equation 13.72 of Seinfeld and Pandis [2006]), for a constant coagulation coefficient $\kappa_k^{qp} = K$ and initial continuous distribution

$$n(v,0) = \frac{N_0^2}{V_0}\exp\left(\frac{-vN_0}{V_0}\right) \tag{5.27}$$

solves to

$$n(v,t) = \frac{N_0^2}{V_0\left(1+t/\tau_c\right)^2}\exp\left(-\frac{vN_0}{V_0\left(1+t/\tau_c\right)}\right). \tag{5.28}$$

Note that now n is a function of aerosol volume v. The characteristic time $\tau_c = 2/(KN_0)$, N_0 is the number concentration of particles at the onset of the calculation or simulation, and V_0 is total volume concentration. The above analytic solution is compared with the numerical solution in Figure 5.6 left panel. The black lines show the particle spectrum for $t = 0$ as calculated by Eq. 5.28, and the black symbols show the simulated aerosol spectrum at the same instant. The red line and red symbols are the analytic and numerical solution evolved over $t = 12$ hours. The behavior of the simulated spectra is seen to follow closely that of the analytic ones. It should be noted however, that as time progresses the largest particles coagulate beyond the upper size node, and as such the volume of simulated coagulation is not strictly conserved. This manifests itself as slight deviations from the analytic solutions towards the high end of the spectrum, and worsens as time progresses.

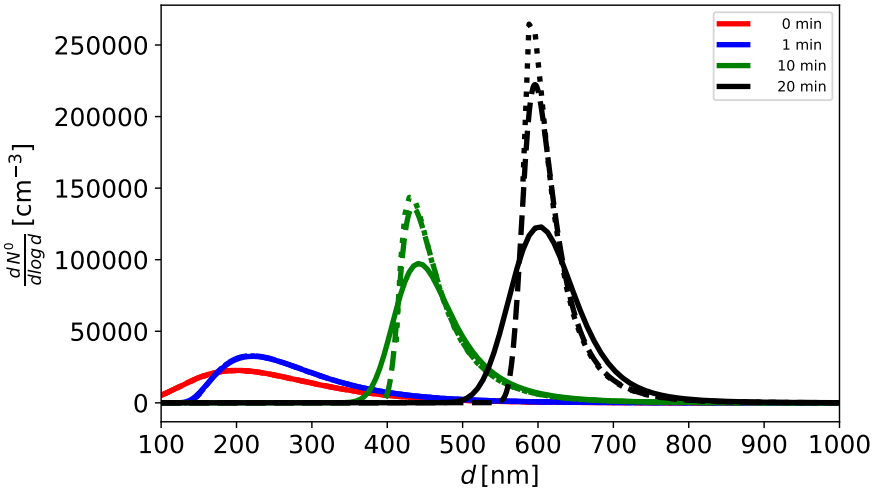

Figure 5.5: Pure condensation for an initial lognormal distribution of aerosols from equation 5.25, using $\sigma_g = 1.5$, $D_g = 200 \times 10^{-9}\,\mathrm{m}$ and $N_0 = 10000\,\mathrm{cm}^{-3}$. The condensation coefficients used for this reflect the choice of $(p_i - p_{\mathrm{i,eq}}) = 10^{-9}\,\mathrm{atm}$, $M_i = 100\,\mathrm{g/mol}$, $D_i = 10^{-5}\,\mathrm{m^2 s^{-1}}$, $T = 300\,\mathrm{K}$, $\rho_p = 1.2\,\mathrm{g\,cm^{-3}}$). Dotted lines show the analytical solution, solid lines are snapshots from a condensation-only simulation, and dashed lines are a similar simulation with a factor of 10 higher density of volume nodes, lowering the numerical diffusion at a high cost in computation. For the solid lines, two adjacent nodes are a factor of 1.013 apart.

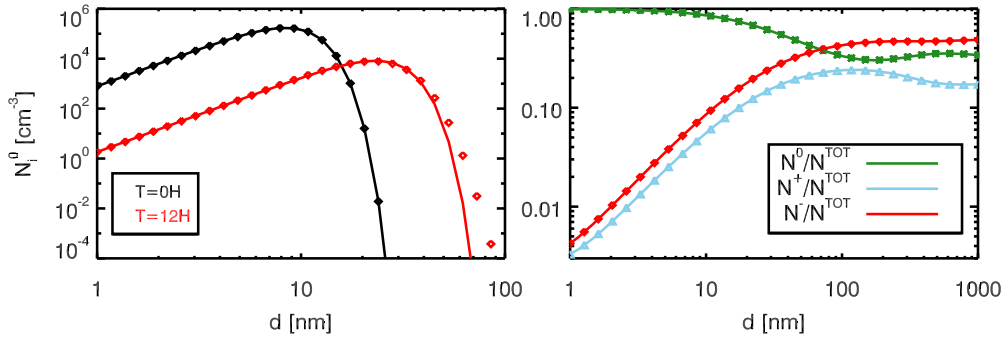

Figure 5.6: Left: The particle spectrum initially (black) and after 12 hours of simulation for a distribution of the form Eq. 5.28 subject to coagulation only, with a constant coagulation coefficient $K = 10^{-15}\,\mathrm{cm^3 s^{-1}}$. It can be noted that the analytic and model distributions begin to deviate for larger aerosol diameters as time progresses. This is an effect of the logarithmic spacing of the size nodes, as can be seen also in Figure 15.2 of Jacobson [2005]. Right: Fraction of neutral, positively charged and negatively charged aerosols relative to the total number, as calculated by the model run in steady state (points), and calculated analytically (lines). The plotted quantities are shown in the legend, and that the y-axis is unitless. In this particular model run, the mass of the ions are deliberately very different for demonstration purposes: The mass of the neutral monomer is 100 AMU, positive ion is 325 AMU and negative ion is 150 AMU. These masses are also reflected in the interaction coefficients, which is directly pronounced in the positive and negative aerosol fraction.

5.4.2 Charge Distribution in Steady State

A good benchmark for an aerosol model that handles charge is that the charged fractions of aerosols at a given volume node meet analytic expectations. The fraction of charged aerosols in a steady state scenario depends on the coefficients chosen for ion and aerosol interactions. These in turn are affected by a number of parameters, of which some are the ion masses. The ratio of the charged to neutral aerosol concentrations at a given volume node at steady state can be expressed as

$$\frac{N_k^+}{N_k^0} = \frac{n^+\beta_k^{+0}}{n^-\beta_k^{-+}}, \tag{5.29}$$

$$\frac{N_k^-}{N_k^0} = \frac{n^-\beta_k^{-0}}{n^+\beta_k^{+-}}, \tag{5.30}$$

which depends only on ion concentrations and condensation coefficients [Hoppel, 1985]. If $N_k^{\mathrm{tot}} = N_k^0 + N_k^+ + N_k^-$ then the above equations solve to

$$\begin{aligned}
\frac{N_k^0}{N_k^{\mathrm{tot}}} &= \left(1 + \frac{n^-\beta_k^{-0}}{n^+\beta_k^{+-}} + \frac{n^+\beta_k^{+0}}{n^-\beta_k^{-+}}\right)^{-1}, \\
\frac{N_k^+}{N_k^{\mathrm{tot}}} &= \left(1 + \frac{n^-\beta_k^{-+}}{n^+\beta_k^{+0}}\left(1 + \frac{n^-\beta_k^{-0}}{n^+\beta_k^{+-}}\right)\right)^{-1}, \\
\frac{N_k^-}{N_k^{\mathrm{tot}}} &= \left(1 + \frac{n^+\beta_k^{+-}}{n^-\beta_k^{-0}}\left(1 + \frac{n^+\beta_k^{+0}}{n^-\beta_k^{-+}}\right)\right)^{-1}.
\end{aligned} \tag{5.31}$$

As an illustration, different condensation coefficients are chosen by setting the neutral monomer mass to $100\,\mathrm{AMU}$, positive ion mass to $325\,\mathrm{AMU}$ and negative ion to $150\,\mathrm{AMU}$ (as opposed to later, where positive and negative ion masses are assumed equal). The model is then run into a steady state. The continuous lines of Figure 5.6 in the lower right hand panel, show the analytic charge fractions given by Equation 5.31 as a function of aerosol diameter. The modeled charged aerosol fractions are shown as the diamond symbols, and demonstrate a good agreement between the analytical and modeled solutions. The model also reproduces the common observation that aerosols generally have a higher negative than positive charging state, due to differences in ion size and thus mobility [Wiedensohler, 1988, Enghoff and Svensmark, 2017], although the choice of masses in the present example may exaggerate this effect. Note that for larger aerosols (above $\sim$100 nm) multiple charging starts to be relevant even though it is not included in the model. In cases with large number of $>$100 nm aerosols this would begin to impact the amount of available small ions. For most atmospherically relevant situations this will not be a significant issue.

5.5 Case study: Simulated ion-induced condensation

One of the core features of the model presented in this work is the inclusion of the GDE terms describing ion induced condensation. It is of natural interest to quantify how this growth

channel compares to neutral condensation, and this has indeed already been done in SESS17 taking a theoretical and experimental approach. Here it was shown that ion-condensation can be an important addition to the neutral condensation growth of aerosols under atmospheric conditions. It was found, that the addition of small concentrations of ions relative to the neutral condensable clusters heightened the probability of small nucleated aerosols surviving to cloud condensation nuclei (CCN) sizes $> 50\,\mathrm{nm}$, which will have an impact on cloud micro-physics in the terrestrial atmosphere. The strength of the theoretical ion-condensation description is that it shows how the ions contribution to growth rate is independent of aerosol size distribution. This description however neglects growth from coagulation, which may also be affected by the presence of ions. While the theoretical result of SESS17 is consistent with the experimental findings of the same paper, it is interesting to expand on aerosol growth from ion induced condensation in the context of neutral and charged coagulation. In order to do so, we first reconsider the theoretical description of aerosol growth in the context of charge. Our focus will lie on the growth rate

$$GR = \frac{d\,d}{dt} \tag{5.32}$$

of aerosols at diameter d, and explore the conditions under which ion-induced condensation can be said to be important.

5.5.1 Condensation growth rate

In the case of purely neutral condensation, the growth rate can be written as

$$GR^0_{\mathrm{cond}} = A_0 n^0 \beta^{00}, \tag{5.33}$$

where $A_0 = (m^0/4\pi(d/2)^2\rho)$ is simply a constant related to the aerosol and monomer, such that d is the aerosol diameter, m^0 the monomer mass and ρ their density (SESS17). The 0 superscript in the LHS indicates that only neutral condensation is considered. In the presence of ions, the contribution to the condensation is presented in SESS17 as

$$GR^{\pm}_{\mathrm{cond}} = A_0 n^0 \beta^{00}\,(1+\Gamma)\,, \tag{5.34}$$

where

$$\Gamma = 4\left(\frac{n^{\pm}}{n^0}\right)\left(\frac{\beta^{\pm 0}}{\beta^{00}}\right)\left(\frac{m^{\pm}}{m^0}\right)\left(\frac{N^0(d)}{N^{\mathrm{tot}}(d)}\right). \tag{5.35}$$

Γ is then the increase in growth rate caused by ion-condensation relative to the neutral growth rate for pure neutral condensation. Positive and negative ions are treated symmetrically, such that interaction coefficients for the two species are $\beta^{+0} = \beta^{-0} = \beta^{\pm 0}$, $m^+ = m^- = m^{\pm}$ and $n^+ = n^- = n^{\pm}$. The final factor N^0/N^{tot} is given in Equation 5.31 assuming charge equilibrium. Note that all β are functions of aerosol diameter as shown in Figure 5.3. In Figure 5.7 on the left Γ can be seen for a charge equilibrated distribution of aerosols with sulfuric acid monomers $n^0 = 10^6\,\mathrm{cm}^{-3}$, $m^0 = 100\,\mathrm{AMU}$, $m^{\pm} = 225\,\mathrm{AMU}$ for a couple of ion-pair concentrations. As expected, Γ scales with $n^{\pm}$.

5.5.2 Coagulation growth rate

While the result of the condensation above is universally applicable to any aerosol distribution, a similar expression is harder to achieve for the coagulation, where aerosols of all diameters may coagulate with each other. Here we shall consider the growth rate of a mono-disperse distribution for simplification, and then compare with simulations that are reasonably approximated as such. From Equation 9 of Leppä et al. [2011], the growth rate of a monodisperse concentration N^T of completely neutral aerosols due to coagulation is

$$GR^0_{\text{coag}} = \frac{d\, k^{00} N^T}{6}. \tag{5.36}$$

Here $k^{00}(d) = \kappa^{00}(d,d)$ is the neutral-neutral coagulation coefficient of particles at equal diameters. k^{00} is thus a function of diameter. Introducing ions, a fraction of the monodisperse aerosols will obtain a single charge. In this case, the growth rate from coagulation is

$$GR^{\pm}_{\text{coag}} = \frac{d}{3N^T}\left[\frac{1}{2}k^{00}(N^0)^2 + k^{0+}N^0N^+ + k^{0-}N^0N^- + k^{+-}N^+N^-\right]. \tag{5.37}$$

As in the model, the terms with interactions between two positive aerosols and two negative aerosols have been neglected. Again all coagulation coefficients k^{0+}, k^{0-} and k^{+-} are functions of d, and now $N^T = N^0 + N^+ + N^-$. If we assume that $k^{0\pm} = k^{0-} = k^{0+}$, and $N^{\pm} = N^+ = N^-$ then

$$\begin{aligned} GR^{\pm}_{\text{coag}} &= \frac{d}{3N^T}\left[\frac{1}{2}k^{00}(N^0)^2 + 2k^{0\pm}N^0N^{\pm} + k^{+-}(N^{\pm})^2\right] && (5.38)\\ &= \frac{d\, k^{00} N^T}{6}\left[\left(\frac{N^0}{N^T}\right)^2 + 4\frac{k^{0\pm}}{k^{00}}\left(\frac{N^{\pm}}{N^T}\frac{N^0}{N^T}\right) + 2\frac{k^{+-}}{k^{00}}\left(\frac{N^{\pm}}{N^T}\right)^2\right] && (5.39)\\ &= \frac{d\, k^{00} N^T}{6}\left(1+\Lambda\right), && (5.40) \end{aligned}$$

where

$$(1+\Lambda) = \left[\left(\frac{N^0}{N^T}\right)^2 + 4\frac{k^{0\pm}}{k^{00}}\left(\frac{N^{\pm}}{N^T}\frac{N^0}{N^T}\right) + 2\frac{k^{+-}}{k^{00}}\left(\frac{N^{\pm}}{N^T}\right)^2\right]. \tag{5.41}$$

The relative concentrations of the $1+\Lambda$ expression can be calculated based on Equation 5.31 assuming the aerosols to be in equilibrium with respect to their charge. Then Λ is independent of N^T and $n^{\pm}$. Thus the GR from coagulation has a unit-less and diameter dependant adjustment $\Lambda(d)$ that is given by the coagulation coefficients and equilibrium charge fractions. Λ can be seen plotted in Figure 5.7 on the left. For $d > 100\,\text{nm}$, Λ actually becomes slightly negative, since the assumption of like-charged coagulation is neglected. Including the like-charged terms in Equation 5.37 would produce an increase $\widetilde{\Lambda}$ as seen in Figure 5.7, and for more advanced treatments multiple charge aerosol species could be included in the term. The fraction of multiply charged aerosols is however low for sizes below 100 nm, going from ≈1% to ≈5% between $d = 40\,\text{nm}$ and $d = 100\,\text{nm}$ [Hoppel and Frick, 1986]. As multi-charge aerosols are not handled by the model of the present work, we exclude it for consistency and direct comparison and use only Λ.

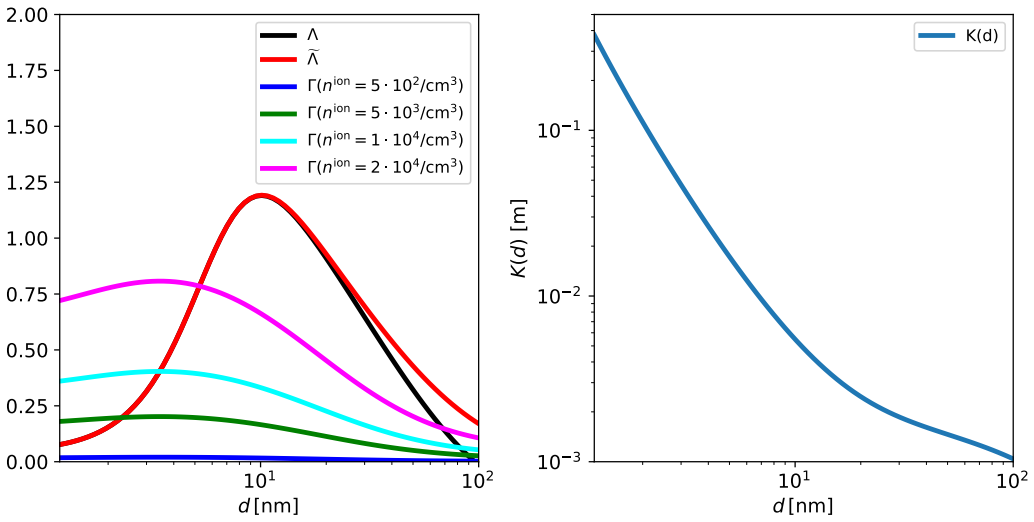

Figure 5.7: *Left:* The growth rate enhancement profiles associated with charged coagulation Λ and $\widetilde{\Lambda}$, and ion condensation growth rate enhancement profiles Γ for ion concentrations $n^{\pm}$ written in the legend. Note that all quantities are unitless. *Right*: $K(d)$ from Equation 5.42.

5.5.3 Growth rate increase from ions

With expressions for the neutral and charged growth rate from condensation and coagulation in hand, we can consider two cases: 1) The growth rate due to both coagulation and condensation for a neutral monodisperse concentration N^T of aerosols, and 2) The growth rate of the same concentration N^T of aerosols however with the presence of ions, condensing and charging a fraction of the aerosols. Taking the ratio of the two growth rates we obtain a measure of the increase in growth rate due to the presence of charging ions on aerosols at diameter d and concentration N^T:

$$\begin{aligned} \Omega &= \frac{GR^{\pm}_{\text{cond}} + GR^{\pm}_{\text{coag}}}{GR^{0}_{\text{cond}} + GR^{0}_{\text{coag}}} \\ &= \frac{K(d)\frac{n^0}{N^T}(1+\Gamma) + 1 + \Lambda}{K(d)\frac{n^0}{N^T} + 1}, \end{aligned} \tag{5.42}$$

where $K(d) = \frac{6A_0(d)}{d}\frac{\beta^{00}(d)}{k^{00}(d)}$. $K(d)$ can be seen in Figure 5.7, and ranges from $\approx 10^{-2}$ at $d = 5\,\text{nm}$ to $\approx 10^{-3}$ at $d = 100\,\text{nm}$.

To explore the regimes in which coagulation or condensation dominates the GR increase due to ions, we explore the limits of Equation 5.42. If we assume $N^T << K(d)n^0$ condensation is the dominant growth mechanism. Ω reduces to

$$\Omega = 1 + \Gamma. \tag{5.43}$$

On the other hand, if $N^T >> K(d)n^0$ then the coagulation is the dominant growth mechanism, and the expression reduces to

$$\Omega = 1 + \Lambda. \tag{5.44}$$

In the next subsection we simulate these two cases for appropriate atmospheric values, as well as cases in between, and compare with the equations above.

5.5.4 Growth rates in simulation

In order to calculate growth rates from the model, an initial number N^T of aerosols at $d = 1\,\text{nm}$ were grown in a loss-free environment with fixed sulfuric acid concentration n^0 and fixed ion concentration $n^{\pm}$, using parameters mentioned in Section 3.6. As our goal is to compare model and theoretical results, two consideration must be made: 1) We focus on the simulation mean diameter rather than GR for the entire distribution, and 2) when considering coagulation we must take into consideration the fact that the number of aerosols N^T changes dynamically in each simulation depending on ambient conditions.

Since the model suffers from numerical diffusion as well as a broadening of the originally narrow distribution due to coagulation itself, the simulation quickly departs from the mono-disperse initial conditions assumed above, so some extra care is needed to compare to the expressions in the previous subsection. At each point in time through each simulation we can calculate the mean aerosol volume in the simulation

$$\langle v \rangle = \frac{\Sigma_k N_k^T v_k}{\Sigma N_k^T}, \tag{5.45}$$

from which the mean diameter $\langle d \rangle$ is obtained. We can then consider the growth rate as

$$GR = \frac{d\langle d \rangle}{dt}. \tag{5.46}$$

The equivalent number of aerosols at this diameter is simply N^T:

$$N^T = \frac{\Sigma_k N_k^T v_k}{\langle v \rangle} = \Sigma_k N_k^T. \tag{5.47}$$

Assuming $d = \langle d \rangle$ enables us to compare the simulated growth rate of the mean diameter to that of the analytical mono-disperse distribution above. Then, we can produce simulated Ω by comparing the GR in simulations with similar N^T at similar $\langle d \rangle$ with and without ions present.

First, we focus on the condensation only-case of Equation 5.43, by decoupling the coagulation term from the model. Given a fixed ion-pair concentration $n^{\pm}$, an initially monodisperse distribution of $N^T = 1000\,\text{cm}^{-3}$ was grown towards higher diameters. Growth rates of the mean diameter in simulations of 20 different levels of $n^{\pm}$ was compared to the growth rate at the equivalent diameter of the neutral ($n^{\pm} = 0$) case for two levels of sulfuric acid $n^0 = 1 \times 10^6 \text{cm}^{-3}$ and $n^0 = 4 \times 10^6 \text{cm}^{-3}$. Both of these can be seen in Figure 5.8. The upper panel is equivalent to Figure 1 of SESS17. There is an excellent correspondence between

the expression for $\Omega = 1 + \Gamma$ and the simulated GR enhancement in a coagulation free environment. Γ scales with $n^{\pm}/n^0$, and by quadrupling n^0 from the top to the bottom panel in Figure 5.8, the effect is seen to be suppressed exactly with this factor in response. This is in effect the ion condensation effect.

Now, including also coagulation Equation 5.42 shows how Ω varies a function of d, $n^{\pm}$, n^0 and N^T. Within the course of a single simulation, as the aerosols coagulate N^T decreases, which in turn reduces the effect of coagulation. It is convenient to be able to compare growth rates at similar N^T while varying d, $n^{\pm}$ and n^0. Therefore, given an ion-pair concentration $n^{\pm}$, 20 simulations of initial N^T aerosols between $10^2\,\mathrm{cm}^{-3}$, and $10^8\,\mathrm{cm}^{-3}$ were computed. Then, even though N^T decreases with time within a single simulation, the growth rate of the mean diameter at concentration N^T could be interpolated between simulations. We assume a value of $n^0 = 10^6\,\mathrm{cm}^{-3}$, and for around 20 values of $n^{\pm}$ between 0 and $22005\,\mathrm{cm}^{-3}$ we allow aerosols at $1.1\,\mathrm{nm}$ and different initial concentrations to coagulate, condensate, and interact with ions. For each simulation, the growth rate $GR(\langle d \rangle)$ and total aerosol concentration $N^T(\langle d \rangle)$ of the mean diameter $\langle d \rangle$ is obtained. A subset of the simulation growth rates are seen in Figure 5.9. The trajectory of $\langle d \rangle$ in this space for a single simulation can be seen as beginning at the lowest value of $\langle d \rangle$, for an initial N^T, and growing towards higher values as time progresses while N^T decreases.

Interpolating in this space for two constant values of N^T yields the two panels of Figure 5.10. Here, the added effects of ions on the coagulation and condensation i.e. Λ and Γ are comparable in magnitude. As can be seen when comparing the pure condensation in Figure 5.8 and pure coagulation contained in Λ of Figure 5.7 with Figure 5.10, we can identify the two components that contribute to the charged growth rate enhancement. Ion induced condensation enhances growth rates for increasing $n^{\pm}$ and small diameters i.e. the bulge in the upper left corners. Added growth from charged coagulation via Λ manifests itself as an increase with diameter, followed by a decreases back to uncharged growth as coagulation coefficients for single-charge aerosols and neutral aerosols tend to be equal for very large diameters. This corresponds to the vertical band across the two figures. The coagulation effect is independent of $n^{\pm}$, as expected when aerosols are in a charged fraction equilibrium. In the top panel, a constant value of $N^T = 100\,\mathrm{cm}^{-3}$ is depicted. In the bottom panel, $N^T = 500\,\mathrm{cm}^{-3}$, and as expected, the contribution to Ω from coagulation at the higher total particle concentration is stronger while the condensation of ions remains the same. There is a good, but not 1-to-1 correspondence between the simulated and theoretical contours in the two figures, however the principal behaviour of theory and simulation is the same.

Holding instead $n^{\pm}$ as constant, and using vertical slices along the d direction of Figure 5.9 allows for the calculation of the data in Figure 5.11. In comparison to Figure 5.10 N^T is now varied instead of $n^{\pm}$. As N^T increases, coagulation and therefore Λ becomes progressively more dominant for Ω. Increasing $n^{\pm}$ from the top panel to the bottom panel makes the Γ ion condensation term contribute more to Ω for the lower diameter aerosols, on par with the theoretical Γ.

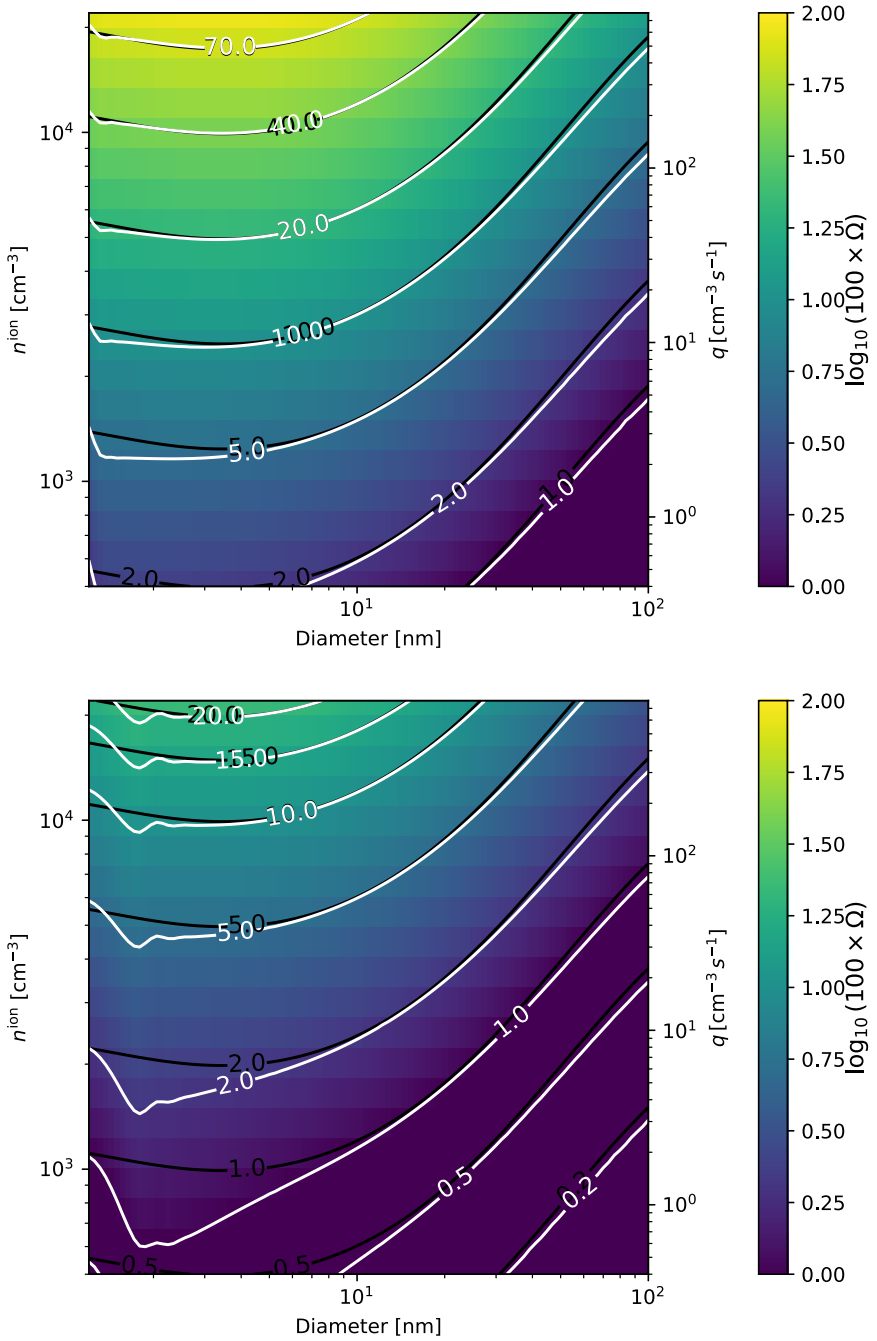

Figure 5.8: Charge enhancements of the growth rate Ω from condensation only. The black lines show the theoretical contours of equation 5.42, in percent. The white lines show contours of simulated Ω in percent. The colors represent the logarithm of the same simulated Ω in percent. The y-axis on the left hand side of the panels shows the fixed ion-pair concentration, and the right hand side shows the equivalent ion-pair production rate as calculated by $q = 1.6 \times 10^{-6}(n^{\pm})^2$ *Top*: Neutral monomer concentration $n^0 = 1 \times 10^6\,\mathrm{cm}^{-3}$, equivalent to Figure 1 of SESS17. *Bottom*: $n^0 = 4 \times 10^6\,\mathrm{cm}^{-3}$

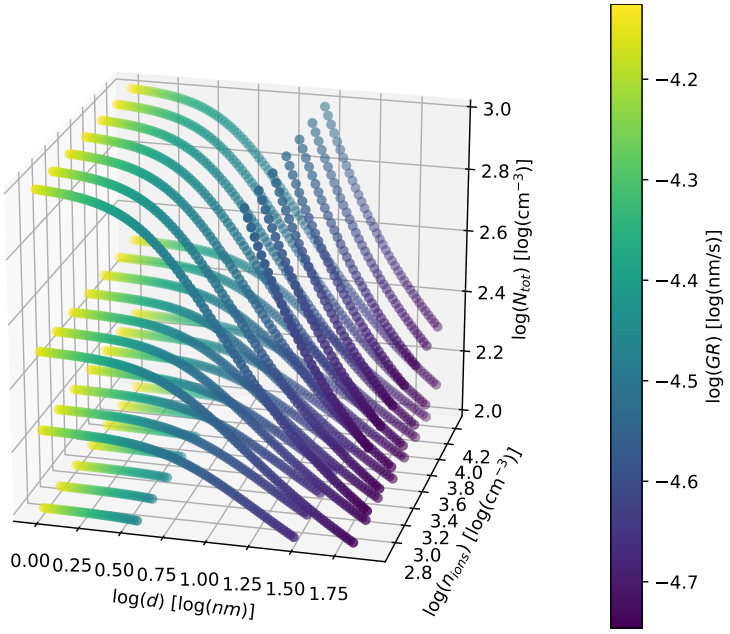

Figure 5.9: Subset of mean diameter growth rate enhancements in simulations at constant n^{ion}, including condensation and coagulation growth terms. As time evolves, N^T decreases and the mean diameter grows.

It should be noted that in general, ion mass, concentrations and interaction coefficients can be set and calculated individually, in the code, and need not to be restricted to the symmetric case tested here.

5.6 Discussion and Conclusion

In the present work a numeric model for simulating aerosol growth in the presence of charge has been developed and presented. The code consists of a 0-dimensional time integration model, where the interactions between ions and (charged) aerosols are taken into account. In particular ions are treated as massive condensing particles contributing to the growth rate in an implementation similar to condensation of neutral clusters here modeled as (H_2SO_4), while accounting for their inherent transfer of charge. The model is then used to investigate the newly demonstrated effect of ion-induced condensation from Svensmark et al. [2017] and a good agreement between model output and the theoretical and experimental SESS17 results is demonstrated employing condensation-only assumptions. Once coagulation is taken into account, we explore the conditions under which ion condensation is relevant, and show that while coagulation adds to the growth rate of aerosols when ions are present, it is not dependent on ion concentration, and in this sense the ion-condensation contribution to growth rate can be said to function independent of coagulation. Naturally in both experimental and real atmosphere scenarios there will be growth due to coagulation when the aerosol distribution is not well approximated by monodisperse conditions, there will be loss mechanisms and temporally varying concentrations of the ion-pairs and neutral clusters from which aerosols grow in size. Furthermore the positive and negative ions may in general be of different

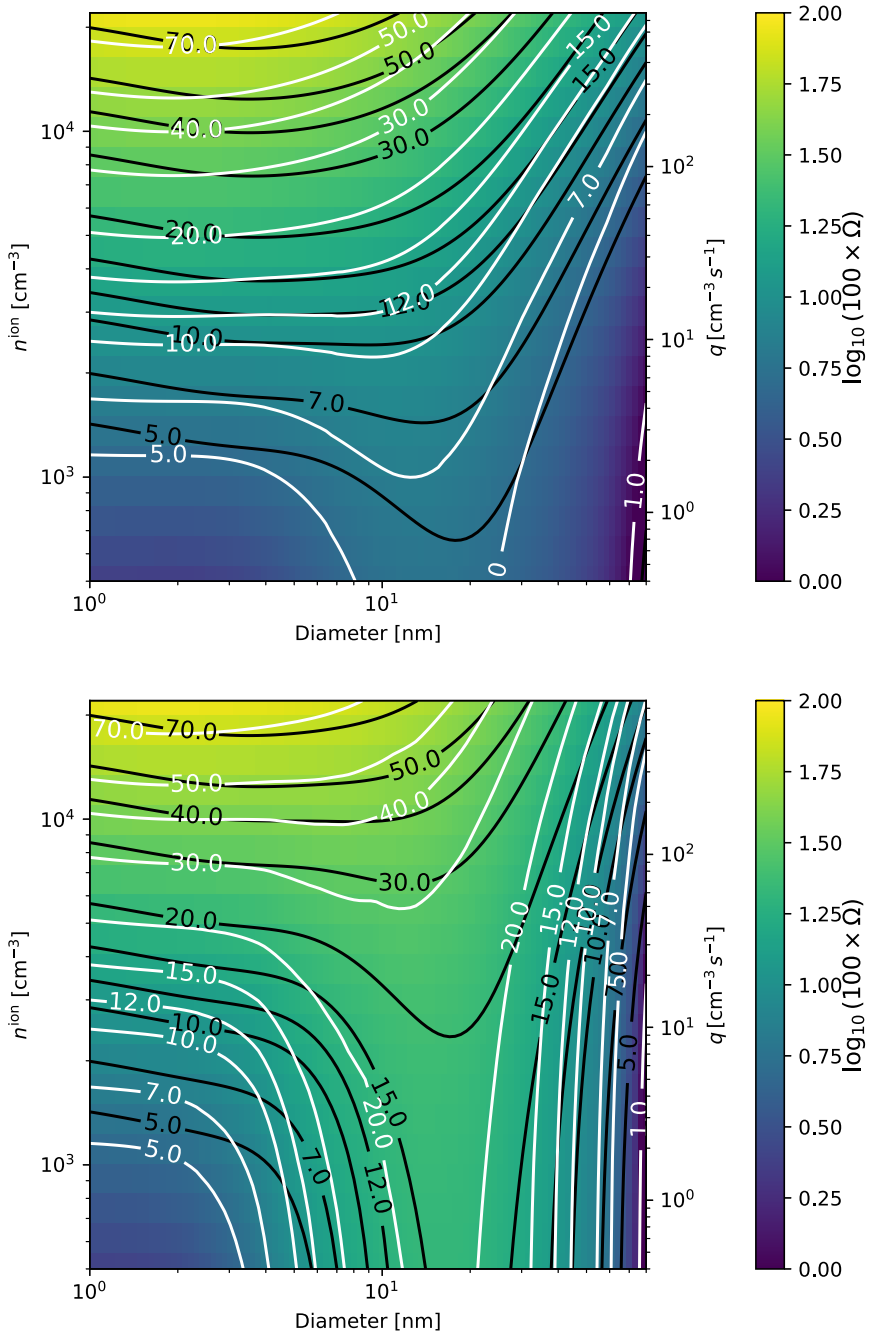

Figure 5.10: Charge enhancements of the growth rate Ω from condensation and coagulation. The black lines show the theoretical contours of equation 5.42, in percent. The white lines show contours of simulated Ω in percent. Both panels are calculated from a horizontal slice through the data of Figure 5.9. The y-axis on the left hand side of the panels shows the fixed ion-pair concentration, and the right hand side shows the equivalent ion-pair production rate as calculated by $q = 1.6 \times 10^{-6}(n^{\pm})^2$ *Top*: Total particle concentration $N^T = 100\,\mathrm{cm}^{-3}$. *Bottom*: $N^T = 500\,\mathrm{cm}^{-3}$

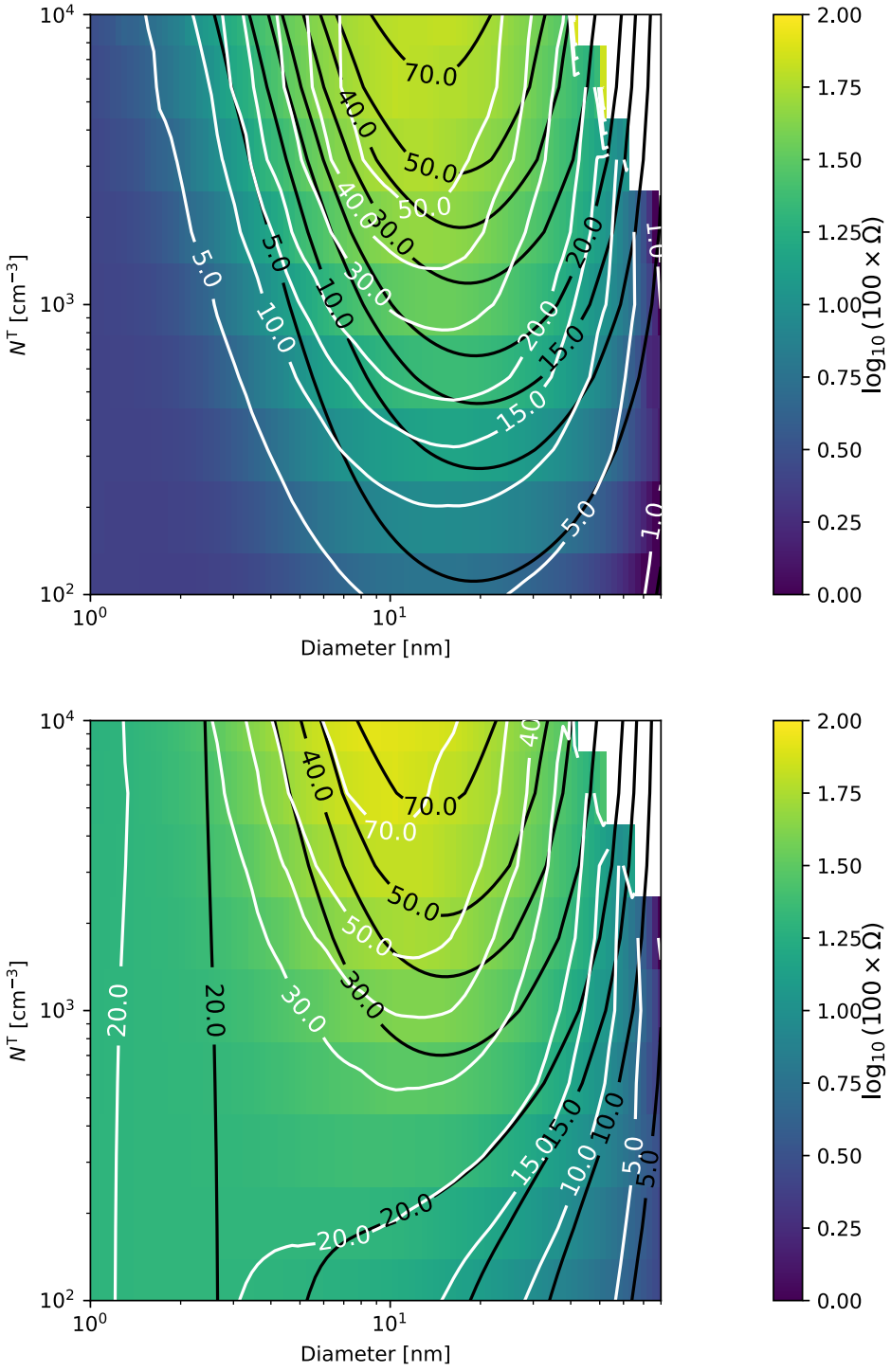

Figure 5.11: Charge enhancements of the growth rate Ω from condensation and coagulation, with a constant n^{ion}. The black lines show the theoretical contours of equation 5.42, in percent. The white lines show contours of simulated Ω in percent. Both panels are calculated from a vertical slice through the data of Figure 5.9. *Top*: Ion pair concentration $n^{\pm} = 500\,\mathrm{cm}^{-3}$. *Bottom*: $n^{\pm} = 5000\,\mathrm{cm}^{-3}$.

masses. These are parameters and dynamics which may be handled by the model in its current implementation.

The concept of ion-induced condensation is still new, and further investigation into its dynamics and implications are needed. The present model may prove a useful tool for describing the mechanism under a range on conditions and parameters relevant for the atmosphere, including some that would otherwise be unobtainable in the laboratory. While we have done a step towards describing it in the context of aerosol coagulation, more detailed work remains for future studies. Here, various scenarios could be considered such the effect on ion-induced condensation of introducing losses to experiment walls or large pre-existing aerosols. Simulations of realistic new particle formation events should be studied, to examine if the growth rate is enhanced under such scenarios. For atmospheric relevance it is necessary transform the effect of the ion condensation on the growth rate to a survival probability of the particles, i.e. to estimate the change in the number of CCN. This can be done either by numerical modeling or a simple theoretical estimate [Lehtinen et al., 2007, Kürten et al., 2015]. Also, the simulations depicted in Figure 5.8 could be repeated for upper tropospheric conditions with high ion pair production rates, low temperatures and low pressure. Furthermore an implementation of ion condensation into in higher dimensional models i.e. atmospheric circulation models would. Here, the current model would meet at challenge as numerical diffusion from the condensation term and computational weight of the coagulation term would need to be optimized.

The model could also be expanded to include more or different cluster-species. This could be relevant for investigating, for instance, how these species affect the growth of aerosols such as the role of organics in early aerosol growth [Tröestl et al., 2016]. Implementing evaporation of small clusters would allow for the model to be used in nucleation studies, as well for systems relevant to Earth [Zhang et al., 2004] or more exotic systems like TiO_2 relevant to brown dwarfs or exoplanets [Lee et al., 2015]. Further more, the model may provide insight into the fast dust grain growth observed in supernovae remnants [Gall et al., 2014, Bevan et al., 2017] and in high redshift galaxies [Watson et al., 2015, Michałowski, 2015].

5.7 Appendix

Here the parameters of the model are defined. We note that the calculated enhancement factors and potentials are system specific and that the calculations presented here should be considered as a first approximation.

5.7.1 Brownian coagulation kernel

The interaction coefficient between two aerosols in the Brownian regime is given by Jacobson and Seinfeld [2004] as

$$\beta^B{}_{i,j} = \frac{4\pi(a_i + a_j)(D_{m,i} + D_{m,j})}{\frac{a_i+a_j}{a_i+a_j+(\delta_{m,i}+\delta_{m,j})^{1/2}} + \frac{4(D_{m,i}+D_{m,j})}{\sqrt{\overline{v}_i^2+\overline{v}_j^2}(a_i+a_j)}} V_{i,j}, \tag{5.48}$$

where a_i and a_j are the radii of the two interacting particles. $\overline{v}_i = \sqrt{8k_BT/(\pi M_i)}$ is the average speed of the aerosol, with M_i being the mass of the aerosol. $D_{m,i}$ is the diffusion constant of particle of radius a_i

$$D_{m,i} = \frac{k_BT}{6\pi a_i \eta} \left[1 + \mathrm{Kn}_i \left(A_m + B_m \exp(-C_m/\mathrm{Kn}_i)\right)\right], \tag{5.49}$$

where the Knudsen number is given by $\mathrm{Kn}_i = \lambda/a_i$ and where λ is the mean free path of an air molecule. η is the dynamic viscosity of air, and

$$\delta_i = \frac{(2a_i + \lambda_i)^3 - (4a_i^2 + \lambda_i^2)^{3/2}}{6a_i\lambda_i} - 2a_i. \tag{5.50}$$

The three constants in the diffusion term are quoted by [Kasten, 1968] as

$$\begin{aligned} A_m &= 1.249, \\ B_m &= 0.42, \\ C_m &= 0.87. \end{aligned}$$

Finally the $V_{i,j}$ is an enhancement factor that can take interactions between the aerosols into account. This term will be defined in the next section.

5.7.2 Calculation of enhancement factors for coagulation of charged ions

In the case of charged aerosols, the Brownian coagulation coefficients should be corrected since their charge as well as their subsequent induction of additional charge results in a modified potential. For any potential, the correction factor for aerosols in the continuum regime ($Kn \to 0$) of radii a_i and a_j is [Jacobson and Seinfeld, 2004],

$$W^c_{i,j} = \frac{1}{(a_i + a_j)\int_{a_i+a_j}^{\infty} D_\infty/D_{i,j} \exp\left[\frac{E_{i,j}(r)}{k_BT}\right] r^{-2} dr}, \tag{5.51}$$

where $E_{i,j}(r)$ is the interaction potential between the two aerosols at separation r, k_B is the Boltzmann constant and T is the temperature. Viscous forces are taken into account by the following expression

$$D_\infty/D_{i,j} = 1 + \frac{2.6\ a_ia_j}{(a_i+a_j)^2}\sqrt{\frac{a_ia_j}{(a_i+a_j)(r-a_i-a_j)}} + \frac{a_ia_j}{(a_i+a_j)(r-a_i-a_j)}. \tag{5.52}$$

In the kinetic regime ($Kn \to \infty$) when the interaction between the two aerosols is attractive and has a singularity at contact, the enhancement factor is [Marlow, 1980]

$$W_{i,j}^{k} = \frac{-1}{2(a_i + a_j)^2 k_B T} \int_{a_i+a_j}^{\infty} \left(\frac{dE_{i,j}}{dr} + r \frac{d^2 E_{i,j}}{dr^2} \right) \exp\left[\frac{-1}{k_B T} \left(\frac{r}{2} \frac{dE_{i,j}}{dr} + E_{i,j} \right) \right] r^2 dr. \tag{5.53}$$

5.7.3 The potentials

In the present work the aerosols can be charged with a single charge, either positive or negative. Since the aerosols are made of dielectric medium the charge interaction will involve mirror charges, and the interaction potential will be slightly more involved. The potential representation used here is based on Bichoutskaia et al. [2010] for two spheres of radii a_i and a_j. For the two spheres with charge Q_i and Q_j, permittivity ϵ_i and ϵ_j and at a central distance r,

$$\begin{aligned} E_{EM,i,j}(r) \quad &= \quad K \frac{Q_i Q_j}{r} - Q_i \sum_{m=1}^{\infty} \sum_{l=0}^{\infty} \frac{(k_j - 1)m}{(k_j + 1)m + 1} \frac{(l+m)!}{l!m!} \\ &\times \quad \frac{a_j^{2m+1}}{r^{2m+l+2}} A_{1,l} - \frac{1}{K} \sum_{l=1}^{\infty} \frac{(k_i + 1)l + 1}{(k_i - 1)l} \frac{A_{1,l} A_{1,l}}{a_i^{2l+1}}, \end{aligned} \tag{5.54}$$

where $K = 1/4\pi\epsilon_0 \approx 9 \cdot 10^9$ Vm/C, $k_i = \epsilon_i/\epsilon_0$ and $k_j = \epsilon_j/\epsilon_0$ and $A_{1,l}$ are the coefficients found by solving the following implicit system of linear equations:

$$\begin{aligned} A_{1,l} \quad &= \quad a_i V_i \delta_{l,0} - \frac{(k_i - 1)l}{(k_i + 1)l + 1} \frac{a_i^{2l+1}}{r^{l+1}} a_j V_j + \frac{(k_i - 1)l}{(k_i + 1)l + 1} \\ &\times \quad \sum_{l_2=0}^{\infty} \sum_{l_3=0}^{\infty} \frac{(k_j - 1)l_2}{(k_j + 1)l_2 + 1} \frac{(l + l_2)!}{l! l_2!} \frac{(l_2 + l_3)!}{l_2! l_3!} \\ &\times \quad \frac{a_i^{2l+1} a_j^{2l_2+1}}{r^{l+2l_2+l_3+2}} A_{1,l_3}. \end{aligned} \tag{5.55}$$

Here $a_i V_i = K Q_i$, $a_j V_j = K Q_j$, and $\delta_{l,0}$ is the Kronecker delta function.

In addition to the electrostatic potential, it is assumed that there are short range Van der Waals forces present. This potential will ensure that there is a singular potential at contact and make the expression for the kinetic enhancement factor valid [Marlow, 1980]. The Van der Waals potential is given by

$$E_{\mathrm{vdW},i,j}(r) = -\frac{A}{6} \left[\frac{2a_i a_j}{r^2 - (a_i + a_j)^2} + \frac{2a_i a_j}{r^2 - (a_i - a_j)^2} + \log\left(\frac{r^2 - (a_i + a_j)^2}{r^2 - (a_i - a_j)^2} \right) \right]. \tag{5.56}$$

Here A is the Hamaker constant measured to be $A = (6.4 \pm 2.6)10^{-20}$ J for H2SO4-H2O aerosol interactions at 300 K [Chan and Mozurkewich, 2001].

5.7.4 Connecting the continuum regime with the kinetic regime

Calculation of $W^c_{i,j}$ and $W^k_{i,j}$ must be done numerically and it is therefore convenient to make the following variable transformation

$$x = \frac{a_i + a_j}{r}. \tag{5.57}$$

The interval of integration is changed from $[a_i + a_j; \infty[$ to $[0; 1]$, so that the enhancement factor in the continuum limit becomes

$$W^c_{i,j} = \left(\int_0^1 D_\infty / D_{i,j} \exp\left[\frac{E_{i,j}((a_i + a_j)/x)}{k_B T} \right] dx \right)^{-1}, \tag{5.58}$$

while the enhancement factor in the kinetic limit becomes

$$W^k_{i,j} = \frac{-1}{2k_B T} \int_0^1 \frac{1}{x^2} \left(x \frac{d^2 E_{i,j}}{dx^2} - \frac{dE_{i,j}}{dx} \right) \exp\left[\frac{-1}{k_B T} \left(E_{i,j} - \frac{x}{2} \frac{dE_{i,j}}{dx} \right) \right] dx. \tag{5.59}$$

The potential used here is

$$E_{i,j} = E_{EM,i,j} + E_{\mathrm{vdW},i,j}. \tag{5.60}$$

Finally the correction factor which interpolates between the continuum and kinetic regime is given by Alam [1987]

$$V_{i,j} = \frac{W^c_{i,j}[1 + 4(D_{m,i} + D_{m,j})/\sqrt{\overline{v_i}^2 + \overline{v_j}^2}(a_i + a_j)]}{1 + (W^c_{i,j}/W^k_{i,j})(4(D_{m,i} + D_{m,j})/\sqrt{\overline{v_i}^2 + \overline{v_j}^2}(a_i + a_j))}. \tag{5.61}$$

Figure 5.12 graphically displays the calculated enhancement factors. The above Brownian coagulation kernel can be used as a basis for including electrostatic and Van der Waals forces. Such effects are conveniently included by multiplying the Brownian coagulation kernel by a correction or enhancement factor. Such that

$$\begin{aligned} \kappa^{+0}_{i,j} &= {\beta^B}_{i,j} V^{+0}_{i,j}, \\ \kappa^{00}_{i,j} &= {\beta^B}_{i,j} V^{00}_{i,j}, \\ \kappa^{0-}_{i,j} &= {\beta^B}_{i,j} V^{0-}_{i,j}. \end{aligned}$$

The above calculations do not include three-body interactions such as discussed in López-Yglesias and Flagan [2013], where charged aerosols are slowed down by collisions with (but not attachments to) a third body, and subsequently attaches to another aerosol of a given charge. This will be important in the recombination between small ion-pairs, and that is the likely reason that the $V^{+-}_{i,j}$ coefficients for the smallest particles does not reach the

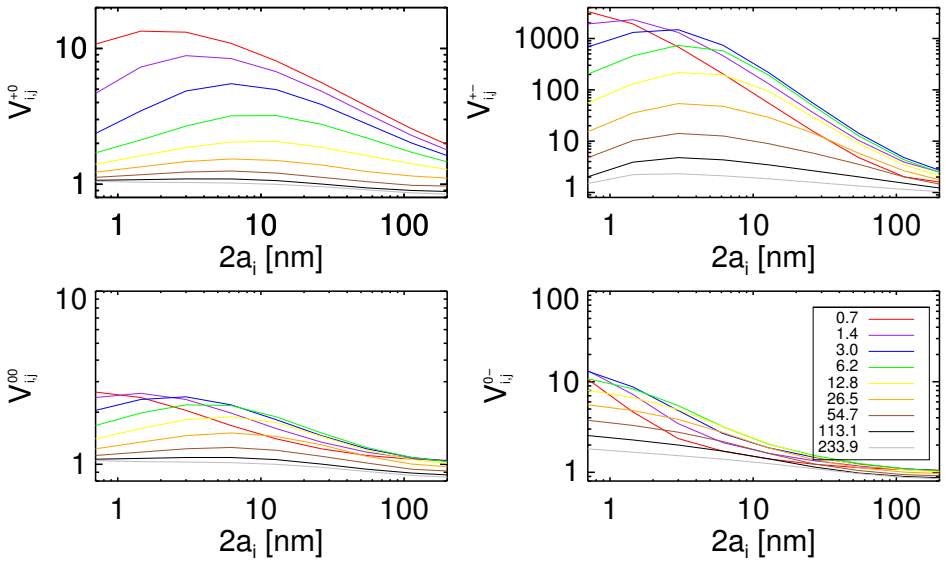

Figure 5.12: Enhancement factors between a particle of size a_i and a_j due to all effects mentioned in the Appendix and for $T = 300\,\mathrm{K}$, $\eta = 1.8362 \times 10^{-5}\,\mathrm{kg\,m^{-1}\,s^{-1}}$ and mean free path $\lambda = 65\,\mathrm{nm}$, for different charges on each of the coagulating spheres. Numbers in the legend are diameters are diameters in units of nm.

experimentally determined recombination coefficient $\alpha = 1.6 \cdot 10^{-6}$ cm^{3}s^{-1} but is a factor ≈ 5 too low. We correct this by simple adjustment, to obtain the final coagulation coefficients:

$$\kappa^{+-}_{i,j} = \frac{{\beta^B}_{i,j} V^{+-}_{i,j}}{1 + \left(\frac{{\beta^B}_{i,j} V^{+-}_{i,j}}{\alpha} - 1 \right) \exp\left(-\frac{\sqrt{d_i^2 + d_j^2}}{d_s} \right)}, \tag{5.62}$$

where $d_s = 100\,\mathrm{nm}$ is a characteristic scale length. The condensation coefficients used in the condensation equations are

$$\begin{aligned} \beta^{00}_k &= {\beta^B}_{0,k} V^{00}_{0,k}, \\ \beta^{0+}_k &= {\beta^B}_{0,k} V^{0+}_{0,k}, \\ \beta^{0-}_k &= {\beta^B}_{0,k} V^{0-}_{0,k}. \\ \beta^{+0}_k &= {\beta^B}_{+,k} V^{+0}_{+,k}. \\ \beta^{-0}_k &= {\beta^B}_{-,k} V^{-0}_{-,k}. \end{aligned} \tag{5.63}$$

Note that these β only have one index k for the radius of the aerosol a_k, as the radius of the condensing monomers (denoted with subscripts 0,$-$, and $+$) are fixed at radii a_0, a_-, and a_+. Again the recombination coefficient is used as a limit for the final two terms

$$\beta_k^{-+} = \frac{{\beta^B}_{-,k} V_{i,j}^{-+}}{1 + \left(\frac{{\beta^B}_{-,k} V_{-,k}^{-+}}{\alpha} - 1 \right) \exp\left(-\frac{a_j}{a_s} \right)}, \tag{5.64}$$

$$\beta_k^{+-} = \frac{{\beta^B}_{+,k} V_{i,j}^{+-}}{1 + \left(\frac{{\beta^B}_{+,k} V_{+,k}^{+-}}{\alpha} - 1 \right) \exp\left(-\frac{a_j}{a_s} \right)}, \tag{5.65}$$

where $\alpha = 1.6 \cdot 10^{-6}$ cm^{3}s^{-1}.

Bibliography

M. Khairul Alam. The effect of van der waals and viscous forces on aerosol coagulation. *Aerosol Science and Technology*, 6(1):41–52, 1987. doi: 10.1080/02786828708959118. URL https://doi.org/10.1080/02786828708959118.

A. Bevan, M. J. Barlow, and D. Milisavljevic. Dust masses for SN 1980K, SN1993J and Cassiopeia A from red-blue emission line asymmetries. *Monthly Notices of the RAS*, 465: 4044–4056, March 2017. doi: 10.1093/mnras/stw2985.

Elena Bichoutskaia, Adrian L. Boatwright, Armik Khachatourian, and Anthony J. Stace. Electrostatic analysis of the interactions between charged particles of dielectric materials. *The Journal of Chemical Physics*, 133(2):024105, 2010. doi: 10.1063/1.3457157. URL https://doi.org/10.1063/1.3457157.

Tak Wai Chan and Michael Mozurkewich. Measurement of the coagulation rate constant for sulfuric acid particles as a function of particle size using tandem differential mobility analysis. *Journal of Aerosol Science*, 32(3):321 – 339, 2001. ISSN 0021-8502. doi: https://doi.org/10.1016/S0021-8502(00)00081-1. URL http://www.sciencedirect.com/science/article/pii/S0021850200000811.

Eimear M. Dunne, Hamish Gordon, Andreas Kürten, João Almeida, Jonathan Duplissy, Christina Williamson, Ismael K. Ortega, Kirsty J. Pringle, Alexey Adamov, Urs Baltensperger, Peter Barmet, Francois Benduhn, Federico Bianchi, Martin Breitenlechner, Antony Clarke, Joachim Curtius, Josef Dommen, Neil M. Donahue, Sebastian Ehrhart, Richard C. Flagan, Alessandro Franchin, Roberto Guida, Jani Hakala, Armin Hansel, Martin Heinritzi, Tuija Jokinen, Juha Kangasluoma, Jasper Kirkby, Markku Kulmala, Agnieszka Kupc, Michael J. Lawler, Katrianne Lehtipalo, Vladimir Makhmutov, Graham Mann, Serge Mathot, Joonas Merikanto, Pasi Miettinen, Athanasios Nenes, Antti Onnela, Alexandru Rap, Carly L. S. Reddington, Francesco Riccobono, Nigel A. D. Richards, Matti P. Rissanen, Linda Rondo, Nina Sarnela, Siegfried Schobesberger, Kamalika Sengupta, Mario Simon, Mikko Sipilä, James N. Smith, Yuri Stozkhov, Antonio Tomé, Jasmin Tröstl, Paul E. Wagner, Daniela Wimmer, Paul M. Winkler, Douglas R. Worsnop, and Kenneth S. Carslaw. Global atmospheric particle formation from cern cloud measurements. *Science*, 354(6316):1119–1124, 2016. ISSN 0036-8075. doi: 10.1126/science.aaf2649. URL http://science.sciencemag.org/content/354/6316/1119.

Martin Bødker Enghoff and Jacob Svensmark. Measurement of the charging state of 4-70nm aerosols. *Journal of Aerosol Science*, 114(Supplement C):13 – 20, 2017. ISSN 0021-8502.

doi: https://doi.org/10.1016/j.jaerosci.2017.08.009. URL http://www.sciencedirect.com/science/article/pii/S0021850216303846.

Erwin Fehlberg. Low-order classical runge-kutta formulas with stepsize control and their application to some heat transfer problems. Technical Report NASA-TR-R-315, National Aeronautics and Space Administration, 1969.

C. Gall, J. Hjorth, D. Watson, E. Dwek, J. R. Maund, O. Fox, G. Leloudas, D. Malesani, and A. C. Day-Jones. Rapid formation of large dust grains in the luminous supernova 2010jl. *Nature*, 511:326–329, July 2014. doi: 10.1038/nature13558.

William A. Hoppel. Ion-aerosol attachment coefficients, ion depletion, and the charge distribution on aerosols. *Journal of Geophysical Research: Atmospheres*, 90(D4):5917–5923, 1985. doi: 10.1029/JD090iD04p05917. URL https://agupubs.onlinelibrary.wiley.com/doi/abs/10.1029/JD090iD04p05917.

William A. Hoppel and Glendon M. Frick. Ion-aerosol attachment coefficients and the steady-state charge distribution on aerosols in a bipolar ion environment. *Aerosol Science and Technology*, 5(1):1–21, 1986. doi: 10.1080/02786828608959073. URL https://doi.org/10.1080/02786828608959073.

M. Z. Jacobson and J. H. Seinfeld. Evolution of nanoparticle size and mixing state near the point of emission. *Atmospheric Environment*, 38:1839–1850, 2004. doi: 10.1016/j.atmosenv.2004.01.014.

M.Z. Jacobson. *Fundamentals of Atmospheric Modeling*. Cambridge University Press, 2005. ISBN 9780521548656. URL https://books.google.dk/books?id=96wWzoyKRMoC.

Fritz Kasten. Falling speed of aerosol particles. *Journal of Applied Meteorology*, 7(5):944–947, 1968. doi: 10.1175/1520-0450(1968)007<0944:FSOAP>2.0.CO;2. URL https://doi.org/10.1175/1520-0450(1968)007<0944:FSOAP>2.0.CO;2.

J. Kazil and E. R. Lovejoy. Tropospheric ionization and aerosol production: A model study. *Journal of Geophysical Research: Atmospheres*, 109(D19):n/a–n/a, 2004. ISSN 2156-2202. doi: 10.1029/2004JD004852. URL http://dx.doi.org/10.1029/2004JD004852. D19206.

A. Kürten, C. Williamson, J. Almeida, J. Kirkby, and J. Curtius. On the derivation of particle nucleation rates from experimental formation rates. *Atmospheric Chemistry and Physics*, 15(8):4063–4075, 2015. doi: 10.5194/acp-15-4063-2015. URL https://www.atmos-chem-phys.net/15/4063/2015/.

L. Laakso, J. M. Mäkelä, L. Pirjola, and M. Kulmala. Model studies on ion-induced nucleation in the atmosphere. *Journal of Geophysical Research (Atmospheres)*, 107(D20):4427–4445, 10 2002. doi: 10.1029/2002JD002140.

G. Lee, Ch. Helling, H. Giles, and S. T. Bromley. Dust in brown dwarfs and extra-solar planets iv. assessing tio2 and sio nucleation for cloud formation modelling. *ASTRONOMY & ASTROPHYSICS*, 575, 03 2015. ISSN 0004-6361. doi: 10.1051/0004-6361/201424621.

Kari E.J. Lehtinen, Miikka Dal Maso, Markku Kulmala, and Veli-Matti Kerminen. Estimating nucleation rates from apparent particle formation rates and vice versa: Revised formulation

of the kerminen-kulmala equation. *Journal of Aerosol Science*, 38(9):988 – 994, 2007. ISSN 0021-8502. doi: https://doi.org/10.1016/j.jaerosci.2007.06.009. URL http://www.sciencedirect.com/science/article/pii/S0021850207001024.

Johannes Leppä, Veli-Matti Kerminen, Lauri Laakso, Hannele Korhonen, Kari EJ Lehtinen, Stephanie Gagne, Hanna E Manninen, Tuomo Nieminen, and Markku Kulmala. Ion-uhma: a model for simulating the dynamics of neutral and charged aerosol particles. *Boreal Environ. Res*, 14:559–575, 2009.

Johannes Leppä, Topias Anttila, Veli-Matti Kerminen, M Kulmala, and K E. J. Lehtinen. Atmospheric new particle formation: real and apparent growth of neutral and charged particles. *Atmospheric Chemistry and Physics*, 11, 05 2011. doi: 10.5194/acp-11-4939-2011.

Xerxes López-Yglesias and Richard C. Flagan. Ion-aerosol flux coefficients and the steady-state charge distribution of aerosols in a bipolar ion environment. *Aerosol Science and Technology*, 47(6):688–704, 2013. doi: 10.1080/02786826.2013.783684. URL https://doi.org/10.1080/02786826.2013.783684.

Anni Määttänen, Joonas Merikanto, Henning Henschel, Jonathan Duplissy, Risto Makkonen, Ismael K. Ortega, and Hanna Vehkamäki. New parameterizations for neutral and ion-induced sulfuric acid-water particle formation in nucleation and kinetic regimes. *Journal of Geophysical Research: Atmospheres*, pages n/a–n/a. ISSN 2169-8996. doi: 10.1002/2017JD027429. URL http://dx.doi.org/10.1002/2017JD027429. 2017JD027429.

William H. Marlow. Derivation of aerosol collision rates for singular attractive contact potentials. *The Journal of Chemical Physics*, 73(12):6284–6287, 1980. doi: 10.1063/1.440126. URL https://doi.org/10.1063/1.440126.

M. J. McGrath, T. Olenius, I. K. Ortega, V. Loukonen, P. Paasonen, T. Kurtén, M. Kulmala, and H. Vehkamäki. Atmospheric cluster dynamics code: a flexible method for solution of the birth-death equations. *Atmospheric Chemistry and Physics*, 12(5):2345–2355, 2012. doi: 10.5194/acp-12-2345-2012. URL https://www.atmos-chem-phys.net/12/2345/2012/.

M. J. Michałowski. Dust production 680-850 million years after the Big Bang. *Astronomy and Astrophysics*, 577:A80, May 2015. doi: 10.1051/0004-6361/201525644.

J. R. Pierce and P. J. Adams. Can cosmic rays affect cloud condensation nuclei by altering new particle formation rates? *Geophysical Research Letters*, 36:L09820, May 2009. doi: 10.1029/2009GL037946.

A. Prakash, A. P. Bapat, and M. R. Zachariah. A simple numerical algorithm and software for solution of nucleation, surface growth, and coagulation problems. *Aerosol Science and Technology*, 37(11):892–898, 2003. doi: 10.1080/02786820300933. URL https://doi.org/10.1080/02786820300933.

Christian Seigneur, A. Belle Hudischewskyj, John H. Seinfeld, Kenneth T. Whitby, Evan R. Whitby, James R. Brock, and Harold M. Barnes. Simulation of aerosol dynamics: A comparative review of mathematical models. *Aerosol Science and Technology*, 5(2):205–222, 1986. doi: 10.1080/02786828608959088. URL https://doi.org/10.1080/02786828608959088.

J. H. Seinfeld and S. N. Pandis. *Atmospheric Chemistry and Physics: From Air Pollution to Climate Change*. John Wiley & Sons, Inc., 2nd edition, 2006. ISBN 0-471-72018-6.

L. F. Shampine, H. A. Watts, and S. M. Davenport. Solving nonstiff ordinary differential equations—the state of the art. *SIAM Review*, 18(3):376–411, 1976. doi: 10.1137/1018075. URL https://doi.org/10.1137/1018075.

H. Svensmark, M. B. Enghoff, N. J. Shaviv, and J. Svensmark. Increased ionization supports growth of aerosols into cloud condensation nuclei. *Nature Communications*, 8:2199, December 2017. doi: 10.1038/s41467-017-02082-2.

Henrik Svensmark, Martin B. Enghoff, and Jens Olaf Pepke Pedersen. Response of cloud condensation nuclei (>50 nm) to changes in ion-nucleation. *Physics Letters A*, 377(37):2343 – 2347, 2013. ISSN 0375-9601. doi: http://dx.doi.org/10.1016/j.physleta.2013.07.004. URL http://www.sciencedirect.com/science/article/pii/S0375960113006294.

Jasmin Tröestl, Wayne K. Chuang, Hamish Gordon, Martin Heinritzi, Chao Yan, Ugo Molteni, Lars Ahlm, Carla Frege, Federico Bianchi, Robert Wagner, Mario Simon, Katrianne Lehtipalo, Christina Williamson, Jill S. Craven, Jonathan Duplissy, Alexey Adamov, Joao Almeida, Anne-Kathrin Bernhammer, Martin Breitenlechner, Sophia Brilke, Antonio Dias, Sebastian Ehrhart, Richard C. Flagan, Alessandro Franchin, Claudia Fuchs, Roberto Guida, Martin Gysel, Armin Hansel, Christopher R. Hoyle, Tuija Jokinen, Heikki Junninen, Juha Kangasluoma, Helmi Keskinen, Jaeseok Kim, Manuel Krapf, Andreas Kuerten, Ari Laaksonen, Michael Lawler, Markus Leiminger, Serge Mathot, Ottmar Moehler, Tuomo Nieminen, Antti Onnela, Tuukka Petaejae, Felix M. Piel, Pasi Miettinen, Matti P. Rissanen, Linda Rondo, Nina Sarnela, Siegfried Schobesberger, Kamalika Sengupta, Mikko Sipila, James N. Smith, Gerhard Steiner, Antonio Tome, Annele Virtanen, Andrea C. Wagner, Ernest Weingartner, Daniela Wimmer, Paul M. Winkler, Penglin Ye, Kenneth S. Carslaw, Joachim Curtius, Josef Dommen, Jasper Kirkby, Markku Kulmala, Ilona Riipinen, Douglas R. Worsnop, Neil M. Donahue, and Urs Baltensperger. The role of low-volatility organic compounds in initial particle growth in the atmosphere. *NATURE*, 533(7604):527+, 05 2016. ISSN 0028-0836. doi: 10.1038/nature18271.

D. Watson, L. Christensen, K. K. Knudsen, J. Richard, A. Gallazzi, and M. J. Michałowski. A dusty, normal galaxy in the epoch of reionization. *Nature*, 519:327–330, March 2015. doi: 10.1038/nature14164.

A. Wiedensohler. An approximation of the bipolar charge distribution for particles in the submicron size range. *Journal of Aerosol Science*, 19(3):387–389, 1988. ISSN 0021-8502. doi: http://dx.doi.org/10.1016/0021-8502(88)90278-9.

Fangqun Yu. Ion-mediated nucleation in the atmosphere: Key controlling parameters, implications, and look-up table. *Journal of Geophysical Research: Atmospheres*, 115 (D3):n/a–n/a, 2010. ISSN 2156-2202. doi: 10.1029/2009JD012630. URL http://dx.doi.org/10.1029/2009JD012630. D03206.

Fangqun Yu and Richard P. Turco. From molecular clusters to nanoparticles: Role of ambient ionization in tropospheric aerosol formation. *Journal of Geophysical Research: Atmospheres*, 106(D5):4797–4814, 2001. ISSN 2156-2202. doi: 10.1029/2000JD900539. URL http://dx.doi.org/10.1029/2000JD900539.

RY Zhang, I Suh, J Zhao, D Zhang, EC Fortner, XX Tie, LT Molina, and MJ Molina. Atmospheric new particle formation enhanced by organic acids. *SCIENCE*, 304(5676):1487–1490, 06 2004. ISSN 0036-8075. doi: 10.1126/science.1095139.

Yang Zhang, Christian Seigneur, John H. Seinfeld, Mark Z. Jacobson, and Francis S. Binkowski. Simulation of aerosol dynamics: A comparative review of algorithms used in air quality models. *Aerosol Science and Technology*, 31(6):487–514, 1999. doi: 10.1080/027868299304039. URL `https://doi.org/10.1080/027868299304039`.